Structure dependence of molecular reactions on surfaces

Proefschrift

ter verkrijging van
de graad van Doctor aan de Universiteit Leiden,
op gezag van Rector Magnificus prof. mr. C. J. J. M. Stolker
volgens besluit van het College voor Promoties
te verdedigen op donderdag 11 oktober 2018
klokke 8.45 uur

door

Kun Cao
geboren te Henan, China, 1986

Promotiecomissie:

Promotors:
Prof. dr. M. T. M. Koper
Prof. dr. A. W. Kleyn

Co-promotor:
Dr. L. B. F. Juurlink

Overige leden:
Prof. dr. T. H. Oosterkamp
Prof. dr. G. J. Kroes
Prof. dr. H. S. Overkleeft
Prof. dr. M. A. Stöhr (University of Groningen, the Netherlands)
Dr. M. A. Gleeson (Dutch Institute for Fundamental Energy Research, the Netherlands)

The research reported in this thesis was financially supported by the China Scholarship Council (CSC).

C

Contents

C

Chapter 1

Introduction

1.1 Heterogeneous catalysis

The phrase catalysis was coined by Jöns Jakob Berzelius who in 1836 was the first to describe reactions that are accelerated by substances that remain unchanged after the reaction[1]. Catalysis plays an important role in biology and chemistry. It modifies the kinetics for the reaction, modifies the pathway of the reaction and steers a reaction toward a specific product.

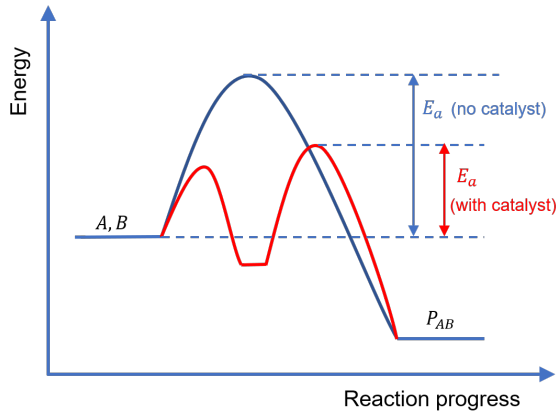

Figure 1.1: Generic potential energy diagram showing the effect of a catalyst in a hypothetical exoergic chemical reaction $A + B \rightarrow P_{AB}$. The presence of the catalyst opens a different reaction pathway with a lower activation energy.

There are three types of catalysis. Biocatalysis, where the catalyst is an enzyme. Homogeneous catalysis, where the catalyst is in the

same phase as the reactant and product. Heterogeneous catalysis, where the catalyst is in a separate phase. The obvious advantage of heterogeneous catalysis is the easy separation of product and catalyst. Heterogeneous catalysis is widely used in industrial catalytic processes like the Sabatier reaction for synthesizing methane from CO_2, the car exhaust gas system[2] and fuel cells[3]. This thesis describes studies into elementary steps in heterogeneous catalysis.

In a heterogeneously catalyzed reaction, the following steps occur: diffusion of reactant to the catalyst, adsorption and diffusion of reactant on the surface of the catalyst, reactions on the catalyst surface, desorption of product from the catalyst surface and diffusion of product away from the catalyst. The understanding of the mechanism of reactions, notably the adsorption step on the catalyst surface, is the goal of research. Here, we investigate how elementary steps depend on the structure of the surface.

For a real catalyst, the structure and surface is not homogeneous. The reactions are not taking place at the entire surface but have favorite active sites. The fundamental understanding of the active sites and the reaction mechanism can help us improve the design and synthesis of new catalysts. But it is difficult to carry out such research for a real catalyst, working under industrial conditions.

To simplify the question, working under vacuum, using well characterized single crystalline surfaces and simple reactions has proven to be a good approach.

1.2 Ultra-high vacuum

Vacuum is a space devoid of matter. A perfect vacuum is ideal and not achievable in reality. An approximate of a perfect vacuum is a region that the residual gas pressure is so low that it takes on the order of an hour to cover a surface with one monolayer of residual gas molecules.

Ultrahigh vacuum (UHV) always refer to a pressure less than 1×10^{-9} mbar. The UHV condition can be obtained by using specially designed vacuun pumps, such as a series of a rotary pump, turbo pump and/or an ion pump. UHV conditions are an integral ingredient for science research. Surface science experiments always need a chemically clean surface without any unwanted adsorbates, which under UHV remains clean for a longer time, say, 10 minutes. Most surface analysis

techniques, such as low energy electron diffraction (LEED), require at least high vacuum conditions for the transmission of an electron beam.

In a properly designed UHV system, several surface science experiments can be carried out. By using an Ar sputter gun the surface can be cleaned. Many surface analysis tools can be used to study the surface, like a scanning tunneling microscope (STM), low energy electron diffraction (LEED) and Auger electron spectroscopy (AES). The reactant, always in the gas phase, is introduced into the UHV chamber by using a leak valve or by using a molecular beam. The reaction conditions, such as temperature and pressure, can be controlled. The product can be detected in the gas phase by using a quadrupole mass spectrometer (QMS).

1.3 Simple surface

The surface of a real catalyst is very complex. It may contain steps, kinks and facets etc. It is difficult to identify the active sites. By using a well-defined single crystal surface, we have control over which types of sites are provided. We can study the effect of various types of sites using different single crystal surfaces.

The use of the single crystal surface also has disadvantages. To fully understand the reaction mechanism of reactions on real complex catalyst surfaces, several single crystals with different crystal faces are needed. This is expensive and repeating experiments on various crystal surfaces takes a lot of work and time. If we can introduce different structures onto one single crystal in some order and measure the reactivity locally, then we can study the catalytic reactivity simpler and faster. Chapters 5 and 6 in this thesis show the use of a curved Pt(111) surface to study the step density dependence of HD formation and O_2 sticking on Pt surface.

1.4 Simple reaction

We always use small molecules in this thesis, such as H_2, D_2 and O_2 etc. The dissociative adsorption of a diatomic molecule on a surface follows a series of steps, the first of which on the surface is:

$$A_2(g) \rightleftharpoons 2A(ads) \tag{1.1}$$

which is the simplest initial step for heterogeneous catalysis. The reverse reaction is the recombination and desorption of a diatomic molecule from surface.

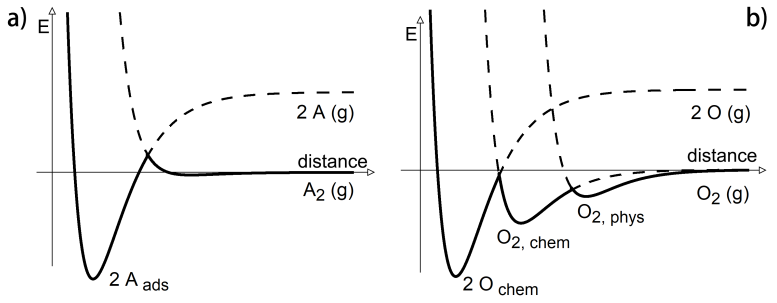

Figure 1.2: a) shows the energy diagram for dissociative adsorption of diatomic molecule, as equation (1.1) describes. b) illustrates hypothetical one dimension potential energy surface for equation (1.2).

For complex reactions containing intermediate states, like O_2 on Pt surface:

$$\begin{aligned} O_2(g) &\rightleftharpoons O_{2,phys} \\ O_{2,phys} &\rightleftharpoons O^{n-}_{2,chem} \\ O^{n-}_{2,chem} &\rightleftharpoons 2O_{chem} \end{aligned} \tag{1.2}$$

the dissociative adsorption may occur via physisorption and chemisorption states. Figure 1.2 illustrates the one-dimensional potential energy surfaces of equation (1.1) and (1.2).

One advantage of using small molecules is that these are relatively easy to model by theory. Then the experimental and theoretical results can be combined to obtain a deeper understanding of the mechanism. Calculations are usually separated into two parts. The Born-Oppenheimer approximation is used assuming that the energy of the electronic system of the reactants and the surface can be calculated for fixed positions of the nuclei. This gives a potential energy surface (PES) for the interacting particles. The dimensions of the potential energy surface for a small molecule with a surface are not too large to calculate using Density Functional Theory (DFT). The PES allows to calculate the molecular and surface motion using classical mechanics or quantum mechanics. Figure 1.3 shows a coordinate system of a diatomic molecule with a fcc (111) surface. The motion of the molecular center of mass is represented by the set of coordinates (X, Y, Z), the orientation of the molecular axis is represented by the angles (θ and

ϕ), the stretching of the molecule is represented by coordinate r. The surface atom motion, which also could take into account, is not shown in this figure. The figure also shows some low coordinate sites such as steps, kinks, corners etc.

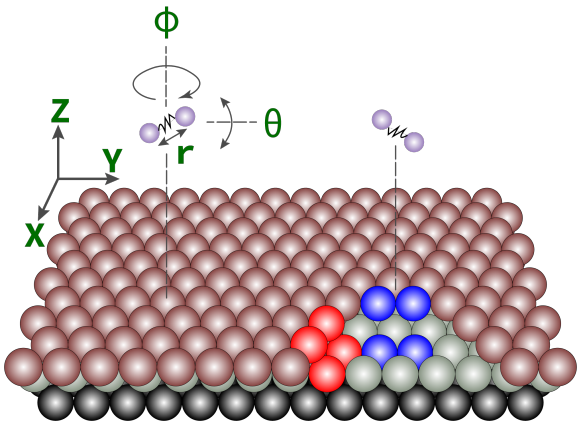

Figure 1.3: Coordinate system of diatomic molecule with a fcc-(111) surface. The surface also contains defects. The red and blue atoms indicate the (100) (also called A-type) and (110) (B-type) step, respectively.

1.5 Reactions on surfaces

For the simplest reaction on surface in which a bond is broken, i.e. dissociative adsorption of a diatomic molecule, there are two mechanisms. First is the direct mechanism. In this case, a molecule incident from the gas phase directly dissociates upon the collision with surface. This process may be activated depending on the type of molecule and surface. The other mechanism is the trapping-mediated mechanism. The molecule is trapped on the surface in a weak physisorption or chemisorption state. It diffuses on the surface until it finds an active site where it can dissociate. As the interaction between the molecule and the surface is weak, the molecule has a finite residence time on the surface. Subsequently it may desorb or dissociation.

Reactions on surfaces can take place through several mechanisms. The most common is the Langmuir-Hinshelwood (LH) mechanism[4, 5]. In this mechanism, the reactants are trapped or dissociated on the surface. Two or more adsorbed species meet through thermal diffusion and react on the surface. Then the product desorbs from the surface.

Another mechanism is the Eley-Rideal (ER) mechanism[6, 7]. In this mechanism, one reactant is on the surface, the other collides with it directly from the gas phase without equilibration or diffusion. The the reaction takes place upon the collision, followed by a desorption of product. An intermediate mechanism is the hot-atom (HA) or Harris-Kasemo mechanism[8]. It is in between the LH and ER mechanism. In this mechanism, one reactant coming from the gas phase, bounces around on the surface for a short period of time, and then reacts with another reactant adsorbed on the surface without having thermalized. Another mechanism, that is introduced by Mars and van Krevelen[9] is not relevant to this thesis.

1.6 Scope of this thesis

The research presented in this thesis makes use of small molecules (as H_2, D_2 and O_2) on well-defined single crystal surfaces (flat Pt(111), flat Cu(211) and curved Pt(111)) to elucidate the role of surface structure and degrees of freedom in the reactant in specific surface reactions.

In chapter 2, we briefly describe the experimental apparatus and the general experimental techniques used in this thesis.

In chapter 3, we investigate geometric corrugation for D_2 dissociation on Pt(111) by mapping the dependence of the initial reaction probability on incident kinetic energy and polar angle for two different azimuths. In accordance with predictions from dynamical calculations of dissociation on an SRP-based potential energy surface, we find at most a very weak signature of geometric corrugation at large polar angles.

In chapter 4, we present a combined experimental-theoretical study on structural and coverages dependences of the adsorption and desorption of molecular hydrogen on atomically flat Cu(111) and highly stepped Cu(211) surfaces. For molecules with identical incident energy from supersonic molecular beams, we find a reduced dissociative sticking probability for the stepped surface compared to Cu(111). DFT calculations of activation barriers to dissociation for the clean and partially precovered surfaces, as well as quantitative analysis of TPD spectra support that the A-type step of the (211) surface causes an upward shift in activation barriers to dissociation and a lowering of the desorption barrier. The new data allow us to determine low stick-

ing probabilities at conditions where King and Wells measurements fail to determine the reactivity. They are also fully consistent with the unexpected observation that monoatomic steps on a surface lower the reactivity toward the dissociation of a diatomic molecule.

In chapter 5, we introduce (100) and (110) steps at varying step density onto a surface consisting otherwise of (111) planes by using a curved Pt(111) single crystal. As HD formation from H_2 and D_2 incident onto Pt at low incident energy is very sensitive to the step density, we use an anti-seeded supersonic molecular beam to probe surface structure variation along on the curved surface. HD formation increases linearly from the (111) apex of the crystal to the edges when the curved crystal is cleaned and annealed at 850 K. It reflects the dominance of the indirect dissociation mechanism of molecular hydrogen occurring at step sites and the linear step density variation with position on the crystal. A LEED study confirms the structural variation through a spot-splitting analysis. When the curved crystal is cleaned using the same procedure but annealing occurs at 1200 K, HD formation is non-linear. Reactivity is strongly reduced over the entire A-type step side of the crystal. Here, the surface seems to restructure by formation of large (100) facets. For the B-type step side, steps remain monoatomic except near the (443) plane. It shows that, in contrary to common belief, it is the 7-atom wide (111) terrace with B-type steps that is unstable and not the 8-atom wide (997) surface. Although changes are observable in LEED patterns, our study shows that H-D exchange as a chemical probe is much more sensitive to surface structure changes caused by higher annealing temperature.

In chapter 6, we present the first study combining curved single crystals and stereodynamical control of impinging O_2 to unravel how monoatomic steps improve oxidation kinetics. Based on general principles, defect sites on Pt catalyst particles may be expected to enhance reactivity, but the reaction dynamics underlying such improved kinetics remain largely unexplored. Our results show that at low incident energy, steps dominate reactivity by providing means for an indirect dynamical trapping mechanism with no orientational dependence to the incident O_2 molecule. At higher impact energy, a direct chemisorption mechanism dominates. For the step facet, we show that it favors molecules impacting with their internuclear axis parallel to its surface. Combined with the contribution of atomically flat terraces, stereodynamical filtering controls reactivity at high temperature conditions.

1

Chapter 2

Experimental apparatus and techniques

2.1 Ultra-high vacuum apparatus

2.1.1 Potvis

Potvis is a home-built UHV system with a base pressure below 8×10^{-11} mbar. This system contains a double differential-pumping supersonic molecular beam chamber, a quadrupole mass spectrometer (QMS, Pfeiffer QMA 200), a quadrupole mass spectrometer (QMS, Pfeiffer QMA 400) which can move along themolecular beam axis, and a LEED/AES (OCI BDL800IR-MCP) system.

The main UHV chamber is connected to a series of 3 vacuum chambers used to generate a well-defined molecular beam through supersonic expansion of gases. The molecular beam is generated by expansion of a gas (or a gas mixture) at a total pressure of $1.0 \sim 5.0$ bar through a tungsten nozzle with a 25 μm diameter orifice. The nozzle's 25 μm diameter orifice is accurately positioned at variable distance (between approx. 1 and 15 mm) from the first of this series of skimmers (Model 1, 0.25 mm, Beam Dynamics). To increase the kinetic energy of molecules in the expansion, the tungsten tip of the nozzle is heated radiatively by a second short tungsten tube that surrounds the tungsten tip. This second tube is heated by electron bombardment using two oppositely positioned filaments. A C-type thermocouple is spot-welded to the Ta part of the expansion tube, approx. 10-20 mm from the 25 μm diameter orifice.

We skim the gas expansion in the source chamber to create a beam which passes through two stages of differential-pumping prior to entering the UHV chamber, which houses a temperature-controlled single crystal on an *x, y, z, θ* manipulator. A valve separates the two differential pumping stages. Two additional flags in the beam line can be opened and closed. They are used to determine the absolute dissociation probabilities by the King and Wells (KW) technique[10]. The first flag is located in the first differential pumping stage. The second flag is located inside the main UHV chamber. The opening and closing of both flags is computer-controlled to ensure an accurate timing. For KW measurements, we use a Baltzers quadrupole mass analyzer (QMA 200), positioned such that it samples the pressure rise from the SMB after equilibration inside the chamber. When retracting the sample, the beam enters the differentially-pumped housing of a Baltzer's 400 quadrupole mass analyzer (QMA 400) of a special linear design with a cross-beam ionizer and two consecutive quadrupole mass filters. It is used to determine the kinetic energy of molecules in the beam through time-of-flight (TOF) analysis and for temperature programmed desorption (TPD). The differentially-pumped QMA is retractable over 200 mm along the beam axis, allowing TOF measurements for varying neutral flight path lengths. More details of our entire UHV-SMB system were previously described in Ref.[11].

2.1.2 Lionfish

Lionfish is another home-build ultra high vacuum (UHV) apparatus (base pressure is below 1×10^{-10} mbar). This system contains a double differential-pumping super sonic molecular beam chamber, a quadrupole mass spectrometer (QMS, Pfeiffer QMA 200), a quadrupole mass spectrometer (UTI, 100C) which can move along the molecular beam axis, and a LEED/AES (OCI BDL800IR-MCP) apparatus.

The crystal is mounted on an x, y, z, θ manipulator. The surface temperature can be controlled between 89 and 1300 K with the use of liquid nitrogen cooling and radiative heating combined with electron bombardment for heating.

The molecular beam is generated by expansion of a gas (or a gas mixture) at a total pressure of $1.0 \sim 4.0$ bar through a tungsten nozzle with a 28 μm diameter orifice. The beam is shaped by two skimmers (subsequent diameters from the expansion nozzle are 0.45 mm and 2.5

mm). Two flags, one positioned in the second differential pumping chamber and one in the UHV chamber, and a chopper wheel located in the first differential chamber, modulate the beam. The two flags are used to determine the absolute dissociation probability using the King and Wells (KW) technique[10]. The chopper wheel is a fast rotating disk (∼250 Hz) with two broad (17 mm) and two narrow (0.85 mm) slits. It is used to determine the kinetic energy and the energy distribution using time-of-flight (TOF) techniques.

A home-made gate valve separates the second differential pumping chamber and the UHV chamber. It consists of a rectangular plate with four orifices. It slides through a groove cut into a solid flange with knife edges on both sides. A linear feedthrough accurately positions the sliding plate within the groove. The sliding plate contains, besides an O-ring to seal the UHV chamber, one larger hole with a diameter of 6.2 mm, one medium-sized hole with diameter of 3.2 mm, one small hole with diameter of 1.6 mm, and a rectangular slit of 3.2 mm in horizontal direction and 0.065 mm in vertical direction. By choosing different orifices on the plate, we can change the molecular beam's size and shape at the crystal position inside the UHV chamber.

2.2 Experimental techniques

2.2.1 Low energy electron diffraction

Low energy electron diffraction (LEED) is a technique to study surface structures. The rather simple and well known example for diffraction is Bragg diffraction:

$$2dsin\theta = n\lambda \tag{2.1}$$

where d is the interplanar distance, θ is the scattering angle, n is a positive integer and λ is the wavelength, in the present case of the electron beam. Scattering the electron beam from the surface will yield a pattern with spots, showing the crystal in reciprocal space.

For a surface containing steps, the following expression for the scattered intensity I at an angle φ is derived[12]:

$$I(\varphi) = const. \frac{sin^2[\frac{1}{2}ka(N+1)sin\varphi]}{sin^2[\frac{1}{2}kasin\varphi]} \times \sum_{i=-\infty}^{+\infty} \delta[\frac{1}{2}k(N \times a + g)sin\varphi + \frac{1}{2}kd(1+cos\varphi) - i\pi] \tag{2.2}$$

where I is the intensity of electron beam in direction φ, $k = 2\pi/\lambda$, λ is the wavelength of the electron beam, $N+1$ is the number of atom rows on one terrace and a is the separation of atom rows, d is the step height and g is the horizontal shift of the top layer compared with the adjacent step, i is an integer.

The first term of equation 2.2 is due to the finite number of atoms on a single terrace and equals the expression for the intensity distribution for a grating with $N+1$ slits. The second term of equation 2.2 is a sum of δ-functions in the limit of an infinite number of steps. The figure 2.1 shows simulations of LEED for $Pt[N(111) \times (100)]$ surfaces at two different beam energies. The (0,0) spot is a single spot at beam energy equals 65.7 eV and becomes doublet at 89.5 eV. As the right panel shows, the spot splitting decreases with increasing the terrace length N.

For $(0,0)$ spot, $\varphi = 0$, the second term of equation 2.2 can be rewritten as the following equation by using $\lambda \sim \sqrt{150/V}$, where V is the acceleration voltage of the electron beam:

$$V_{00} = \frac{150i^2}{4d^2} \tag{2.3}$$

where V_{00} is the voltage in volts for observation of a single $(0,0)$ spot, d is the step height in Å. For a integral i the $(0,0)$ spot is a single spot. The value $E = 65.7eV$ in the left panel of figure 2.1 corresponds to $i = 3$. To get a doublet with equal intensity in each spot, two delta functions that lie symmetrical on both sides near $(0,0)$ are required. This responds to the half-integer value of i. The energy 89.5 eV in the right panel of figure 2.1 corresponds to $i = 3.5$. By measuring the voltages corresponding to single or doublet spots of $(0,0)$ and combining with equation 2.3, the step height can be obtained.

The LEED patterns in this thesis are obtained using a microchannel plate (MCP) LEED/AES optics (OCI BDL800IR-MCP). Because of the design of this LEED system, the patterns are distorted. The details

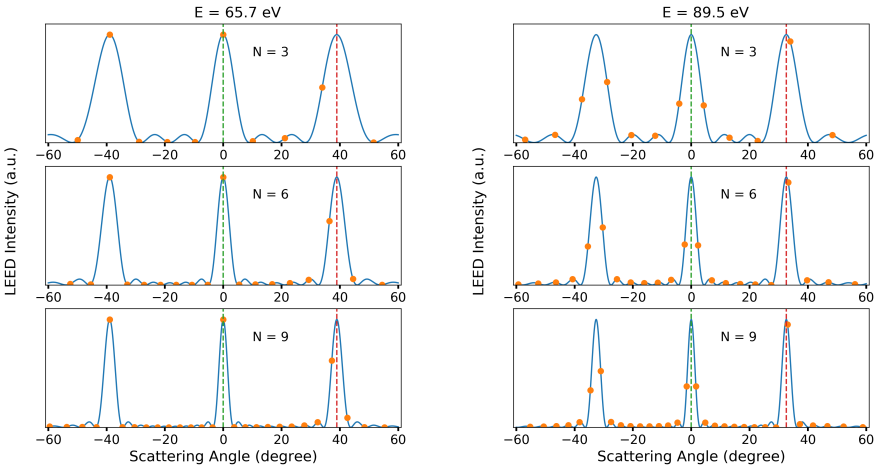

Figure 2.1: The simulation of LEED by using equation 2.2. The parameters used are from a series of $Pt[N(111) \times (100)]$ surfaces, where a is 2.40 Å, d is 2.27 Å and g is 1.60 Å. The beam energies are 65.7 eV and 89.5 eV for left and right figures, respectively. The solid curves are from the first term of equation 2.2. The circles are from the second term of equation 2.2.

of the origin of distortions and the correction procedures are described in Ref. [13].

2.2.2 King and Wells technique

The sticking probability of a molecule on a single crystal surface is measured directly by the King and Wells (KW) technique[10]. It requires two flags on the beam axis. One is positioned in the beam line prior to it entering the UHV chamber. The second flag is inside the UHV chamber and can block the beam from impinging onto the crystal. The measurement consists of the follow steps:

- At the beginning, both of the flags are closed. The beam is blocked from entering the UHV chamber. The QMS measures the effusive load of the beam.

- First, the first flag in the beam line is opened. The beam enters into the UHV chamber but does not collides with the surface, because the second flag is closed. This will cause a rise of the QMS intensity, labeled as L_1.

- Second, the second flag is opened. The beam collides with the surface and partially sticks on the surface. A drop of QMS intensity occurs, labeled as L_2.

- The sticking probability can be calculated by:

$$S = \frac{L_2}{L_1} \tag{2.4}$$

Fig. 2.2a) shows an example of KW measurements on Potvis. It shows a slowly increasing background, which we account for by fitting and extrapolating the data prior to opening the second flag and by comparison to results when the second flag was not opened at all during experiment. Note that accounting for this modest change in background for the duration of the experiment (on the order of a couple of percent only) is relevant to accurate determination of the time-dependence of sticking. The slow increase in background likely results from variations of the pumping speed of the UHV system and/or a change in the sensitivity of the QMS by exposure to reducing and oxidizing gases, e.g. H_2 and O_2 [14]. Fig. 2.2b) illustrates how we extract an accurate initial sticking coefficient, S_0, from the data in a). We fit the time-dependent sticking obtained through normalizing and inverting the KW trace by a linear functional form through the first couple of seconds and a double exponential functional form when reliable data is available for longer exposures, and extrapolating to the exact time of opening the second flag. This removes the convolution of the QMS partial pressure measurement at 4-5 Hz with the time constant from opening the second flag.

The KW technique used with a single measurement can be applied when the sticking probability, S, is larger than $\sim$0.01-0.03 as the dip in the partial pressure trace that appears when opening the second flag needs to be discernable within the noise-level. To improve our detection limit, the opening and closing of the two flags is computer-controlled with accurate, but variable time intervals for both flags. The sticking probability is measured repeatedly under identical conditions and we average the resulting KW-traces. Hence, we improve our detection limit by (approximately) the square root of the number of repetitions of the measurement. An example of this trick is shown in chapter 4, figure 4.2.

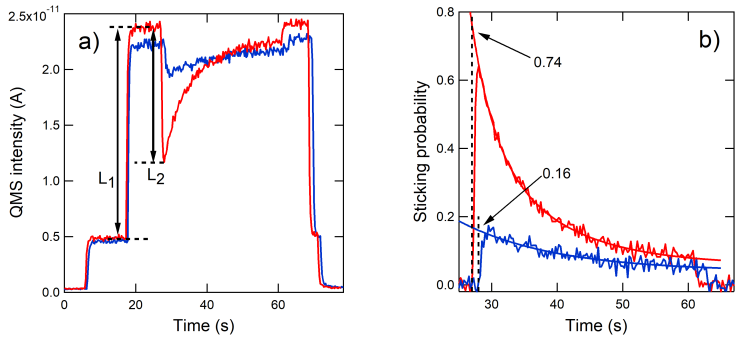

Figure 2.2: a) An example of KW measurements of D_2 on Pt(111) on Potvis. The kinetic energy of D_2 is 0.46 eV. The polar angles between the beam axis and the surface normal are 0° and 50° for the red and blue curves, respectively. The first plateau is cause by the opening of the valve between the two differential pumping stages. b) Examples of the time-dependent sticking and double-exponential fits obtained from normalizing and inverting the KW traces as shown in a).

2.2.3 Time of flight technique

The velocity distribution of the beam can be described by a shifted Maxwell-Boltzmann distribution [15]:

$$P_{vel}(v;T_n) = Av^3\exp(-(v-v_0)^2/\alpha^2) \tag{2.5}$$

where v_0 is the flow velocity, α a measure for the velocity spread, and A a normalization factor. We use time-of-flight (TOF) methods to measure the molecular beam's velocity distribution. The continuous molecular beam is chopped into short pulses by a chopper wheel with a duty cycle of 0.5%. The chopper wheel is spun at a high frequency, resulting in convolution of the TOF distribution with a gating function.

The total measured flight time, t_{total}, is composed of the following contributions:

$$t_{total} = t_{TOF} + \Delta t_{trig} + \Delta t_{elec} + \Delta t_{QMS} \tag{2.6}$$

where t_{TOF} is the flight time of the neutral species from chopper wheel to the QMS ionizer over a distance L. Δt_{trig} captures the offset between the signal of the optical sensor triggering our multi-channel scalar (MCS) card and the center time of release of the gas pulse. Δt_{QMS} captures the flight time of the ionized species from ionizer to the QMS channeltron. Δt_{elec} captures the electronic delay difference for the optical pulse and channeltron pulse to arrive at the MCS card.

Our QMS, with its cross-beam ionizer, is mounted inside a differentially pumped stage, which can be moved by an x, y, z manipulator along the beam axis over a distance, d, of 200 mm on Potvis and 50 mm on Lionfish. By doing so, we vary only L, *i.e.* the flight length of the neutral, hence t_{TOF}. As figure 2.3 shows, through linear extrapolation of t_{total} to L=0 mm, we derive the sum of all other time delays, i.e. $\Delta t_{trig} + \Delta t_{elec} + \Delta t_{QMS}$. These offsetting values are required for fitting procedures in the time-domain, as described below. Simultaneously, the slope in a graph plotting the most probable arrival time for different values of d yields the most probable velocity. This is not identical to v_0, though.

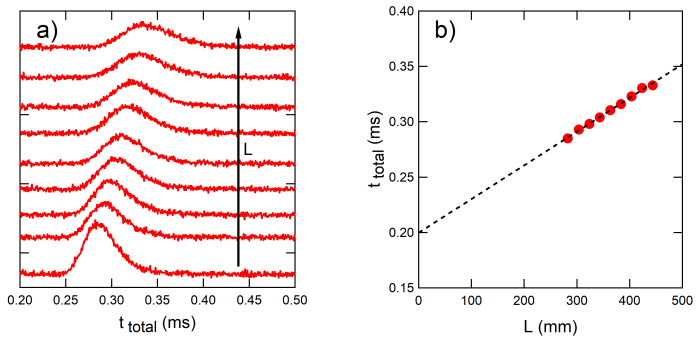

Figure 2.3: a) The TOF spectrum at different L positions. A clear shift of total flight time with increasing flight length, L, is observed b) shows the TOF peak's total flight time versus the flight length L. The intercept with y-axis yields the sum of all other time delays, $\Delta t_{trig} + \Delta t_{elec} + \Delta t_{QMS}$.

To obtain the beam's velocity distribution, we convert equation (2.5) to the time-domain [15]

$$\int P_{vel}(v; T_n) dv = \int g(t; T_n) dt \tag{2.7}$$

Using $v = L/t$ and $dv \sim t^{-2}$ the function can be rewritten as:

$$g(t; T_n) \sim \left(\frac{L}{t}\right)^5 \cdot \exp\left(-\left(\frac{\frac{L}{t} - \frac{L}{t_0}}{\alpha}\right)^2\right) \tag{2.8}$$

The time t in this equation corresponds to the time-of-flight for the neutral species, t_{TOF}. Prior to fitting in the time domain, we correct the measured time, t_{total}, for all delays and off sets as determined by

the procedure described above. Then we fit each TOF spectrum for its specific neutral flight path length, L, taking into account that our density sensitive detector modulates the signal by a factor of $1/v$, hence fitting $g_{dens}(t)$ with a pre-exponential factor proportional to $(L/t)^4$. We also include a gating function by adding nine of the $g_{dens}(t)$ functions, each separated by 3 μs and scaled with the appropriate amplitude. We verify that the flow velocity, v_0, and distribution as characterized by α for spectra taken for identical expansion conditions, but varying L, yield consistent values.

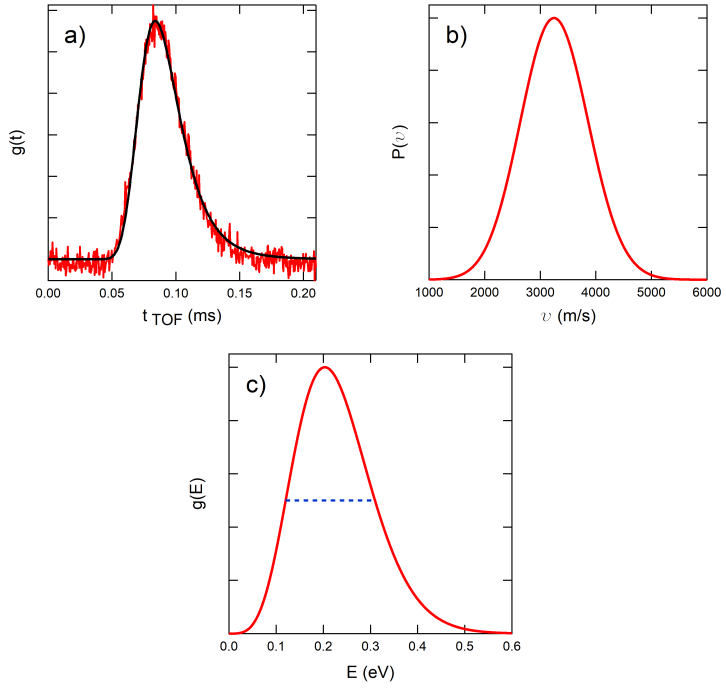

Figure 2.4: a) A typical TOF spectrum (red) and fit (black) in the time domain. b) and c) are the corresponding molecular beam's velocity distribution and energy distribution, respectively. The dashed blue line indicated the full width at half maximum.

We average values for v_0 and α for identical beam conditions and calculate the kinetic energy distribution by converting the velocity distribution to the energy domain:

$$g(E;T_n) = \frac{1}{m\sqrt{2E/m}} P_{vel}(v;T_n) \tag{2.9}$$

where $E = mv^2/2$.

Figure 2.4 shows a typical result of our TOF analysis for a pure D_2 beam. The horizontal dashed line in Fig. 2.4c) shows that the energy width in our beam in a typical experiment is substantial. The nozzle temperatures T_n were calculated from $\langle E_i \rangle = 2.7 \times k_B T_n$ assuming 20% rotational cooling and no vibrational cooling Ref. [16]. Comparison to temperatures measured 10-20 mm downstream the nozzle confirmed that, as expected, in most cases the nozzle temperatures determined from the relation stated above exceed the measured lower bounds, by values in the range 50-470 K. Nozzle temperatures were computed from the accurately determined average translational energies because physical constraints made it impossible to measure the nozzle temperature in our beam machine at the tip of our gas expansion tube. For the measurements reported here, as we noted, the thermocouple was attached 10-20 mm toward a cooling block and, therefore, it provided values significantly lower than the actual expansion temperatures. As the tip of the expansion tube is also hidden from view by heat shields, we could not use an optical pyrometer to measure the actual temperature near the nozzle's orifice. In previous experiments from nearly a decade ago, where the thermocouple was located significantly closer to the tip of a previous design, we measured ∼1800 K as the maximum obtainable temperature for nearly identical heating conditions. This maximum value is consistent with the maximum achieved nozzle temperature we determined from the average translational energies (1744 K).

2.2.4 Temperature programmed desorption

Temperature programmed desorption (TPD) is an experimental technique based on the crystal being heated in time. Species releasing from the surface are monitored.

The rate of thermal desorption is usually described by the Polanyi-Wigner equation:

$$r = -\frac{d\theta}{dt} = \nu(\theta) \cdot \theta^n \cdot exp(-\frac{E_{des}(\theta)}{R \cdot T}) \tag{2.10}$$

where r is the rate of desorption, θ the coverage, ν the coverage-dependent prefactor, E_{des} the coverage-dependent activation energy of desorption, and n the desorption order. In TPD, the temperature,

T, is generally ramped linearly

$$T = T_0 + \beta \cdot t \tag{2.11}$$

Figure 2.5 shows a simulation of TPD spectrum by solving equation 2.10 with the Runge-Kutta method.

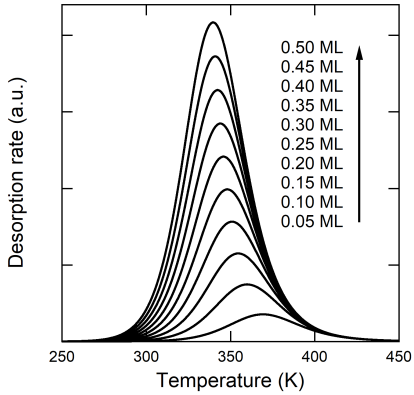

Figure 2.5: A simulation of TPD spectrum for a second order desorption. The parameters are: $E_{des} = 75.0$ kJ/mol, $\nu = 1 \times 10^{11}\ s^{-1}$, n = 2 and $\beta = 2$.

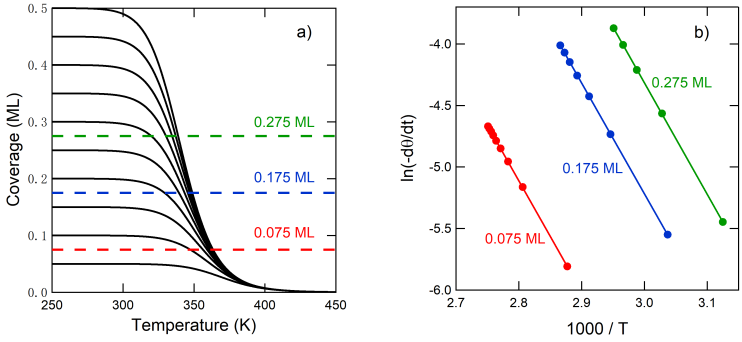

Figure 2.6: The 'complete analysis' of TPD spectrum. Figure a) shows the remaining coverage versus surface temperature. For every selected coverage, there is a pair of (r, T) values for every TPD trace. Figure b) shows the Arrhenius plot of $ln(-d\theta/dt)$ for the selected coverage.

Quantitative analysis of TPD spectra is complex as both E_{des} and ν in equation (2.10) may depend on coverage. By using the so-called 'complete analysis' method[17], we can determine E_{des} and ν for every

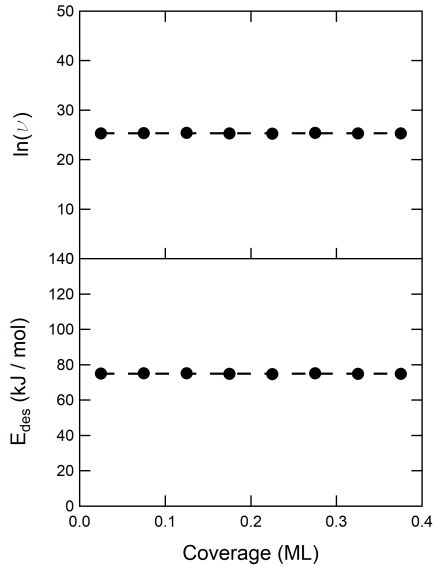

Figure 2.7: The prefactors and desorption energies obtained from 'complete analysis' at different coverage. The E_{des} is (75.00 ± 0.16) kJ/mol. The v is $(1.03 \pm 0.04) \times 10^{11}$ s^{-1}.

coverage. It requires changing equation (2.10) into

$$ln\ r = ln\ \nu(\theta) + n\ ln\ \theta - \frac{E_{des}(\theta)}{RT} \tag{2.12}$$

where the variables are the same as in equation (2.10). An Arrhenius plot of $ln\ r$ versus $1/T$ yields $-E_{des}/R$ as the slope. The intercept for any particular coverage equals $ln\ \nu(\theta) + n\ ln\ \theta$. The complete analysis of TPD spectrum shown in figure 2.5 is illustrated in figure 2.6 and 2.7. The results agree well with our simulation parameters.

2.3 Single crystals

In this thesis two types of single crystals are used. In chapters 3 and 4, we use flat single crystals, like Pt(111), Cu(111) and Cu(211). In chapters 5 and 6, we use a curved Pt(111) single crystal.

Figure 2.8 shows the flat Pt(111) crystal we used in chapter 3. The figure shows how we change the azimuthal angles. From LEED patterns we confirm that at azimuthal angle 0°, figure 2.8a), the azimuthal direction is $[11\bar{2}]$ and at azimuthal angle 30°, figure 2.8b), the

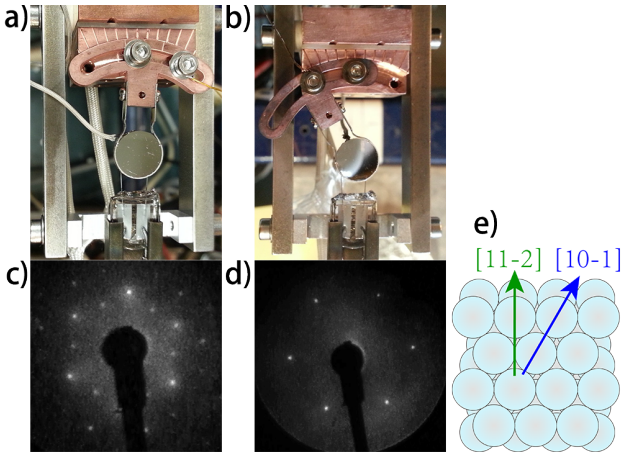

Figure 2.8: Illustration of how we change azimuthal angles on Potvis. Figure a) and b) correspond to azimuthal angle 0° and 30°, respectively. Figure c) and d) are the LEED patterns. Figure e) shows the azimuthal directions. Figure a and c correspond to $[11\bar{2}]$ direction. Figure b and d correspond to $[10\bar{1}]$ direction.

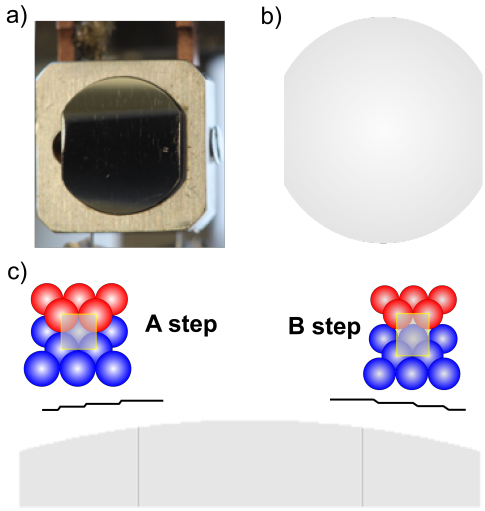

Figure 2.9: Illustration of curved Pt(111) single crystal. Figure a) and b) are the front views. Figure c) is the side view.

azimuthal direction is $[10\bar{1}]$.

Figure 2.9 shows the curved Pt(111) crystal we used in chapter 5 and 6. The crystal is cut and polished to expose a curvature encompassing $\sim 31°$ along the $[11\bar{2}]$ direction with the (111) surface at the apex. On one side the surface is Pt$[N(111) \times (100)]$, also called A step side. On the other side the surface is Pt$[N(111) \times (110)]$, also called

B step side. The length of (111) terrace decreases with distance from apex to both A and B step sides. In figure 2.9b, the height of the crystal is 8 mm and the width of the crystal is 7 mm.

Chapter 3

A molecular beam study of D_2 dissociation on Pt(111): testing SRP-DFT calculations

3.1 Introduction

The interaction between H_2 or D_2 with Pt surfaces has been a model system for dissociative chemisorption for a long time [18, 19]. In experiments scattering and diffraction, rotational excitation and selective adsorption, and dissociative adsorption (or sticking) have been studied[20–25]. In this study we focus on dissociative chemisorption at high energies of 0.1 to 0.5 eV on Pt(111). Not only on the close packed Pt(111) surface but also on stepped Pt surfaces hydrogen dissociation has been studied recently in detail[26–30]. The step edge introduces additional mechanism for adsorption near the step edge, that are irrelevant for the present study[31, 32].

Over the years theoretical studies have been carried out with increasing sophistication. The Born-Opperheimer Approximation has been demonstrated to work under these conditions[33–35]. This allows the separate calculation of a potential energy surface (PES) and dynamics calculations using a given PES. For adsorption studies, it is relevant to mention that the dimensionality of the calculations has increased over the years, from 2D (internuclear distance of H_2 and molecule surface separation assuming a structureless surface) to 6D: 3

intramolecular degrees of freedom and the 3D position of the molecule above the surface[36, 37]. Both quantum mechanical and classical calculations have been used to compute sticking coefficients[38].

Although in the past empirical PES have been used, recently the PES is computed by Density Functional Theory (DFT). The results show that the PES is elbow type and has an early barrier [36, 39]. The barrier height strongly depends on the lateral position of the molecule above the surface and the molecular orientation. Most recent calculations show that the barrier height can be as low as -0.008 eV on the top site to almost 0.5 eV on the hcp adsorption site[39]. This implies that adsorption can be barrier less, but because most surface sites show a small barrier towards sticking the system overall exhibits weakly activated sticking. Since the barrier height is site dependent, the PES shows energetic corrugation. In addition, the distance between the molecule and the surface at the barrier is also site dependent: thus, the PES also shows geometric corrugation. These terms have been introduced by Darling and Holloway[40, 41]. In general, strong energetic corrugation leads to a reduction of sticking with increasing parallel momentum, for constant normal energy $E_n = E_i cos^2(\Theta_i)$, where Θ_i is the incidence angle measured from the surface normal and E_i the beam energy. In contrast, strong geometric corrugation leads to an increase in sticking with increasing parallel momentum. The most recent theoretical calculations for this system have been carried out in the Kroes group, see[39]. Pijper et al. observe that their PES shows both energetic and geometric corrugation [36].

The group of Kroes proposed to allow an adjustable Specific Reaction Parameter (SRP) in the DFT functionals used, to obtain chemical accuracy in the DFT calculations and obtain good agreement between theory and experiment for several different observables[34, 42]. The method has been calibrated by Ghassemi et al. on normal incidence sticking data of D_2 on Pt(111) by Luntz et al[22]. The resulting SRP-DFT PES was tested on Luntz's data for non-normal incidence. The agreement between theory and experiment was very good, indicating that the SRP-DFT potential is very good. However, Luntz et al. did not specify the azimuthal orientation of the crystal with respect to the incidence plane of the beam. So the dependence of sticking on the azimuthal orientation of the crystal should be determined experimentally. The two most important orientations of the incidence plane (Φ) are $[10\bar{1}]$ and $[11\bar{2}]$, corresponding here to $\Phi = 30°$ and $\Phi = 0°$ The

theoretical prediction by Ghassemi et al. is that the differences will be very small, except at $\Theta_i = 60°$[39]. It is the aim of this paper to experimentally test the theoretical prediction and determine the azimuthal dependence of D_2 sticking on Pt(111).

3.2 Experimental

Experimental methods and our UHV-molecular beam system have been described before[30, 43–45]. Briefly, a triply differentially pumped molecular beam is aimed at the polished and cleaned (111) surface of a 10 mm diameter, 1 mm thick Pt single crystal kept in an ultrahigh vacuum (UHV) chamber. The energy of the molecular beam can be varied by heating the nozzle and by seeding D_2 in H_2 or inert gases, e.g. Ne, N_2 and Ar. An inline quadrupole mass spectrometer (QMS) with a cross-beam ionizer detects molecules in the beam. Using time-of-flight (TOF) techniques and a mechanical chopper, TOF spectra of the beam can be obtained. The distance between the chopper wheel and the ionizer can be adjusted continuously over 200 mm, to allow accurate determination of the offsets and delays in the flight time. We fit the TOF spectra in the time domain and represent the fit in the energy domain to extract the most probable energy and energy spread in the beam. From this data, we calculate the average energy, E_{avg}, of our beams when comparing to data from previous studies.

The Pt(111) surface is prepared with a mis-cut angle of less than 0.1° (Surface Preparaation Laboratory, Zaandam, the Netherlands). It is cleaned daily by multiple sputtering, oxidation, reduction, and annealing cycles. We sputter at 600 eV with $\sim 2.5\mu$A Ar^+ current during 5 minutes at a surface temperature, T_S , of 900 K. This is followed by a mild oxidation at the same surface temperature (2 minutes, $p(O_2) = 2 \times 10^{-7}$ mbar), H_2 reduction at the same surface temperature (2 minutes, $p(H_2) = 2 \times 10^{-6}$ mbar) and annealing at 1200 K for 5 minutes. Surface order is regularly verified by low energy electron diffraction (LEED, OCI Vacuum, BDL800IR-MCP) and cleanliness by Auger Electron Spectroscopy (AES, Staib Instruments DESA).

Sticking coefficients are obtained using the method of King and Wells (KW)[10]. We remove background signal from residual hydrogen prior to opening the UHV chamber to the differential stages of the supersonic molecular beam. We normalize the signal from the

molecular beam when it is admitted to the UHV chamber. We then inverting the time-dependent KW trace and fit the time-dependent reaction probability by a double exponential functional form starting at approx. 0.5–1.0 s after opening the beam flag. We extrapolate the fit backward to the exact time of opening this last flag and obtain the reaction probability from the fit. This procedure removes the convolution of the signal with the time required to fully remove the beam flag and the vacuum time constant of the UHV chamber for molecular hydrogen. The reported experimental error in the initial sticking coefficient is one standard deviation determined from repeating measurements under identical conditions.

3.3 Results and discussion

In Figure 3.1 the results for normal incidence are shown for T_S = 200 K. Our data are in good agreement with previous experiments by Luntz et al. and Samson et al. [21, 22]. In addition, we present results for two well-defined azimuthal orientations of the crystal. We note that there is very little difference between $\Phi = 0°$ and $\Phi = 30°$. This is to be expected as for normal incidence the sticking should be independent of Φ. The small differences observed should be due to imperfections of the crystal or the beam alignment. Our data for $\Phi = 0°$ and $\Phi = 30°$ indeed are the same within experimental error. The lines drawn through our data are quadratic fits and shown to guide the eye only. As discussed before, agreement between theory and experiment is very good, because the data by Luntz et al. were used to calibrate the SPR-DFT PES.

In Figure 3.2 data for off-normal incidence are presented, also for T_S = 200 K. Our data at $\Theta = 30°$ and both Φ values are in good agreement with the data of Luntz. The data for both Φ values are the same within experimental error. Only above 0.37 eV do we find that Luntz's data are slightly higher than ours. A source of discrepancy for high nozzle temperature H2 (D2) molecular beams may be differences in the energy dispersion, causing variation in the convolution with the energy-resolved sticking probability[34].The theory of Ghassemi et al.[39] follows Luntz's data. Our data at $\Theta = 40°$ and both Φ values are in good agreement with the data of Luntz for $\Theta = 45°$. Our data at $\Theta = 50°$ and both Φ values fall in between the data of Luntz

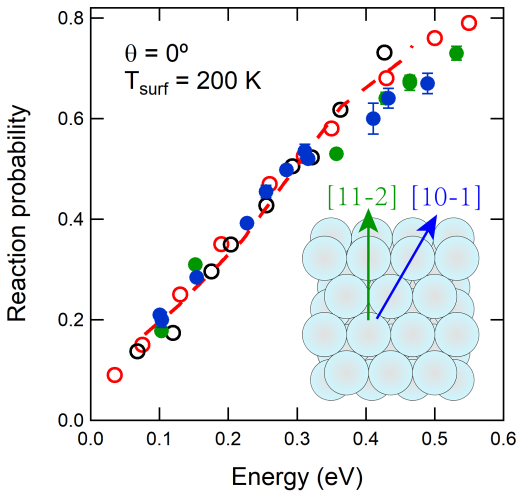

Figure 3.1: Energy dependence of the dissociative reaction probabilities of D_2 on Pt(111). Solid circles are our data, the color indicating the azimuthal directions as shown in the inset. The black and red open circles are the experimental data from Samson et al.[21] and Luntz et al.[22], respectively. The red dashed line reproduces the results of dynamical calculation from Ghassemi et al.[39]. Represented energies are the averages of energy distributions calculated from TOF distributions. Error bars indicate one standard deviation for repeated measurements. For single measurements, no error bar is shown.

for $\Theta = 45°$ and $\Theta = 60°$. Because of the different Θ values, direct comparison is not possible. The Luntz's data again seem slightly higher than ours at energies above 0.35 eV. The lines drawn through our data are again quadratic fits to guide the eye.

At $\Theta = 50°$, the data in Figure 3.2 suggest a slight difference for sticking at $\Phi = 0°$ and $\Phi = 30°$. The resulting sticking curves are shown with an expanded scale in Figure 3.3. At $\Theta = 50°$, the difference between $\Phi = 30°$ and $\Phi = 0°$ is small with sticking at $\Phi = 30°$ being slightly higher. With barrier heights being equal, this implies a slightly different geometrical corrugation felt by trajectories along the two different azimuths.

The PES shows that there is an almost complete absence of a precursor well[39]. The average well depth for physisorption is 0.072 eV[39]. This implies that precursor-mediated dissociative adsorption is not possible at $T_S = 200$ K. This is qualitatively confirmed by the work of Poelsema et al. where only at 25 K significant adsorption is observed [20]. The absence of a deep well also implies that there is no

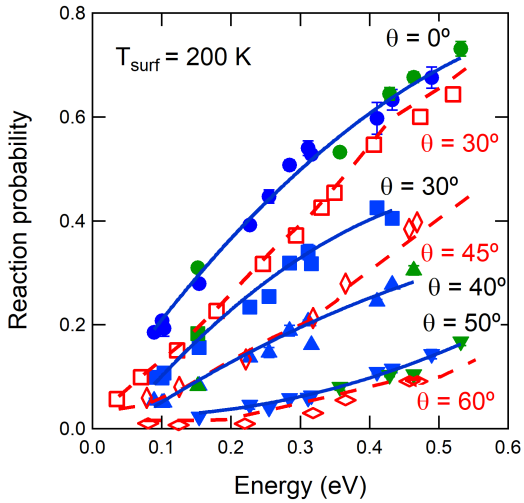

Figure 3.2: The dissociative reaction probability dependence on kinetic energy for various polar and azimuthal angles. The solid symbols are our data. Polar angles are indicated by the black text. The color of the solid symbol indicates the azimuthal angle as in figure 3.1. The solid lines are quadratic fits to guide the eye. The open symbols reproduce the experimental data from Luntz et al.[22]. The dashed lines reproduce results of dynamical calculations from Ghassemi et al.[39]. The red text indicates their polar angles.

T_S dependence of the sticking probability. This is confirmed by the data presented in Figure 3.4. No significant T_S dependence is seen. In addition, in the sticking curves as a function of energy no evidence of the presence of a precursor state is seen. This is also in agreement with the studies of Gee et al., and Groot et al. for stepped Pt(111) surfaces[26, 28–30]. These authors observed significant sticking at low beam energies, that decreases with increasing beam energy. This was attributed to the presence of a deeper molecular chemisorption well near the step edge.

3.4 Conclusion

There is excellent agreement between our data and earlier experimental work. Our work demonstrates that the interaction only weakly depends on the azimuthal orientation of the incidence plane. Our data is entirely consistent with the SRP-DFT calculations on D_2 on Pt by Ghassemi et al[39]. It demonstrates that the SRP-DFT methodology

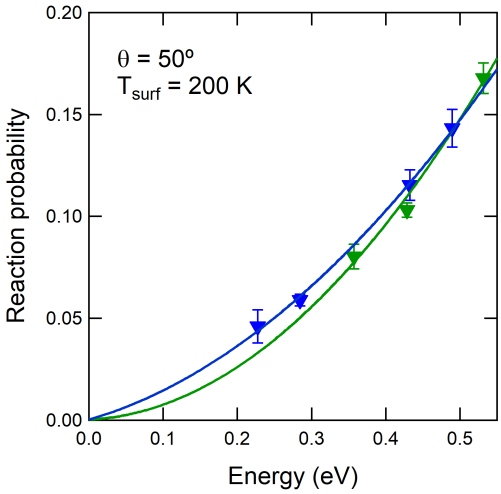

Figure 3.3: Reaction probabilities versus kinetic energy at 50° polar angle for both azimuthal angles. Colors for the azimuthal angle are used as in figures 3.1 and 3.2. Error bar are standard deviation determined from multiple measurements at identical conditions.

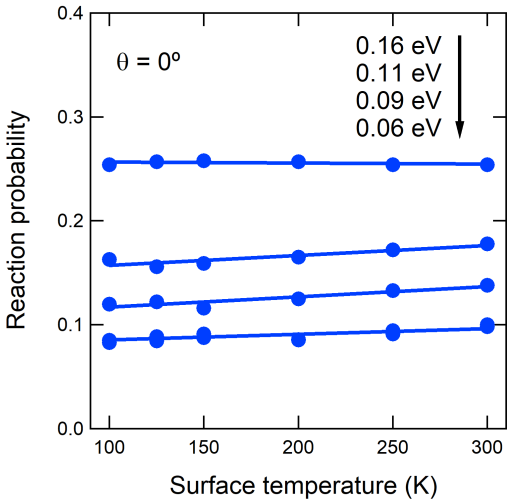

Figure 3.4: The surface temperature dependence of the dissociative reaction probability on Pt(111) for incident energies as indicated in the figure.

works for this system at the level of the azimuthal dependence of the sticking probability for non-normally incident beams. There are possibly small discrepancies at large polar incidence angles and high energies. More detailed, focused experiments and calculations are needed

to investigate if there is a significant difference between theory and experiment for those special conditions.

Chapter 4

Hydrogen adsorption and desorption from Cu(111) and Cu(211)

4.1 Introduction

Few chemical reactions occurring at the gas-surface interface have been studied with similar intensity as hydrogen dissociation on Cu. It serves as the model system for strongly activated dissociative adsorption of a simple diatomic molecule on a metal surface [18, 34]. In recent years, however, it has also become of practical importance. The industrial hydrogenation of CO_2 to methanol over a $Cu/ZnO/Al_2O_3$ catalyst, is considered to be rate-determined by elementary hydrogenation steps involving dissociated hydrogen[46–48]. The industrial process presents a potential means to fixate CO_2. However, it currently suffers from high pressure and moderate temperature requirements[46]. A thorough understanding of all elementary reaction steps involved may advance the development of new catalysts that operate at less energy-consuming conditions. The dissociation of molecular hydrogen on (defective) Cu surfaces is such an elementary step that is crucial to the reaction.

Using supersonic molecular beam (SMB) methods and temperature programmed desorption (TPD), Anger, Winkler, and Rendulic showed for low Miller surfaces that the reactivity order toward H_2 dissociation is Cu(111) > Cu(100) > Cu(110)[49]. Sakong and Groß reproduced this trend in a theoretical study of atomic hydrogen adsorption and H_2 dissociation[50]. For the most intensely studied Cu(111) surface

in this context, Winkler's group also initiated studies on vibrational effects to hydrogen dissociation [51]. Auerbach, Rettner and Michelsen subsequently combined SMB, permeation and laser-based techniques to study adsorption and desorption in a state-specific manner[52–59]. Their studies showed, amongst others, that the vibrational motion plays a large role in the dissociative adsorption. They also demonstrated the applicability of the principle of detailed balance, that is, that adsorption and desorption experiments are similarly accurate at determining important kinetic and thermodynamic quantities of the reaction. In the same decade, Darling and Holloway carried out a series of theoretical studies on rotational, vibrational, and surface temperature effects to dissociative adsorption[40, 60–63]. While they could achieve qualitative agreement with experimental results on the importance of individual molecular degrees of freedom for the dynamics, an acceptable quantitative agreement regarding absolute reactivities was, however, then not attainable. More recently, Díaz et al. continued theoretical studies based on the specific reaction parameter (SRP) approach to density functional theory (DFT)[34, 64]. Their dynamics calculations performed for the H_2 + Cu(111) system accurately reproduced experimental results on sticking, the effect of molecular vibrational and rotational motion on dissociative adsorption and associative desorption, and the amount of rotational excitation of scattered molecules.

Experimental studies of the influence of defects on H_2 dissociation on Cu are sparse. In an early study, Balooch et al. observed that the highly corrugated Cu(310) surface does not exhibit higher HD yields than the Cu(100) surface when exposed to molecular hydrogen and atomic deuterium[65]. They suggested that the edges on this stepped surface are not the principal regions for H_2 adsorption. Theoretical studies performed on similar systems have found the opposite. Using an embedded-atom method (EAM) and a cluster of 800 Cu atoms, Liao and Sun computed a significant decrease for the H_2 dissociative barrier for the Cu(410) plane in comparison to the Cu(100) plane [66]. Šljivančanin and Hammer performed calculations on the reaction barrier for H_2 dissociation on Cu surfaces constructed from the most narrow (111) terrace with A- and B-type steps, that is, Cu(211) and Cu(221), for kinks in step edges, and for vacancy sites in the Cu(111) plane[67]. They found that all types of defects lowered the H_2 dissociation barrier in comparison to the flat Cu(111) surface. A

reduced dissociation barrier for Cu(211) compared to Cu(111) was also predicted by calculations of Behrens et al. based on density functional theory (DFT) that focused on the mechanism of CO_2 hydrogenation [48]. Such increased reactivity for stepped metal surfaces is often rationalized using the d-band theory[68, 69], the important parameter being the position of the d-band relative to the Fermi level.

Recently, we have co-authored a combined theoretical and experimental study on the reactivity of D_2 on clean Cu(211) and Cu(111) surfaces at zero-coverage[70]. Based on ∼115,000 DFT energy points calculated using the SRP48 functional[71], a new potential energy surface (PES) was constructed for the H_2 + Cu(211) system. Surprisingly, subsequently performed molecular dynamics simulations using this PES showed in agreement with new SMB measurements that hydrogen dissociation is more likely on the flat Cu(111) surface than on the stepped Cu(211) surface. The observed lower reactivity of the stepped surface for bond cleavage of molecular hydrogen was rationalized by somewhat larger reaction barriers that were computed for H_2 + Cu(211) and the overall increased complexity of the underlying gas-surface interaction potential in comparison to the H_2 + Cu(111) system.

In the following, we present an experimentally more comprehensive set of data obtained using a combination of SMB techniques and TPD for Cu(211) and Cu(111). The former is a highly corrugated surface with 3-atom wide (111) terraces, which are separated by the monoatomic steps representing a (100) facet. They are also referred to as A-type steps. The additional TPD experiments not only allow us to extend the range of detectable probabilities for dissociative adsorption, we also infer activation barriers to desorption, their surface coverage dependence, and a relation between the obtained saturation coverage and incident energy. Our experimental data is supplemented by additional periodic DFT calculations that probe how the activation barrier energy is modified by different surface concentrations of atomic hydrogen pre-adsorbed on the two different surface facets. Our results contribute to the present knowledge regarding the effect of steps and defects on the reaction dynamics of gas-surface systems.

4.2 Experimental and theoretical methods

4.2.1 Molecular beam apparatus and experimental methodology

All experiments were carried out using a home-built UHV system with a base pressure below 8×10^{-11} mbar. The main UHV chamber is connected to a series of vacuum chambers used to generate a well-defined molecular beam through supersonic expansion of molecular hydrogen (deuterium). We use as our expansion nozzle a 25 μm diameter orifice, laser drilled through the flat end wall of a hollowed single crystalline tungsten rod. This tungsten tip is laser welded to a 100 mm long tantalum tube which is held at the opposite end by a large stainless steel block suspended from an *x, y, z* manipulator. The nozzle's 25 μm diameter orifice is accurately positioned at variable distance (between approx. 1 and 15 mm) from the first of this series of skimmers (Model 1, 0.25 mm, Beam Dynamics). We create the supersonic expansion into vacuum by flowing gases from a gas manifold using flow controllers and pressures between 1 and 5 bara into the Ta-W tube. To increase the kinetic energy of molecules in the expansion, the tungsten tip of the nozzle is heated radiatively by a second short tungsten tube that surrounds the tungsten tip. This second tube is heated by electron bombardment using two oppositely positioned filaments. A C-type thermocouple is spot welded to the Ta part of the expansion tube, approx. 10-20 mm from the 25 μm diameter orifice. A strong thermal gradient along the expansion tube leads to a temperature reading for the nozzle, T_n, below the actual temperature at the orifice.

We skim the gas expansion in the source chamber to create a beam which passes through two stages of differential-pumping prior to entering the UHV chamber, which houses a temperature-controlled Cu single crystal on an *x, y, z,* θ manipulator. A valve separates the two differential pumping stages. When closed, the background pressures for H_2 and D_2 in the main chamber are determined. Two additional flags in the beam line can be opened and closed. They are used to determine the absolute dissociation probabilities by the King and Wells (KW) technique[10]. For KW measurements, we use a Baltzers quadrupole mass analyzer (QMA200), positioned such that it samples the pressure rise from the SMB after equilibration inside the chamber. The first

flag is located in the first differential pumping stage. When closed, the effusive load of the beam onto the main UHV chamber can be determined. As a second flag, we use a wheel located inside the main UHV chamber. It has a 50% duty cycle divided over two "open" sections of equal size. It is firmly attached to the axis of a UHV-compatible stepper motor (Arun Microelectronics) and used, here, only to control impingement of the beam onto the crystal within the UHV chamber in an "on/off" fashion by a single, step-wise rotation of the wheel over one quarter turn. The opening and closing of both flags is computer-controlled to ensure an accurate timing. When retracting the sample, the beam enters the differentially-pumped housing of a Baltzer's 400 quadrupole mass analyzer (QMA400) of a special linear design with a cross-beam ionizer and two consecutive quadrupole mass filters. It is used to determine the kinetic energy of molecules in the beam through time-of-flight (TOF) analysis and for TPD. The differentially-pumped QMA is retractable over 200 mm along the beam axis, allowing TOF measurements for varying neutral flight path lengths. The kinetic energy distribution of molecules in each SMB used to determine sticking probabilities is determined as described in detail in the Supporting Information of Ref. [70]. For the analysis, we assume the standard form for a flux-weighted velocity distribution and take into account that our QMA ionizer is a density-sensitive detector. We also incorporate the chopper function in the fitting procedure. More details of our entire UHV-SMB system were previously described in Ref.[11].

In this work, we use two copper single crystals exposing polished (111) and (211) surfaces. They are 10 mm in diameter, 1 mm thick, of 6N purity, and aligned to $< 0.1^\circ$ from the indicated surface (Surface Preparation Laboratory, Zaandam, The Netherlands). They can be heated at least up to 900 K by electron bombardment heating. They can be cooled to 90 K using liquid nitrogen. The Cu crystals are attached to the sample holder in a way that allows us to adjust the azimuthal angle with an accuracy $\sim 2^\circ$. The polar angle of incidence may be changed up to $\sim 60^\circ$ with an accuracy of $\sim 0.5^\circ$. The surface structure and azimuthal orientation were verified by low energy electron diffraction (LEED). The spot-splitting to row-spacing ratio for the (211) surface was found to be 2.47, in very good agreement with the expected value of 2.45[72]. Cleanliness is checked regularly using Auger electron spectroscopy (AES) (OCI Vacuum, BDL800IR-MCP). Cleaning procedures were identical for both surfaces. We use repetitive

cycles of argon ion sputtering at a surface temperature (T_s) of 400 K and at normal incidence (10 minutes, ~ 1 μA) with subsequent annealing at $T_s = 800$ K for another 10 minutes. This procedure is repeated at least three times before experiments were performed. We combined each measurement of the absolute dissociation probability, S, with a subsequent TPD measurement. We then heated the Cu crystal to 800 K to remove adsorbates. For beam conditions that lead to dissociation probabilities near or below our detection limit, we determine the initial dissociation probability, S_0, by averaging up to 10 independent measurements. This reduces our KW detection limit for S_0 to ~ 0.005. To determine even lower dissociation probabilities, we use the integrated signal of TPD spectra as discussed in detail in the Results section given below.

TPD spectra are taken after exposing the surface to $H_2(D_2)$ for a well-defined time using the molecular beam. In this work, we solely report on TPD spectra from dosing using the SMB - the reactivity is too low to achieve comparable surface coverages from background dosed hydrogen applied at acceptable pressures and exposure times. Dissociative adsorption was probed at normal incidence of the molecular beam and all TPD spectra were taken with the QMA's axis aligned with the crystal's surface normal. The SMBs were generated using pure H_2 (6N, Linde Gas, Rotterdam, The Netherlands) or pure D_2 (2N8 isotopic purity, Linde Gas, Rotterdam, The Netherlands) without further treatment. The rate of heating for all reported TPD spectra was determined to be 2.0 K s^{-1}. The distance between the Cu crystal's polished surface and the 3.0 mm diameter aperture of the QMA housing is kept constant at ~ 2 mm. The reduced pumping speed in between the crystal's surface and the aperture, and the low pumping speed surrounding the QMA's ionizer inside its differential housing, allows this configuration to be taken to be (near) angle-integrating.

4.2.2 Computational methodology

Periodic DFT calculations were carried out using the Vienna ab initio simulation package (VASP)[73–76] and the SRP48-functional. We are particularly interested in changes of the classical activation energy for the dissociation of H_2 on Cu(111) and Cu(211) caused by the presence of pre-adsorbed hydrogen atoms at coverages of 1/9 and 2/9 ML. For calculations on the H_2 + Cu(111) system,we chose a (3×3) supercell

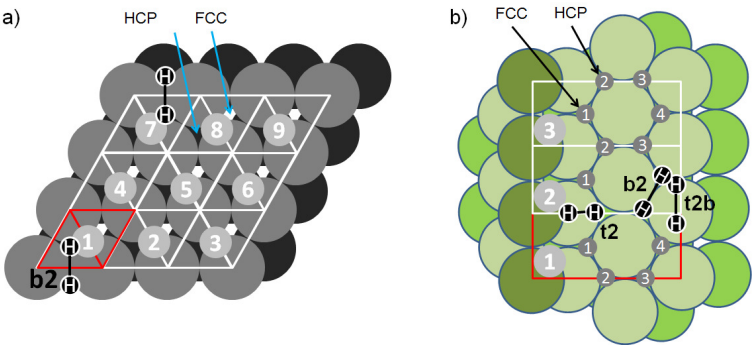

Figure 4.1: Shown are in a) the (3×3) supercell for Cu(111) and in b) the (3×1) supercell for Cu(211) as used in the calculations. Light grey filled circles with numbers label the different unit cells. In b), smaller darker grey circles with numbers indicate H_{ads} positions. Also indicated in black stick models are the geometries of transient H_2 molecules assumed at the different barriers that were considered in this work, i.e. the b_2 site for Cu(111) and the t_2, b_2, and t_2b sites for Cu(211).

and a k-point mesh of $6 \times 6 \times 1$. Further details on the slab model and the applied computational setup are given in ref.[71]. Calculations on H_2 + Cu(211) were performed using a (3×1) supercell and the same 5 layer slab model and the same computational setup as described in Ref. [70]. The supercells are shown in figure 4.1 as well as the corresponding smallest unit cells distinguished by the numbers embedded in the gray circles.

To compute the coverage dependence of the activation barrier we proceed as follows. For the Cu(111) surface, we place the transient H_2 molecule at the transition state geometry specified in Ref.[77] and indicated in figure 4.1a) at the b_2 site. In the case of Cu(211), we select the geometries of transient H_2 associated with the barriers at the b_2, t_2 and t_2b sites, which we have previously found to play an important role in the dissociation process[70]. The corresponding H_2 geometries are also indicated in figure 4.1b). Coverages of 1/9 ML on Cu(111) were simulated by placing a single hydrogen atom in one out of the nine unit cells at either the FCC or the HCP position, see figure 4.1a). We neglect situations in which H_{ads} would lead to strong repulsive interactions with the H_2 molecule and have therefore not considered coverage-configurations over the unit cells 1 and 7 of Cu(111), see figure 4.1a). On Cu(211), we proceed similarly and put H_{ads} at selected local minima in a manner that repulsive interactions with transient H_2 are kept small. According to our DFT calculations,

the four different minima for hydrogen atom adsorption on Cu(211) as indicated by encircled numbers in figure 1b) follow the stabilization order $4 > 3 > 2 > 1$ whereby the hollow site located near the step edge, i.e. site 4, is the preferred adsorption site for a single hydrogen atom. To simulate coverages of 2/9 ML, we placed another H_{ads} at a proper position on the supercell while carefully avoiding too large H_{ads}-H_2 and H_{ads}-H_{ads} repulsions. This procedure leads to pre-covered surfaces of different surface structures that have all been considered in the calculations. The computed reaction barriers therefore vary within a certain energy range, and effective barriers represent averages over all barriers calculated for the different adsorbate layer structures. The calculated reaction barrier energies are given with respect to the potential energy that the system assumes when the H_2 molecule is moved to the gas phase (here 6 Å away from the Cu-surfaces) at its classical equilibrium position (H-H distance is ∼0.74 Å). We note that the considered reaction barrier geometries were not reoptimized in the presence of pre-adsorbed hydrogen. Normal mode analyses rigorously performed for almost all the different coverage configurations revealed that the barriers toward H_2 dissociation considered here remained first order saddle points. This makes the approach of using fixed TS geometries reliable in the computation of the coverage dependence of the activation energies.

4.3 Results

4.3.1 Initial dissociation probability by the King and Wells method

In figures 4.2a) and 4.2b), we exemplify our procedure to determine S_0 at conditions where the sticking probability is too low to be accurately determined by a single KW measurement. Note that the QMA signal in figure 4.2a) shows only the upper 10% of the relative increase in hydrogen partial pressure when the molecular beam enters the main UHV chamber. Inset I of figure 4.2a) shows a single measurement plotted over the entire QMA signal. The data is normalized and corrected for the background pressure of molecular hydrogen present in the main UHV chamber. Data presented as a solid black line in the main plot of panel a) represent the average of multiple measurements shown in

red. One can see that the small dip appearing at 16 s - the moment in which the exposure of the surface to H_2 starts - can only be resolved after averaging multiple measurements and proper magnification of the averaged signal.

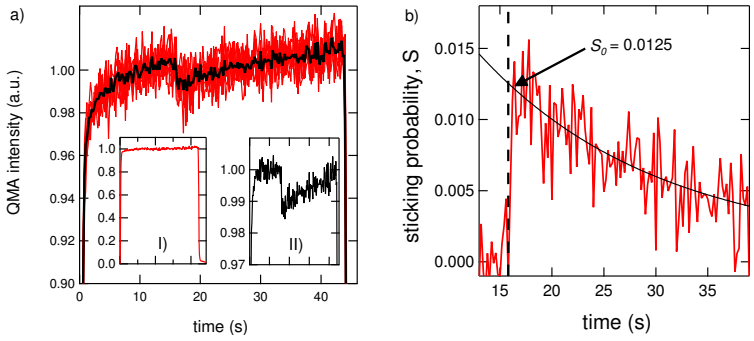

Figure 4.2: Illustration of the applied procedure to determine dissociative sticking of H_2 on Cu(111) by the King and Wells technique. Recorded QMA signals as function of the exposure time are plotted in panel a). Red curves show ten independent KW measurements. The black curve is the corresponding average result. The main panel shows the upper 10% of the full range of the normalized QMA intensity change when admitting the SMB to the UHV chamber. In inset I, the time-dependence of a single measurement is shown over the full range. Inset II shows the average signal after correcting for the change in QMA sensitivity resulting from reduction of the channeltron's inner surface. Panel b) shows the sticking probability, S, as a function of exposure time. The solid black curve is a fit to the data used to extract the indicated value of S_0 at the time of opening the beam flag. The latter is indicated by a vertical dashed line.

We subsequently correct for the small but noticeable increase of the hydrogen partial pressure over longer times. The small continuing rise is hardly noticeable in inset I, but is clearly visible in the top 10% of the pressure versus time trace. We do not believe that it represents an actual partial pressure rise, e.g. generated by slow equilibration of poorly pumped spaces in the UHV chamber. The time constant of the gradual change is too long. Instead, we attribute it to improving amplification of the QMA's channeltron through reduction of its inner surface by exposure to the reducing gas, H_2. We have observed the opposite effect in a study on the dissociation of O_2 dissociation on Pd(100) using the same type of QMA[14]. We correct for this increase in QMA sensitivity by fitting the time-dependent pressure using an exponential form and dividing the data by this exposure-dependent sensitivity function. In the fitting procedure, we mask the part of the data near the dip in

pressure resulting from dissociative adsorption. We have verified that the change in QMA sensitivity is consistent over multiple days and that the fitting function used here reproduces the pressure versus time trace recorded at conditions leading to no discernible dissociation. The upper 10% of the resulting corrected trace is shown in inset II of figure 4.2a). We finally invert the signal and fit the dissociation probability over time. The fit is of a double-exponential form and shown in figure 4.2b) as a black trace. The latter procedure reduces small errors introduced by the convolution of the actual time-resolved dissociation probability, $S(t)$, with the time constants for opening the second shutter and the gating time of QMA data collection. We estimate that the so-determined S_0 values are accurate to at least two significant figures.

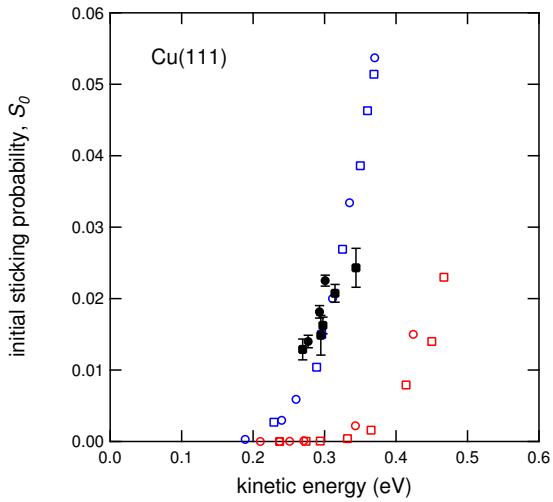

Figure 4.3: Initial sticking probability data for for D_2 (squares) and H_2 (circles) dissociation on Cu(111) from refs. [49, 51] (open blue) and [53, 78] (open red) and current data (solid black) as a function of incident kinetic energy. Error bars reflect the uncertainty from the time-dependent fit as described in figure 4.2b). Kinetic energy for current data represents the most probable kinetic energy from TOF fitting, whereas [53, 78] imply the average kinetic energy.

Figure 4.3 compares our initial sticking probability data for D_2 on Cu(111) to data published previously for dissociative sticking of hydrogen and deuterium to this surface [51, 53, 78]. Our data are shown versus the most probable energy of the energy distribution as determined by time-of-flight and indicated by squares. Error bars reflect the uncertainty in the fit of time vs S traces as shown in figure 4.2b). As

will be shown below, the energy distributions in our beams are rather broad, especially when using high nozzle temperatures. The data published by Berger et al. for H_2 (open blue circles) and D_2 (open blue squares) unfortunately lack a definition of their energy axis, although they indicate that the kinetic energies of their beams were determined using time-of-flight techniques. They do not show typical results for an energy distribution, but specify that the energy is $\sim 5kT_n/2$, with k being Boltzmann's constant. Rettner and Auerbach published time-of-flight spectra [79] and indicated 2.65k as the linear scaling factor between energy and nozzle temperature[52]. Their data for H_2 (open red circles) and D_2 (open red squares) are shown versus the mean energy of their characterized beams. While our data agrees rather well with those from Berger et al., they are clearly considerably higher than those from Auerbach and coworkers. In the Discussion section, we explain the origin of this apparent discrepancy.

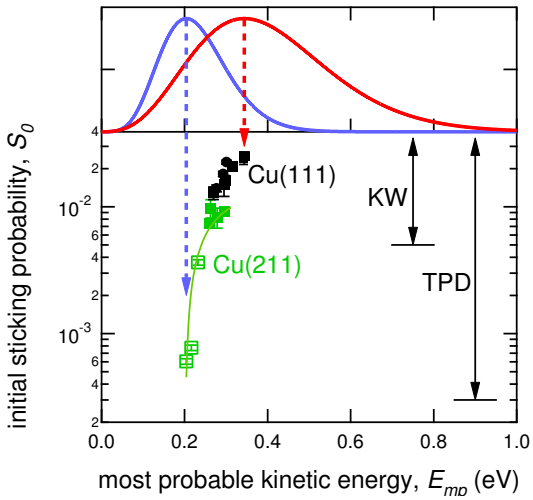

Figure 4.4: The top panel shows two energy distributions obtained from TOF analyses for two representative pure D_2 beams obtained at different nozzle temperatures. Their most probable energies E_{mp} are indicated by the vertical dashed lines. The bottom panel plots initial sticking coefficients, S_0, for H_2 (circles) and D_2 (squares) as function of E_{mp} for Cu(111) (black filled symbols) and for Cu(211) (open green symbols). The range over which absolute reactivity is determined by KW measurements is indicate by a vertical bar in the lower panel. Relative values were established with TPD measurements over the range indicated also by a vertical bar. The solid green line in the bottom panel is a fit of exponential functional form to the data for D_2 dissociation on Cu(211) serving to guide they eye.

Figure 4.4 compares our absolute dissociative sticking probabilities of D_2 (H_2) for Cu(111) as plotted in figure 4.3 to Cu(211). To illustrate that our measurements are not energy-resolved, we show in the upper panel of figure 4.4 two kinetic energy distributions for pure D_2 beams generated at different nozzle temperatures. We previously reported a linear relation between the kinetic energy and nozzle temperature with 2.53k as the scaling factor for our molecular beam system.[45] As we have lost the ability to measure the actual expansion temperature due to changes in the nozzle design, we cannot determine the scaling factor. However, the energy distributions are very similar to those obtained earlier for similar expansion conditions and assuming only an offset in the temperature measurement. In the lower panel of figure 4.4, we plot initial sticking coefficients versus the most probable kinetic energy, E_{mp}, of the associated molecular beams. For H_2 and D_2 impacting on Cu(111) we again use black circles and squares, respectively. For D_2 dissociation on Cu(211), we have used solid green squares for data obtained by KW technique. Data determined by the KW method provides absolute values, but are limited to values larger than 0.005. These data serve to determine lower S_0 values obtained from integrated TPD spectra, as explained in detail below. The latter are shown as open green squares. The solid green line is an exponential fit to the data and included to guide the eye. The data in figure 4.4 show that the Cu(111) surface is significantly more reactive in dissociating hydrogen than Cu(211). The difference is approximately a factor of 2 in the regime where we have been able to collect data by the KW method reproducibly for both surfaces under identical expansion conditions.

We have attempted to widen the kinetic energy range over which we can determine S_0. Attempts to increase reactivity by seeding small amounts of D_2 in H_2 while expanding at the highest attainable nozzle temperatures failed. With abundant H_2, the tungsten tip of our nozzle converts nearly all D_2 into HD through reaction at its inner surface prior to expansion. It leaves too little D_2 in the gas mixture to allow KW measurement of S_0 at higher incidence energy. On the lower kinetic energy side, the limited flux of D_2 molecules in our molecular beam prevents detecting lower reactivities. Exposure times needed to obtain a measurable quantity of D_2 in TPD spectra became too long to guarantee surface cleanliness. For example, CO in the residual gas of our UHV system sticks to the Cu surfaces at the temperatures required for the molecular beam adsorption measurements.

Considering the width of the kinetic energy distributions in our beams and the significant difference in expansion temperatures required to vary the most probable kinetic energy in our experiments, the determined dissociation probabilities seem to be dominated by the high energy tail of the distribution and/or ro-vibrationally excited molecules. Although it is in principle possible to deconvolute the data in figure 4.4 for incident energy and vibrational state[53], we do not. The energy distributions in our beams are too broad, the measured temperature of the nozzle does not represent the actual expansion temperature, and our data set is too limited to yield reliable results. Therefore, we leave this data as qualitatively indicating the surprising result of lowered reactivity by introducing (100) type steps at a high density to the (111) surface, and try to reveal its origin using quantitative TPD.

4.3.2 Temperature programmed desorption

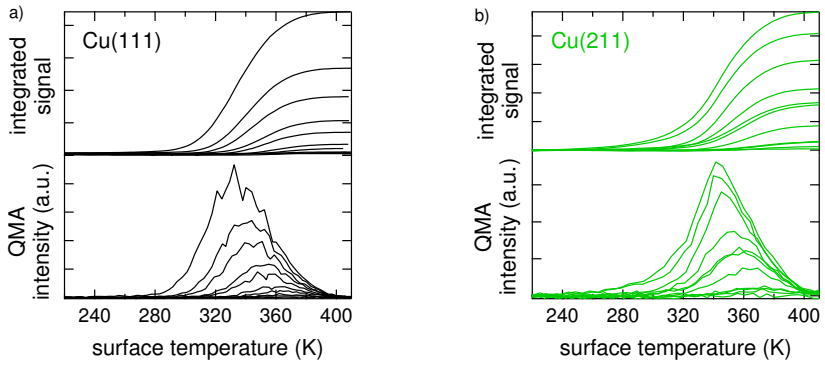

Figure 4.5: At the bottom, TPD spectra are shown for various pure D_2 molecular beam doses at T_s = 90 K onto a) Cu(111) and b) Cu(211) for E_{kin} = 0.298 eV. The integrated spectra are shown in the top panels.

Figure 4.5a) exemplifies background-subtracted D_2 TPD spectra (bottom) and the temperature-integrated spectra (top) for various doses from the molecular beam under fixed expansion conditions onto Cu(111) for a most probable beam energy of 0.298 eV. Figure 4.5b) shows the same for Cu(211) for the identical kinetic energy and energy distribution. The peak desorption temperature shifts for Cu(111) downward from $\sim$ 365 K to $\sim$ 330 K with increasing coverage. Trailing edges overlap mostly. The Cu(211) surface shows the same behavior for

desorption temperatures that are $\sim$ 10 K higher. Overlapping trailing edges are characteristic for second order desorption kinetics with negligible adsorbate-adsorbate interactions. For the highest doses, Cu(211) shows a clear shoulder developing at the low temperature side of the major desorption peak. The onset of desorption for the highest D-coverage is located around 260 K. Cu(111) shows no desorption in this temperature regime even after extended doses at the indicated kinetic energy.

The rate of thermal desorption is usually described by the Polanyi-Wigner equation, as equation (2.10) and equation (2.11) show in chapter 2.

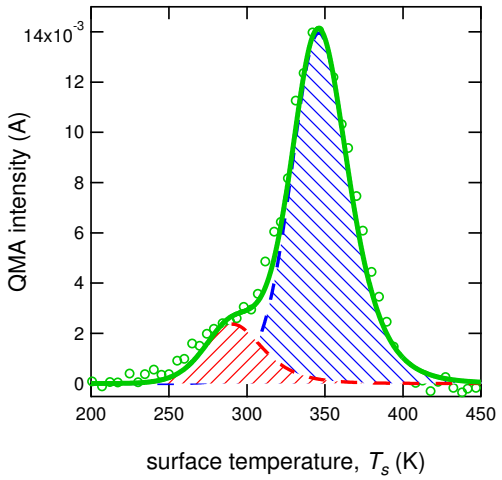

Figure 4.6: Runge-Kutta based simulation of an experimental D_2 TPD spectrum for Cu(211). Experimental data are shown as open circles. The solid green line equals the sum of two separate contributions. The parameters used for the main peak (dashed blue) are $E_{des} = 75.5$ kJ/mol, $\nu = 1 \times 10^{11}$ s^{-1}, $\theta_0 = 0.35$ ML, and $n = 2$. For the shoulder (dashed red), $E_{des} = 52$ kJ/mol, $\nu = 5 \times 10^9$ s^{-1}, $\theta_0 = 0.06$ ML, $n = 2$.

Quantitative analysis of TPD spectra is complex as both E_{des} and ν in equation (2.10) may depend on coverage. To obtain an estimate of the desorption energy for the main peak and shoulder observed at higher coverages for Cu(211), a TPD spectrum was initially simulated by solving equation (2.10) with the Runge-Kutta method. For the simulation, we assume that ν and E_{des} are independent of coverage. We also distribute the total initial coverage, θ_0, (here 0.41 ML) over the two apparent desorption peaks. Figure 4.6 shows the spectrum

with experimental data indicated by open circles. The red curve is the simulation of the shoulder peak and the blue curve the simulation of the main peak. The green curve is the summation of the two individual peaks. The parameters used for this simulation are $E_{des} = 75.5$ kJ/mol, $\nu = 1 \times 10^{11}\ s^{-1}$, $\theta_0 = 0.35$ ML, $n = 2$ and $E_{des} = 52$ kJ/mol, $\nu = 5 \times 10^{9}\ s^{-1}$, $\theta_0 = 0.06$ ML, $n = 2$ for the main peak and shoulder peak, respectively. Increasing E_{des} for the shoulder requires increasing ν in order to keep the simulation and TPD spectrum comparable. However, the width of the simulated shoulder visibly becomes too narrow in comparison to the TPD spectrum. With the indicated parameters, the shoulder peak's area is less than 15% of the total area. The desorption energy difference for the two peaks is approximately 23.5 kJ/mol.

Using the so-called 'complete analysis' method[17], we can determine E_{des} and ν for every coverage. It requires changing equation (2.10) into equation (2.12). An Arrhenius plot of ln r versus $1/T_s$ yields $-E_{des}/R$ as the slope. The intercept for any particular coverage equals ln $\nu(\theta) + n$ ln θ. Figure 4.7 exemplifies a subset of the results when applying this procedure to TPD spectra taken for associative D_2 desorption from Cu(211). We randomly choose a coverage, θ', and find pairs of (r, T_s) data corresponding to this θ' on all TPD curves starting with an initial coverage, θ_0, larger than θ'. Figure 4.7b) shows an Arrhenius plot of all ln r (i.e. ln $d\theta/dt$) versus $1/T_s$ for three random coverages indicated in Figure 4.7a).

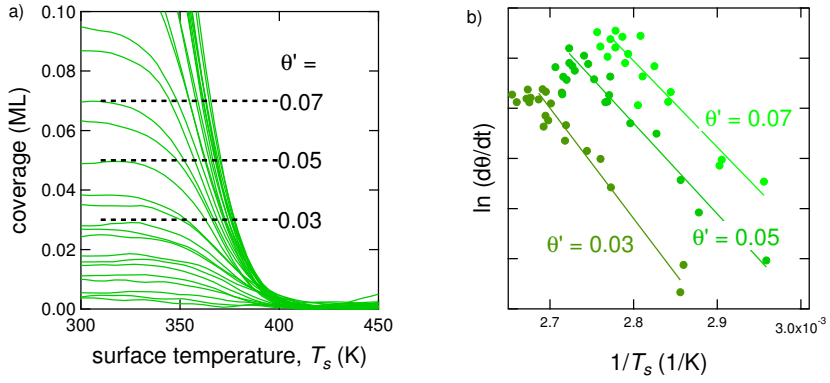

Figure 4.7: a) The remaining surface coverage during TPD versus time with three indicated remaining coverage for Cu(211). b) Exemplary Arrhenius plot for coverages indicated in panel a).

Figure 4.8 summarizes the obtained desorption energies and pref-

actors for Cu(111) (black circles) and Cu(211) (green squares) over the coverage range from 0 to $\sim$ 0.2 ML. The dashes lines in figure 4.8b) represents the average desorption energy and prefactors over this coverage range. They are $E_{des}^{111} = 74.4 \pm 1.3$ kJ/mol, ln $\nu^{111} = 25.9 \pm 0.4$ s^{-1}, $E_{des}^{211} = 72.0 \pm 1.1$ kJ/mol, and ln $\nu^{211} = 24.5 \pm 0.4$ s^{-1}.

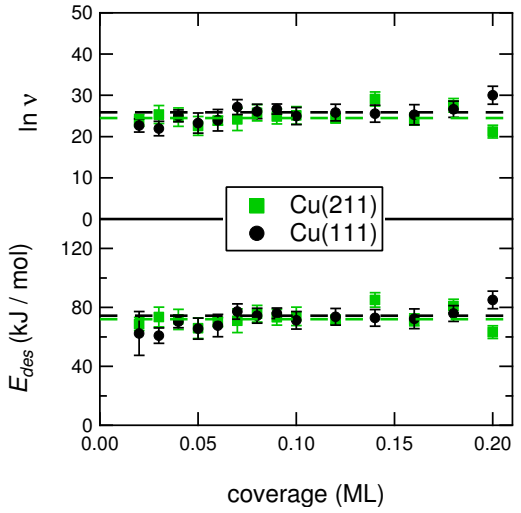

Figure 4.8: a) Prefactor and b) desorption energy obtained by complete analysis of TPD spectra for Cu(111) (black circles) and Cu(211) (green squares). Averages are indicated by dashed lines.

4.3.3 Determination of S_0 from TPD spectra

The integrated TPD spectra in figure 4.5 allow us to extract initial sticking probabilities that are considerably smaller than our KW limit. Figure 4.9 shows the results for Cu(211). We plot D_2 TPD integrals against a relative measure of the exposure for various expansion conditions. The relative measure of exposure is obtained by integrating the pressure increase in the chamber during the exposure to the pure beams. The slopes at the origin of the uptake traces in figure 4.5 are a relative measure of S_0 for each expansion condition. We use as an absolute reference the independently determined values of S_0 by the KW method for the higher temperature expansions. We use all of our values for S_0 obtained by the KW method to establish the best linear relationship with the slopes from figure 4.9. We then extrapolate to obtain values of S_0 for the lower incident energies, where we can not

obtain a signal using the KW method. Those values are indicated by open symbols in figure 4.4.

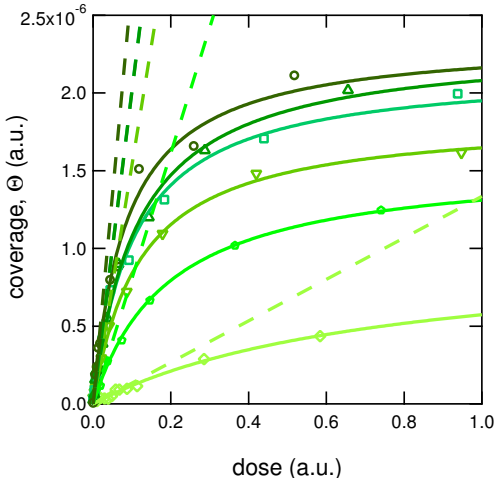

Figure 4.9: Coverage determined from integrating D_2 desorption from Cu(211) as a function of dose for molecular beams expanded at different nozzle temperatures. Increasing nozzle temperature and kinetic energy is symbolized by an increasingly darker shade of green. The solid lines are fits using a Langmuir adsorption model as described in the text. Dashed lines are the tangents at the origin for each fit and represent relative values of S_0.

4.3.4 Beam energy-dependent maximum coverage

The data in figure 4.9 suggest that for different expansion conditions, hence different most probable kinetic energies and kinetic energy distributions of our beams, the maximum attainable coverage, Θ_{max}, varies. This value is represented by the asymptotes of the individual curves. Increasing the beam's most probable energy leads to a higher asymptote. This type of behavior has been reported before for molecules experiencing a high barrier to dissociation, e.g. CH_4 on Pt(111)[80].

We fit our data in figure 4.9 using a simple Langmuir uptake model. The model assumes that there is no precursor state to dissociation. The molecule either dissociates upon impact or scatters back into the gas phase. Furthermore, desorption characteristics from our TPD spectra in figure 4.8 suggest that lateral interactions between adsorbed hydrogen atoms are weak, at least over the range 0 - 0.2 ML, for both Cu(111) and Cu(211). Therefore, we assume that the dissociation probability is not modified by lateral interactions. We integrate

$$\frac{d\Theta}{dt} = 2 \cdot S_0 \cdot \phi \cdot (1 - \frac{\Theta}{\Theta_{max}})^2 \tag{4.1}$$

with ϕ being the molecular beam flux at the crystal position and Θ_{max} the energy-dependent maximum coverage, to obtain

$$\Theta = \Theta_{max} \frac{S_0 \cdot (\phi \cdot t)}{S_0 \cdot (\phi \cdot t) + (\Theta_{max}/2)} \tag{4.2}$$

The fitting parameters are S_0 and Θ_{max}, while the dose equals the multiplication of the molecular beam flux ϕ, represented by the pressure rise in the UHV chamber, and time, t. The best fits to the data on the D_2 + Cu(211) system are shown as solid lines in figure 4.9.

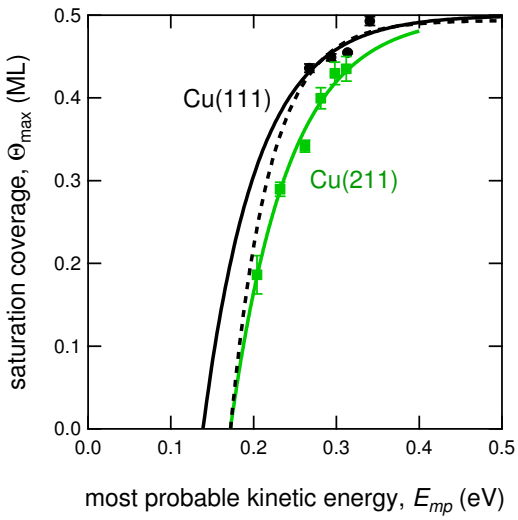

Figure 4.10: D_{ads} saturation coverage versus the most probable kinetic energy of the SMB used to dissociate D_2 on Cu(111) (black) and Cu(211) (green). The solid line through the data for Cu(211) is the best fit using the exponential functional form described in the text. The same best fit applied to the Cu(111) data only allowing an offset is shown as a solid black line. The dotted black line represents the best fit to Cu(111) data with the intercept at the energy axis fixed at identical value for Cu(211).

Figure 4.10 shows the dependence of Θ_{max} on the most probable kinetic energy of our molecular beams. The data are presented as symbols, i.e. black circles for Cu(111) and green squares for Cu(211). Error bars mark the uncertainty from the fits used to obtain the data. We have assumed that $\Theta_{max}^{(211)}$ and $\Theta_{max}^{(111)}$ for dissociating molecular hydrogen are both limited to 0.5 ML. Previous studies for Cu(111), Cu(110)

and Cu(100) all showed a 0.5 ML saturation coverage using atomic hydrogen sources[49, 81, 82]. As our surfaces are constructed from (111) facets with (100) steps, we consider our assumption of an absolute maximum coverage of 0.5 ML for Cu(211) to be reasonable. It allows us to use an absolute scale for Θ_{max} in figure 4.10. The data clearly show that higher maximum coverages are achieved for the atomically flat Cu(111) surface than for the highly stepped Cu(211) surface at any of the most probable incidence energies used in our molecular beam measurements.

As the data in figure 4.10 was obtained by fitting the maximum deuterium uptake using long exposures of the Cu surfaces to SMBs, the general trends may be interpreted to reflect how the minimum activation barrier to dissociation shifts upward with coverage. Unfortunately, the energy axis reflects the energy requirement in a rather indirect manner as our molecular beams have broad energy distributions. As the high energy tails of these distributions are likely responsible for the ultimately obtained coverage, we fit the data for Cu(211) in figure 4.10 using

$$\Theta_{max} = 0.5 \cdot (1 - e^{-(E_{kin} - E_{kin,0})/\beta}) \tag{4.3}$$

where $E_{kin,0}$ is the highest most probable kinetic energy that leads to no measurable dissociation. The value of β is a convoluted measure of how the minimum activation energy barrier shifts upward with D_{ads} coverage. A higher value of β represents weaker adsorbate-adsorbate interactions and a more constant activation barrier. In the absence of lateral interactions and a complete independence of the activation barrier on coverage, the data would be represented by a step function.

For Cu(211), the fit to the data is shown as a solid green line in figure 4.10. It intersects the energy axis at 0.172 eV. Allowing only a variation in $E_{kin,0}$, the same best fit to the Cu(111) data is shown as a solid black line. It is shifted by 34 meV. When fixing the cut off on the energy axis at the identical value for Cu(211), we obtain the dashed black fit for Cu(111). These two fits to the Cu(111) data represent two extremes. In the latter case, the minimum activation barrier to dissociative adsorption on the pristine surface is assumed to be the same for both surface structures. The coverage dependence of the minimum dissociation barrier is allowed to vary between the surfaces. In the former, the minimum activation barrier is taken to have the same dependence on coverage for both surfaces, but it is shifted to

Table 4.1: Classical activation barrier energies to dissociative adsorption reported in eV as calculated with the SRP48 functional for H_2 (D_2) on Cu surfaces and supercells presented in figure 4.1 at coverages of 0, 1/9, and 2/9 ML. Single values computed for 1/9 and 2/9 ML coverages are averaged values over all considered topologies of the H_{ads} overlayer. The actual energy range of the reaction barriers due to the different adsorbate overlayer structures is presented in brackets

surface	site	0 ML	1/9 ML	2/9 ML
Cu(111)	b_2	0.619	0.627 (0.603-0.642)	0.651 (0.623-0.677)
	t_2b	0.641	0.652 (0.627-0.701)	0.685 (0.609-0.815)
Cu(211)	b_2	0.640	0.662 (0.630-0.688)	0.684 (0.656-0.718)
	t_2	0.699	0.694 (0.680-0.731)	0.687 (0.657-0.722)

start at a lower value for Cu(111).

4.3.5 Coverage-dependent dissociation barrier from theoretical calculations

The results from our DFT calculations of reaction barriers are summarized in table 4.1 in eV. It lists the minimum reaction barrier energies calculated for the dissociation sites also shown in figure 4.1 for the (3×3) unit cell of Cu(111) and (3×1) unit cell of Cu(211) for the pristine surface (0 ML). The values for Cu(111) and Cu(211) are consistently $\sim$ 20 meV lower than those obtained for identical geometries on smaller unit cells as presented in our previous study[70]. This finding is in agreement with previous DFT calculations on the dependence of the reaction barrier height of H_2 on Cu(111) on the coverage that yielded generally lower barriers for smaller coverages (larger supercells)[83]. Specifically for the change of the supercell size from (2×2) to (3×3), the computed reaction barrier was reduced by up to 25 meV, depending on the computational setup used. Also listed in table 4.1 are single barrier energies for pre-covered surfaces at 1/9 and 2/9 ML obtained as average over all considered H_{ads} overlayer structures and the corresponding range of barrier energies according to the different topologies of the different adsorbate overlayers we have taken into account in the computations. For simplicity, we represent the average barrier energies as standard average values. They therefore do not capture potential effects arising from finite temperatures as, for example, thermodynam-

ical mean energy values would do. We also neglected coverage situations that would lead to adsorbed atoms in neighboring HCP and FCC sites, and, therefore, strongly repulsive interactions. According to figure 4.1a), transient H_2 dissociating at the edge of cell 1 and 7, respectively, would experience considerable interactions with H_{ads} positioned at the HCP sites in cell 7 and 8, and the FCC sites at cell 1 and 3 due to the employed periodic boundary conditions. The activation barrier for this situation is 0.951 eV, i.e. much higher than all other situations not leading to neighboring adsorbed H atoms. The latter generally show minimum energy barriers in the range 0.6 - 0.7 eV. All situations leading to neighboring H atoms show barriers near 1 eV.

The table shows several noteworthy features. First, the averaged minimum activation barriers generally rise very modestly with coverage for all dissociation geometries on Cu(111) and Cu(211), except for Cu(211)'s t_2 site. There the activation barrier energy drops with coverage. Second, the lowest values found for dissociation for particular geometries, i.e. the low end of the indicated ranges, may not even show any significant rise in the minimum reaction barrier. The observation of lower barriers at 1/9 and 2/9 ML appears at present loosely connected with the specific coverage configurations, that is, steric hindrance effects as discussed in refs. [84, 85] seem to be less important for the variation of the reaction barriers than resulting changes in the electronic structure. Third, only Cu(211)'s t_2b site shows a significant dependence on the exact adsorption sites of the 2 H_{ads} atoms with 0.2 eV in between the most and least favorable geometries. All other ranges show variation around 0.05 or 0.07 eV.

4.4 Discussion

We start our discussion with the comparison of dissociative sticking probabilities for Cu(111) as shown in figure 4.3. While our results compare well to those reported by Winkler and coworkers [49, 51], they far exceed those reported by Auerbach and coworkers for D_2[53] and H_2 [55]. Considering the excellent agreement between theoretically predicted sticking probabilities and the latter experimental data, as shown by Díaz et al.[34], an experimental difference must cause our sticking data to be higher. The origin of the discrepancy between Winkler's and Auerbach's data was pointed out by Díaz et al. When

convoluting the energy-resolved sticking probabilities produced by theory with the experimental energy distributions, results matched both experimental reports. Higher sticking probabilities found in the case of broader energy distributions result from poorer kinetic energy cooling in the supersonic expansion. Our sticking probabilities are nearly identical to those published by Berger et al. [51] for comparable conditions when we correct for the offset in the detection of our nozzle temperature (see table S6 in ref. [70]). As we have also previously determined nearly identical scaling between the kinetic energy and T_n (i.e. 2.53k) for our experimental apparatus as reported by Winkler (∼2.5k), and that this value is smaller than the one reported by Auerbach (∼2.65k), we conclude that the discrepancy with Auerbach's data is a result of poorer cooling in our molecular beam expansion.

We also compare our TPD spectra for Cu(111) to those reported by Anger et al. [49] for the same surface. With a ramp rate of 3 K/s, they find a single desorption feature with peak desorption temperatures increasing from ∼ 320 to 360 K with decreasing initial coverage. Their spectra show clearly overlapping trailing edges. These peak values and the TPD shapes are thus very similar to ours as presented in figure 4.5. The determined desorption energies in the range of 0 to 0.20 ML are in both cases coverage-independent and quantitatively similar. Our value of 74.5 kJ/mol compares reasonably well to the desorption energy we extract from their publication, 87 kJ/mol, as determined by the same analysis method. Frequency factors in this coverage regime were reported only from a leading edge analysis of TPD spectra [86], and show larger scatter that our data reported in figure 4.8a). Quantitatively, they agree reasonable well, though. Taking the different units for coverage into account, they find $^{10}\log\nu \sim 11.8$ where we find 11.2 for Cu(111). From the comparison of adsorption and desorption, we conclude that our data for this surface are quantitatively consistent with previous experimental reports that used the same experimental techniques and conditions, and analysis of data.

Turning to our results for Cu(211), the most remarkable finding is that the sticking probability of D_2 is larger on Cu(111) than on Cu(211). It may be considered of relevance that dissociation on the (111) plane strongly depends on the impact angle between the molecular beam and the surface normal[49, 51]. The angular dependence of the sticking probability, S, relates to the desorption probability, D, and is described by the equation:

$$\frac{S(E,\theta)}{S(E,0^\circ)}cos\theta = \frac{D(E,\theta)}{D(E,0^\circ)} \approx cos^n\theta \tag{4.4}$$

where n for Cu(111) is approximately 6 in the energy regime that we have probed[49, 51]. The angle between the (111) facet and the surface normal of the (211) plane is 19.5°. If sticking only occurs on the (111) facets of the (211) surface, the local sticking probability would be ∼0.75 times the value found for Cu(111). Only when assuming that the step area is unreactive and occupies approximately one third of the surface area, the weighted average reactivity over the (211) unit cell validates our experimental ratio of ∼0.5 for S_0^{211} and S_0^{111}. Although this may appear to be an acceptable explanation, the assumed lack of reactivity of the Cu A-type step would be highly surprising, especially since steps are generally expected to increase reactivity through lowering activation barriers in the dissociation of diatomics[87]. Many supersonic molecular beam experiments for hydrogen dissociation on stepped surfaces of other transition metals have supported this view[26, 28–30, 88].

Our recent combined theoretical-experimental study [70] explains the counterintuitive result. It showed that activation barriers on various locations within the unit cell of Cu(211) for D_2 dissociation are $30-90$ meV higher than on Cu(111) surface. The difference is observed again in the new results presented for 0 ML coverage in table 4.1. On Cu(111), the b_2 bridge site has the lowest dissociation barrier of ∼0.62 eV. The similar b_2 bridge site on the short (111) terrace, positioned near the downward edge, and the t_2b sites are found to have the lowest barriers for Cu(211), i.e. ∼0.64 eV. The barrier at the bottom of the edge is found to have a barrier near 0.70 eV. Based on the similarity of the current new calculations for the (3×3) unit cell for Cu(111) and (3×1) unit cells for Cu(211) and the previously reported values, the previous conclusions regarding the differences in reactivity of these surfaces are expected to hold. Energy dependent values for S_0 were calculated and agreed rather well with experimental results when taking the broad energy distribution of experimental molecular beams into account. However, the computed reactivity overestimates the absolute experimental value slightly. That difference should be reduced by the lower barriers reported in table 4.1 while maintaining higher reactivity of Cu(111) compared to Cu(211). Our new data on sticking at low incidence energies shown in figure 4.4 and extracted from TPD measurements allows to compare experiment and theory on a wider energy

range. This may help to determining the role of quantum mechanical tunneling for reaction and to further validate the performance of the approximations used in the dynamics calculations on sticking.This includes the Born-Oppenheimer static surface approximation and the electronic structure theory to compute the H_2 + Cu(211) interaction potential.

Our experimental data for desorption adds information regarding the effect on the potential energy surface governing the H_2/Cu interaction when disrupting the (111) plane with an A-type step. The higher dissociation barrier for Cu(211) may result from weakened binding of H(D) atoms in the zero-coverage limit, as illustrated in figure 4.11. From linear scaling between the binding energy, E_b, and the activation energy to dissociative adsorption, E_{act}[87], the difference in the desorption barrier for Cu(111) and Cu(211), ΔE_{des}, should be similar to the difference in activation barriers for these two surfaces, ΔE_{act}. From figure 4.8b), this appears to be the case. We found averaged desorption barriers over the 0 to 0.2 ML range for Cu(211) and Cu(111) differing by 2.4 kJ/mol (25 meV).

Our previous trajectory calculations simulating beam conditions with an incidence energy of 34 kJ/mol showed that molecules dissociated over different barriers positioned across the unit cell. Only ∼50% of the reaction is mediated over the step edge area. In Ref. [70], we have predicted that reaction is likely also over other regions, namely at the b_2 site located on the (111) terrace and at the t_2 site located at the bottom of the step. This may also have consequences for the desorption process, as discussed in the following. The average value of the activation energies at zero-coverage for the three sites listed given in table 1 is 0.652 eV, taking into account that the t_2b and the b_2 sites appear twice and the t_2 site only once in the (211) unit cell. This leads to an increase of the average activation energy by approximately ΔE_{act} = 33 meV in comparison to transition state energy of the H_2 + Cu(111) system. This compares well to the ΔE_{des} ∼25 meV found from TPD fitting. It also compares well to the difference between cut off values in figure 4.9. The difference in the energy requirement at the zero-coverage limit to obtain dissociation was found to be 34 meV when assuming that the activation barrier distribution was simply shifted upward for Cu(211) compared to Cu(111). The latter assumption is supported by the findings in table 4.1 when comparing the difference between the averaged barrier heights for Cu(211) with Cu(111) for pre-

coverages of 1/9 and 2/9 ML. The difference remains on the order of 35-40 meV, supporting the lateral shift, and not the option provided by the dashed line in figure 4.9. This finding is again consistent with a (near) invariance of the desorption energy found in figure 4.8 over the same coverage regime. Although the effects on the activation barrier to dissociation and the binding energy by introducing the A-type step to the (111) plane are small compared to the dissociation barrier itself ($\sim 5\%$), our new experiments detect them with reasonably consistent absolute values. They are on the order of several tens of meV. These values are also in quite good agreement with the new calculations of the coverage dependent barrier heights to dissociation.

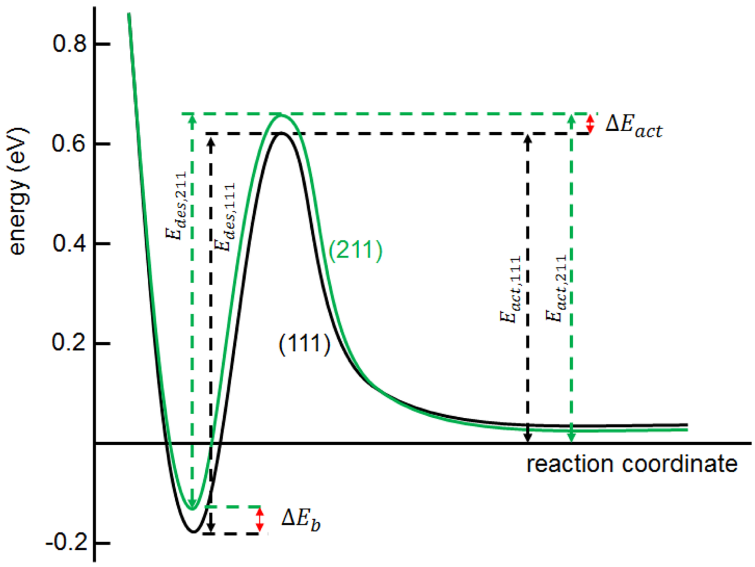

Figure 4.11: Schematic illustration of the dimensional PES for dissociation on Cu(111) (black) and Cu(211) (green) with indications of the activation barrier heights for dissociation, $E_{act,n11}$, and recombinative desorption, $E_{des,n11}$, as vertical dashed arrows, and the differences in binding energy, ΔE_b, and activation barrier to dissociation, ΔE_{act}.

We finally address whether the differences between Cu(211) and Cu(111) in adsorption and desorption can be linked to the shoulder at lower temperature observed for high coverages in the TPD spectra of figure 4.5 and modeled in figure 4.6. A small shoulder on the low temperature side of the main desorption feature has been reported before in the studies of H atoms incident on Cu(110)[49, 82] and H/D on Cu(111)[57]. In all cases, an atomic hydrogen beam was used to create

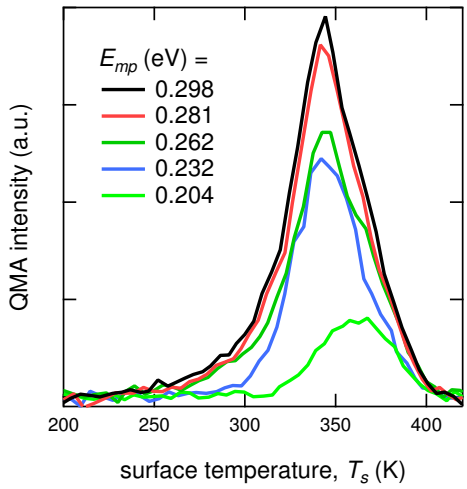

Figure 4.12: TPD curves for saturation coverages obtained using beams with increasing most probable kinetic energy.

some coverage of H_{ads}. The shoulder was consistently ascribed to desorption resulting from resurfacing of subsurface hydrogen. In the study by Rettner and Auerbach [57], this shoulder also did not saturate with increasing exposure and increased to an amount equivalent to 1.5 ML. The shoulder was in previous studies on low Miller index Cu surfaces never reported when using molecular hydrogen. We find it only in TPD spectra from the Cu(211) surface, excluding that it results from a small concentration of deuterium atoms in our highest temperature expansions beam. Had the highest nozzle temperatures led to presence of atomic H(D) in our beams, we should have observed the desorption feature also for Cu(111). As this is not the case, we conclude that it is a new feature associated with the occurrence of the A-type step of the Cu(211) plane. Its size compared to the main desorption feature is small, accounting for only $\sim 15\%$ of the total desorption yield. Oddly, it appears well before saturation of the main desorption feature. In figure 4.12 we have gathered TPD spectra obtained from D-saturated Cu(211) obtained at different nozzle temperatures. The shoulder peak clearly appears when the most probable incident kinetic energy of our beam equals 0.262 eV. However, at this energy, we are not yet close to the assumed limiting coverage of 0.5 ML. With higher incident energy, mostly the main desorption feature continues to increase. We interpret this to signal that a particular dissociation site on Cu(211) exists

- one not present on Cu(111) - and correlated to a significantly lowered desorption energy, as apparent from the Runge-Kutta fit ($E_{des} \sim$ 52 kJ/mol compared to 75.5 for the main feature). The site may be dynamically constrained - associative desorption occurs with limited lateral mobility. This may occur, for example, at sites at the bottom of step edges, e.g. the t_2 site, where diffusion barriers can be highly anisotropic. Dissociation at this site is also consistently found to have a higher barrier than the t_2b and b_2 sites on Cu(211). We note, though, that previous combined theoretical-experimental studies have shown that great care must be taken in relating hydrogen adsorption and desorption sites to desorption peaks in TPD spectra of complex surfaces. [89]

4.5 Conclusion

From our new study of hydrogen adsorption and desorption we find consistent trends regarding the effect of introducing A-type steps to the (111) plane of Cu. Whereas the lowered coordination of step atoms usually leads to lowering of dissociation barriers by increasing the binding energy, we find the opposite behavior here. A-type steps cause a - so far unique - upward shift in the distribution of activation barriers to adsorption and a downward shift in barriers to desorption. The effect is small in comparison to the absolute barrier heights, on the order of 5%, but it is clearly detectable. Furthermore, the barrier distributions are weakly dependent on hydrogen pre-coverage and saturation coverages are shown to depend on incident energy. Lateral interactions between adsorbed hydrogen atoms must be weak, especially in the lower coverage regime. Although the latter may be expected, the lowering of reactivity toward dissociation of a diatomic by introducing monoatomic steps surely is not.

During final stages of the preparation of this manuscript, results of a new state-resolved experimental study on molecular hydrogen desorption following atomic permeation through Cu single crystals appeared [90]. From application of the principle of detailed balance to their results, the authors come to the same conclusion regarding the reactivity of the clean Cu(111) and Cu(211) surfaces for three molecular hydrogen isotopologues. The stepped surface shows higher activation barriers and a broader distribution than the Cu(111) surface. At first

glance, the difference in activation barriers for direct activated adsorption onto the clean surfaces seems to agree quantitatively reasonably well with the barriers extracted here in our manuscript from TPD measurements. Averaged over the first J states, they report a shift in barrier distribution of several tens of meV for D_2. A second mechanism to adsorption, extracted from their desorption data, which shows a characteristic negative dependence on incident energy, lies outside the energy regime probed in our adsorption measurements. The results of this new study are encouraging to us. This independent work is based on a different experimental technique and definitively confirms our earlier and present conclusion of Cu(211) being less reactive then Cu(111) for hydrogen dissociation.

Chapter 5

Structure dependence of HD formation on curved Pt(111) surface

5.1 Introduction

For decades, flat single crystals have served as work horse models in fundamental studies of heterogeneous catalysis [91]. Originally, low Miller-index surfaces, e.g. the (111) and (100) surfaces for metals with a face-centered cubic (fcc) unit cell, caught most attention. Vicinal surfaces, e.g. the fcc (221), (533), and (997) surfaces, soon followed as these contain lower coordinated atoms in monoatomic step edges. Such steps mimic the edges on actual catalyst particles. To study the effect of a lowered coordination number of surface atoms to catalytic activity, simple model reactions, e.g. dissociation of molecular H_2 and D_2, and HD formation from these isotopologues were employed [92–99].

Being the simplest overall heterogeneously catalyzed chemical reaction based on more than a single elementary reaction, a kinetic model for HD formation contains the following elementary reactions

$$H_2(g) \rightarrow 2H_{ads} \tag{5.1}$$

$$D_2(g) \rightarrow 2D_{ads} \tag{5.2}$$

$$H_{ads} + D_{ads} \rightarrow HD(g) \tag{5.3}$$

Dissociative adsorption of H_2 and D_2 is followed by recombinative desorption of HD. If there is no isotopic effect to dissociative adsorption and recombinative desorption, the entire mechanisms reduces to

$$A_2(g) \rightleftharpoons 2A_{ads} \tag{5.4}$$

as H and D may both be represented by A. However, as the reactants and products have different molecular masses, mass spectrometry can be used to measure the extent of HD formation, i.e. the extent to which equilibrium is reached. At equilibrium, the ratios of partial pressure, $p_{H_2} : p_{D_2} : p_{HD}$, should be 1:1:2, as formation of HD competes with recombinative formation of H_2 and D_2. Below, we review studies that focused on elementary steps and the overall mechanism for Pt(111)-type surfaces.

The elementary dissociative adsorption of hydrogen, i.e. equations (5.1) and (5.2), was originally studied in greatest detail using supersonic molecular beam techniques for Pt(111) by Luntz et al.[22]. They found evidence of energetic corrugation, i.e. a distribution of barriers to dissociation, with no threshold. Reactivity, as quantified by the incident energy dependence of the initial dissociation probability, $S_0(E_{kin})$, increased smoothly from the lowest attainable incident energy up to 0.55 eV for normal incidence. A study of the polar angle dependence to dissociation showed that normal energy scaling (NES) does not hold, although exchanging normal for parallel momentum reduces reactivity. They reported an absence of isotope effects and an independence of both surface temperature and nozzle temperature, concluding that dissociation is direct and proceeds over a range of barriers. Samson et al.[21] verified the energetic corrugation, finding absolute reactivities that agree with Luntz's data. Recently, we studied this system's polar and azimuthal dependence for D_2 dissociation, as discussed in Chapter 3. Our data also showed nearly perfect quantitative agreement with Luntz's polar angle dependences and absolute dissociation probabilities for a range of incident energies. In agreement with the most recent dynamical calculations for this system[39], we concluded that the system shows, at most, very little geometric corrugation.

Using flash desorption, Lu and Rye already showed in the 1970's that the dissociation probability of molecular hydrogen for four Pt surfaces decreased in the order: (110) > (211) > (100) > (111)[92]. Besides ordering the reactivity of low Miller index surfaces, it clearly showed that corrugation in the form of monoatomic steps aids the

dissociation process. The (211) surface combines a 3-atom wide (111) terrace with A-type steps, i.e. steps made of a monoatomic (100) facet. In Somorjai's notation, this is Pt[3(111)×(100)]. In a similar study, Christmann and Ertl showed two years later that the presence of B-type steps also increased the initial dissociation probability[99]. The (997) surface, consisting of 8-atom wide (111) terraces separated by monoatomic (110) facets, or Pt[8(111)×(110)], was a factor of four more reactive than Pt(111) in dissociating molecular hydrogen. Both studies used dissociation from a bulb gas to create a surface coverage of H_{ads}, Θ_H, at a low surface temperature, T_s. A temperature ramp was started to quantify with temperature programmed desorption (TPD) how much H_2 had dissociated after a particular exposure. Hence, their measure of reactivity toward dissociation averages over a wide range of incident kinetic energies and angles with respect to the surface normal for molecular hydrogen.

Many years later, Gee et al. studied the role of monoatomic A-type steps in the dynamics of hydrogen dissociation using the Pt(533) or Pt[4(111)×(100)] surface and supersonic molecular beam techniques[26]. Whereas S_0 increased similar to Pt(111) at higher incident energies for this surface, it dramatically decreased with increasing kinetic energy up to $\sim$ 150 meV. Their suggestion that step sites allow for new dynamical mechanisms to dissociation was corroborated by dynamical calculations performed in the group of Baerends on the first detailed potential constructed for H_2 and Pt(211)[31, 32]. Using a series of Pt single crystals that contain A-type steps with (111) terraces of various widths, Groot et al. separated the reactivity for molecules impinging onto the A-type step and the (111) terraces [28–30]. They refined a simple mathematical model from Baerends and coworkers and accurately predicted the reactivity of hydrogen dissociation for all Pt[n(111) × (100)] type surfaces based on measurements for Pt(211) alone. The model relies on separation of the dissociation probability into three dynamical components, two of which only occur at the monoatomic steps. As there is no dependence on a molecularly-bound intermediate state that may diffuse from site of impact to some other more reactive site, S_0 scales linearly with step density. We recently showed that the only other model for molecular hydrogen dissociation on Pt(111), i.e. a model relying predominantly on an indirect process to dissociation at step and kink defects via diffusion of a physisorbed molecular intermediate[20, 100], does not correctly predict reactivity

over a large range of step densities [101]. Reactivity also does not follow the expected surface temperature dependence for this model.

For the overall mechanism of HD formation, the isotopically-independent direct dissociation of molecular hydrogen at steps and terrraces sites is followed by recombination of adsorbed atoms and their immediate desorption, i.e. reaction (5.3). Greenlief et al. studied H-D exchange on Pt(111) using temperature programmed desorption (TPD)[102]. They found no isotope effect in desorption after dosing the isotopically pure molecules at a surface temperature, T_s, above 250 K. They reported an activation energy for recombinative desorption of 6.7 ± 0.4 kJ mol^{-1}. Verheij et al. also conducted experiments on Pt(111) investigating HD formation from an H_2 molecular beam with D_2 dissociation from a bulb gas[103]. By detecting HD in an angular resolved fashion and measuring its kinetic energy, they reached the conclusion that two parallel mechanisms for adsorption and desorption were causing HD formation. For stepped surfaces, Somorjai et al. had already studied HD formation using both effusive and supersonic molecular beam techniques in combination with background dosing [93–98]. Originally, the H-D exchange reaction was only detectable on high Miller index Pt single crystal surfaces with B-type steps. Later, they also found it to occur on Pt(111) and concluded that doubling the step density doubles the reaction probability at higher temperatures [95]. Christmann and Ertl showed in their TPD-based study that the presence of B-type steps enhances the activity in H-D exchange between H_2 and D_2 by an order of magnitude for Pt(997) compared to Pt(111)[99].

In this chapter, we introduce the use of a small curved Pt single crystal with its apex oriented to expose the (111) surface and its macroscopic curvature ideally resulting from monoatomic A-type and B-type steps. Such a small curved crystal surface was studied recently by Walter et al. probing both the clean surface and the effect of surface strain on adsorbed CO [104]. We used the combination of supersonic molecular beams and a large Ni cylindrical crystal before to study elementary dissociation[88]. Very recently, we did the same using a small curved Pt single crystal[101]. Here, we show that such a small single crystal also serves to study overall reaction mechanisms through the H-D exchange between H_2 and D_2. However, such crystals must be treated carefully to obtain the ideal structure, consisting of atomically flat terraces and monoatomic steps. Curved single crystal surfaces may locally contain surface structures that are unstable under particular cleaning

or annealing conditions, as shown, for example, by Ilyn et al. for a Ni curved single crystal[105]. Especially since surface reconstruction have been found and studied for flat Pt single crystals exposing the (111) terraces surface, e.g. for Pt(997)[106–108], and such reconstructions may be related to exposure to O_2 and high-temperature annealing, a detailed study of our curved Pt single crystal and cleaning procedures is necessary.

5.2 Experimental methods

All experiments are carried out with a home-build ultra high vacuum (UHV) apparatus 'LIONFISH' (base pressure is below 1×10^{-10} mbar). The UHV system is attached to a double differentially pumped supersonic molecular beam line and contains, a.o., a fixed quadrupole mass spectrometer (QMS, Pfeiffer QMA 200), a quadrupole mass spectrometer (UTI, 100C) that can be moved along the molecular beam axis with an x, y, z manipulator, and LEED/AES optics (OCI BDL800IR-MCP).

The crystal is mounted at the bottom of a vertical liquid nitrogen cooled cryostat, which protrudes into the UHV chamber through an x, y, z, θ manipulator. The crystal temperature is controlled between 89 and 1300 K using liquid nitrogen cooling and radiative heating or electron bombardment from a tungsten filament located being the crystal. The crystal is cut and polished to expose a curvature encompassing ~ 31 ° along the $[11\bar{2}]$ direction with the (111) surface at the apex. Figure 5.1a shows our laboratory coordinates for the crystal. The z axis runs along the vertical direction and the x axis runs along the horizontal direction. The supersonic molecular beam and the electron beam of the LEED/AES optics are incident along the y axis. As figure 5.1b shows, the upper part of the crystal consists of (111) terraces with B-type steps. The lower part of the crystal contains A-type steps. By moving the crystal along the z axis, we can change the surface exposed to our molecular beam and LEED/ AES optics from beyond Pt(553) (z=+3.19 mm, α=+12.3 °) to Pt(533) (z=-3.74 mm, α=-14.4°) smoothly. Here, α is the angle between the surface normal at the indicated z position and [111].

The crystal is cleaned by sputtering at 0.5 keV with $\sim 2.0\mu A$ Ar^+ current ($p_{Ar} = 6.0 \times 10^{-6}$ mbar) for 5 minutes at surface temperature

900 K. This is followed by an oxidation at the same surface temperature (3 minutes, $p_{O_2} = 3.5 \times 10^{-8}$ mbar) and annealing at 1200 K for 3 minutes. This cleaning procedure is repeated 3-5 times before the last clean cycle. For the last cycle, we only sputter and anneal. Two different annealing temperature are used, 850 K and 1200 K, respectively.

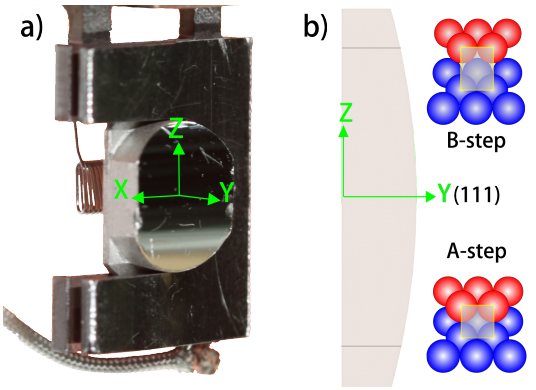

Figure 5.1: Schematic of the crystal. The crystal is mounted onto the 'U' shape sample holder. The x and z axes are along horizontal and vertical direction, respectively. The molecular beam and LEED/AES optics are incident along the y axis. Figure b) is a schematic view along the x axis. The upper part of the crystal contains B-type steps and the lower part of the crystal contains A-type steps.

The molecular beam is generated by expansion of a gas mixture at a total pressure of $\sim$ 2.0 bar through a tungsten nozzle with a 28 μm diameter orifice. The beam is shaped by two skimmers (subsequent diameters from the expansion nozzle are 0.45 mm and 2.5 mm). Two flags, one positioned in the second differential pumping chamber and one in the UHV chamber, and a chopper wheel located in the first differential chamber, modulate the beam. The two flags are used to determine the absolute dissociation probability using the King and Wells (KW) technique[10]. The chopper wheel is a fast rotating disk ($\sim$250 Hz) with two broad (17 mm) and two narrow (0.85 mm) slits. It is used to determine the kinetic energy and the energy distribution using time-of-flight (TOF) techniques.

A home-made gate valve separates the second differential pumping chamber and the UHV chamber. It consists of a rectangular plate with four orifices. It slides through a groove cut into a solid flange with knife edges on both sides. A linear feedthrough accurately positions the sliding plate within the groove. The sliding plate contains, besides an O-ring to seal the UHV chamber, one larger hole with a diameter

of 6.2 mm, one medium-sized hole with diameter of 3.2 mm, one small hole with diameter of 1.6 mm, and a rectangular slit of 3.2 mm in horizontal direction and 0.065 mm in vertical direction. By choosing different orifices on the plate, we can change the molecular beam's size and shape at the crystal position inside the UHV chamber.

For HD formation experiments, we use a mixture of H_2 (6N, Linde Gas, Rotterdam, The Netherlands), D_2 (2N8 isotopic purity, Linde Gas, Rotterdam, The Netherlands) and Ar (5N7, Air Products) to generate the supersonic beam. The beam is expanded at room temperature. The most probable energies of H_2 and D_2 are 10.9 meV and 22.7 meV, respectively, as determined by TOF techniques. The surface temperature of the crystal is 530 K. At this temperature, H_2, D_2, and HD desorb instantaneously. HD formation is measured using the King and Wells (KW) technique. However, while the reactant intensity drops when the beam is allowed to impinge upon the surface, the HD partial pressure detected by our QMA increases when the $H_2/D_2/Ar$ beam hits the surface. Figure 5.2 shows a series of measurement of HD formation when moving the crystal along the z axis. In this example, we probe reactivity change across the curved surface at 15 locations, each separated by 0.5 mm. In between moving the crystal from one to the next location, the beam is blocked by moving both beam flags sequentially. The simultaneously detected H_2 and D_2 signals are also shown. The signals clearly show the opening and closing of both flags. When we open the first flag in the second differential pumping chamber, the beam enters into the UHV chamber. The H_2 and D_2 signals clearly increase. The HD signal also increases, even though the beam does not impinge directly onto the crystal. This increase is due to HD contamination in the molecular beam, presumably from H-D exchange in the nozzle, and/or from the effusive load onto H-D reactive surfaces in our chamber (e.g. the hot tungsten filament behind the Pt sample and the Pt sample itself). When we open the second flag located in the UHV chamber, the beam impinges directly onto a narrow part of the Pt crystal. The H_2 and D_2 signals drop but the HD signal increases further. When we close the second flag but keep the first flag open, the H_2 and D_2 signals increase and the HD signal drops to its earlier level. When both flags are closed, all the signals drop to their residual values. All three signals change simultaneously. The green vertical line with arrow heads in figure 5.2 indicates how we quantify in a relative sense the HD formation by each separate part of the crystal when the

beam directly impinges onto it. We use the QMA intensity difference observed when opening and closing the second flag. Compared to H_2 and D_2, the HD signal has a high signal-to-noise ratio, especially when the reactivity is low. The lower background signal for HD allows an increased channeltron voltage for HD detection in comparison to H_2 and D_2, increasing our sensitivity to the surface reactivity as compared to detection of the removal of H_2 and D_2. Those signals are more noisy than the HD signal. In figure 5.2, the HD signal also clearly shows reactivity changes for different z positions. There is clearly HD being produced at the (111) apex (8th exposure), but HD production increases rapidly when moving onto either type of stepped surfaces.

A slightly complicating factor appears when scrutinizing the data in figure 5.2. The absolute QMS intensities for H_2 and D_2 seem to change each time we admit the beam to the chamber. The rise resulting from admitting the molecular beam to the UHV chamber increases only a little each time, but over the entire experiment quite substantially. This increase is not caused by an instability in our molecular beam. All pressure gauges in the differential stages and UHV chamber indicate that the beam is stable. The origin of the increasing QMS intensity for H_2 and D_2 lies in reduction of the channeltron's inner surface when using a reducing gas. It increases the channeltron's sensitivity, presumably by lowering the work function of the glass through reduction of its outermost layer. We have noticed this effect also in experiments performed with the same type of QMS on a different molecular beam-UHV apparatus (see Chapter 4) and the opposite in experiments using O_2 molecular beams and the same Baltzers QMA200 in the molecular beam apparatus used for the current study[109].

Normalizing the rise of H_2 and D_2 to the first admission of the beam to the UHV chamber, we obtain a functional form of the sensitivity change. It is shown in figure 5.3 for H_2 and D_2 as a function of the number of times that the beam was admitted to the UHV chamber. Here, we show data for a similar experiment as shown in figure 5.2, however, the change in z position was reduced and the beam was admitted 41 times to cover the entire curved surface range. The first admission is numbered as "0" and used for normalization. As beam admission is computer-controlled and uses a fixed time for each admission, the x axis is proportional to the integrated flux of reducing gases admitted to the chamber. For both isotopologues we see the same sensitivity change throughout the entire experiment. It is nearly

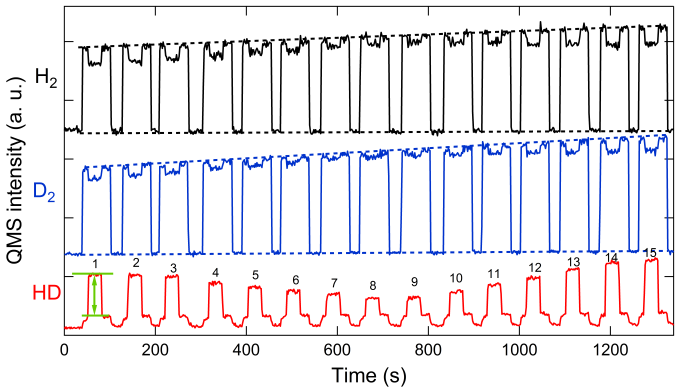

Figure 5.2: An example of a continuous measurement of HD formation by moving the crystal along z axis with a 0.5 mm step. The H_2 and D_2 signals are also showed simultaneously. The green lines indicate how we determine HD formation.

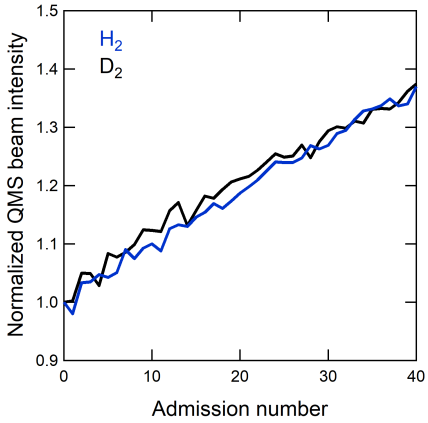

Figure 5.3: Normalized QMS signal intensities of H_2 (blue) and D_2 (black) versus number of times that the beam is admitted to the UHV chamber.

linear. Assuming that the sensitivity to HD follows the manner trend, we correct the HD pressure rise for impingement onto each separate part of the curved surface for this QMS sensitivity change in each run of measurements across the crystal. Obviously, for experiments that take longer as smaller steps in z position are used, the effect is larger.

5.3 Results

5.3.1 The molecular beam size at the surface

As the HD formation is sensitive to step density and step density varies vertically along the crystal's surface, using a circular or rectangular shaped beam influences the measured HD production. To measure the exact size of our beam, we move the crystal horizontally across the beam and measure the intensity of HD (m/e=3) using the QMA200 mass spectrometer. Figure 5.4a shows the results of these measurements when the beam is shaped using the 1.6 mm diameter circular orifice in the sliding beam valve. The blue circles are the HD intensity at different x positions. HD production is nearly identical at -2.0 mm and +2.0 mm. Beyond these positions, it drops (nearly) linearly with position. From the known width of the crystal, ie. 7.0 mm, and the 4.0 mm wide plateau we calculate the beam size at the crystal position. It is ϕ 3.0 mm. The solid line in figure 5.4a is a simulation of the overlapping area of a ϕ 3.0 mm circle moving along the x axis on the 7.0 mm wide crystal surface. The simulation agrees well with our measurement. Figure 5.4b shows the result of the same experiment using the 3.2×0.065 mm slit as our molecular beam shape-defining orifice. The red circles are the measured HD intensity from our QMA versus x position. As the inserted diagram shows, we now have a much more limited range to move the crystal to keeping the HD intensity identical. The solid red line in figure 5.4b is a simulation of the overlapping area of the 6.0 mm wide rectangle with the crystal along the x axis. The simulation again agrees very well with our measurement. The beam's size at the crystal changes by a factor of $\sim$1.9 when varying between these two shape-defining orifices. The vertical size of the beam at the crystal can thus be calculated independently for the 3.2×0.065 mm slit orifice. It is $\sim$0.12 mm. The red horizontal bar in the inserted picture of figure 5.4b shows the size of the beam in comparison to the crystal. As shown in the inset by the dashed rectangle, the rectangular beam's size limits the extent over which we can probe reactivity across the surface without more complex deconvolutions. The range of z positions is limited to $\pm$2.65 mm from the apex when using the slit orifice.

The points that are aberrant at the negative x side are caused by the 'U' shaped sample holder, shown in figure 5.1a. At the negative x

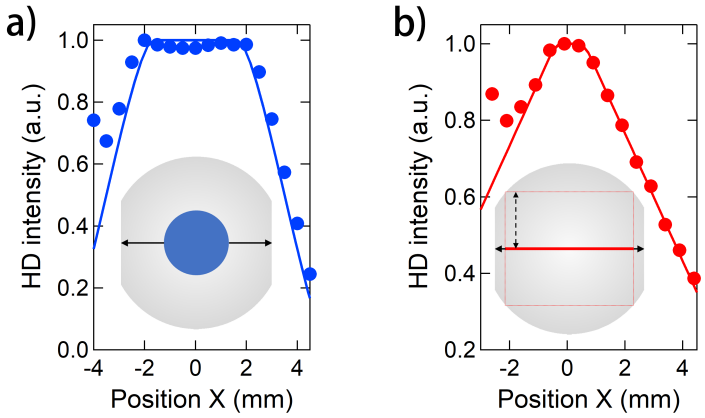

Figure 5.4: HD intensity variation with x-position in the laboratory frame as measured by the QMA200 upon exposure to a H_2/D_2/Ar beam for a) a 1.6 mm diameter circular orifice and b) a 3.2×0.065 mm wide rectangular orifice. Inserted schematics show the molecular beam size in comparison to the crystal. Blue and red circles in figures a) and b) show the measurements. The solid line in a) is a simulation of the convoluting beam and crystal areas for moving the crystal along the x axis assuming a 3.0 mm diameter beam. The solid line in figure b) shows the same simulation using a 6.0 mm wide rectangle. The red bar in the insert of b) shows the extracted 6.0× 0.12 mm molecular beam size at the crystal position in comparison to the crystal's surface. The dashed rectangle indicates the usable area for the 6.0 mm wide beam. The crystal can only be moved along z axis ±2.65 mm from the center when using the slit orifice without the beam impinging onto the crystal holder.

side, the beam impinges onto the sample holder, which is coated with a thin Pt foil. The polycrystalline foil is reactive and HD molecules are generated, causing the higher than expected HD intensity. At the positive x side, the sample holder is open. The part of the beam not impinging onto the same does not strike a reactive surface and does not contribute to the H-D exchange reaction.

5.3.2 HD formation along z axis

Figure 5.5a shows how the local angle between the surface normal and [111], α, (black circles) and the ideal monoatomic step density (red squares) change with the z position of our crystal. To reach $\alpha = -14.4°$, we require $z = -3.74$ mm at the A step side. This position responds to the Pt(533) surface, i.e. Pt[4(111)×(100)]. Moving to the opposite side, we find at 12.3°, i.e $z = +3.19$ mm at the B-type

step side, Pt(553), i.e. Pt[4(111)×(110)]. The step density changes linearly with the distance from the center of the crystal. The slopes of step density with z are identical for both sides of the center. However, reaching the same terrace width, e.g. $n = 4$ for the A and B-type steps, is not the same as the step is structured differently.

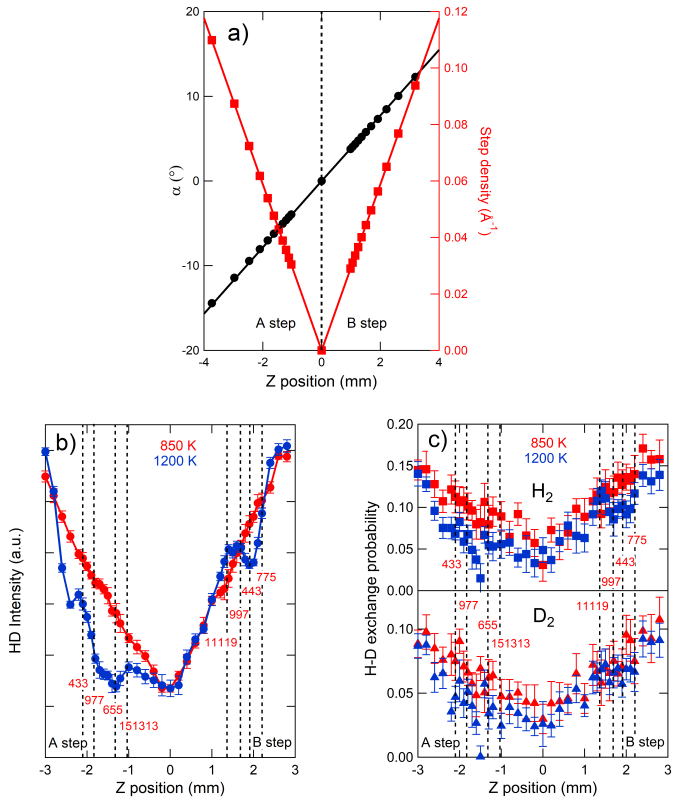

Figure 5.5: a) shows the angle α (black circles) and the step density (red squares) versus the z position on the crystal. b) shows HD formation after the crystal is cleaned using an identical procedure but annealed at different temperature as a final step. The crystal is moved along the z axis with x fixed at 0.0 mm. The data color-coded with red and blue represent the final anneal temperature of T_{anneal} =850 K and 1200 K, respectively. The dashed lines indicate non-reconstructed surface structures. c) shows in the upper panel the absolute H-D exchange probability for H_2 and in the lower panel for D_2 for the same final annealing steps as used in b). The definition of H-D exchange probability is provided in the text.

Figure 5.5b shows the HD formation from the impinging H_2/D_2/Ar beam shaped by our rectangular orifice when moving the crystal along the z axis. The x position is fixed at 0.0 mm. The data presented

with red markers are obtained after the crystal is annealed in the final cleaning cycle at T_{anneal} = 850 K. HD production is, to a first approximation, linear from the center of the crystal to both sides over the entire range. As the dissociation of H_2 and D_2 depends linearly on the availability of steps at these conditions [29, 101], it suggests that the step density of the crystal increases linearly from the center to both A and B step sides.

The data indicated with blue markers in figure 5.5b are obtained when the crystal is cleaned by the same cleaning procedure but finally annealed at T_{anneal} = 1200 K. HD formation is clearly not linear with position over the entire range on both sides. On the A-type step side, the HD intensity is lowered at all positions in comparison to data obtained after annealing at 850 K and only recovers to approximately the same value at −3.0 mm, i.e. where our beam partly impinges onto the crystal holder. The reactivity increases linearly from 0.0 mm to −1.0 mm with a reduced slope. Then it drops from −1.0 mm to −1.3 mm. It subsequently rises again with a slope that is steeper than observed in the data obtained for T_{anneal} = 850 K. A second dip in the nearly linear increase in overall reactivity occurs just beyond -2.0 mm.

On the B-type step side of the apex in figure 5.5b, the HD intensity initially increases linearly from 0.0 mm to +1.4 mm with an identical slope as found for the data obtained at T_{anneal} = 850 K. Then it sharply drops from +1.4 mm to +1.9 mm. Subsequently, it rises again with a steeper slope as found for the 850 K data. At the z position of +1.9 mm the HD intensity for T_{anneal}= 1200 K are approximately identical to the values obtained for T_{anneal} = 850 K. The dependence of local reactivity on the annealing temperature in the final cleaning cycle indicates surface structural differences induced by the final annealing step.

In figure 5.5c, upper panel, we report for the H_2 isotoplogue the absolute H-D exchange probability as a function of z position. This probability equals the drop in the H_2 QMS intensity when opening the second flag divided by the rise in H_2 QMS intensity when admitting the beam (i.e. opening the first flag). The latter is proportional to the number of H_2 molecules in the beam entering the chamber. The former is proportional to the number of H_2 molecules dissociating and not returning as H_2 to gas phase, but as HD. Clearly, for each H_2 molecule that dissociates and is involved in H-D exchange, two HD molecules are produced and detected at m/e = 3. We use the same color coding

as in 5.5b to indicate T_{anneal} as 850 K (red) and 1200 K (blue). The bottom panel shows the same information for D_2. Clearly, the general trends observed for HD production in figure 5.5b are reproduced. The chance for both H_2 and D_2 to dissociate and recombine with an atom of the other isotopic kind increases with step density. It also decreases for $T_{anneal} = 1200$ K on extensive parts of the A-type step side of the curved surface, in particular near Pt(655), although the position of largest dip differs by ~ 0.1 mm. On the B-type step side, the data show a dip in H-D exchange probability near Pt(443). Clearly, the signal-to-noise level is considerably worse in these panels than in figure 5.5b. It is noteworthy that the absolute H-D exchange probabilities are not identical for H_2 and D_2 at the same surface positions. They differ by approximately a factor of 1.5.

5.3.3 LEED analysis of the surface structure

To study local changes of the crystal surface by diffraction, we minimize the electron beam size of our LEED optics. A micro-channel plate (MCP) LEED should allow for the use of a smaller electron beam diameter than conventional LEED optics. Our electron beam diamater is estimated to be 0.3 mm, based on a measurement of current to the crystal from the electron beam when translating the crystal parallel to the face of the optics. However, the design of MCP-based LEED/AES optics distorts the observed LEED pattern. The MCP plate is flat while proper visualization of the Ewald sphere requires a hemispherical screen. We have previously discussed how the distorted pattern can be corrected [13] and have written a software program to modify photographic images taken of the LEED pattern and correct the distortion.

Figure 5.6a shows three examples of corrected photographic images of LEED patterns taken at z=-2.2 mm, z=0 mm and z=+2.2 mm. In this figure, vertical spot splitting is clearly observed for the two images not taken at the apex. The vertical splitting indicates that the steps lie in in the x-y plane in the laboratory frame. To analyze the dependence of spot-splitting in the LEED pattern on the z position of the crystal, we select a slice of the $(0, -1)$ LEED spot be cropping the image to 4×200 pixels. An example is shown in figure 5.6b. We subsequently connect a series of such slices for different z positions. Figure 5.6 c and d show the result. The crystal was moved along z axis with a

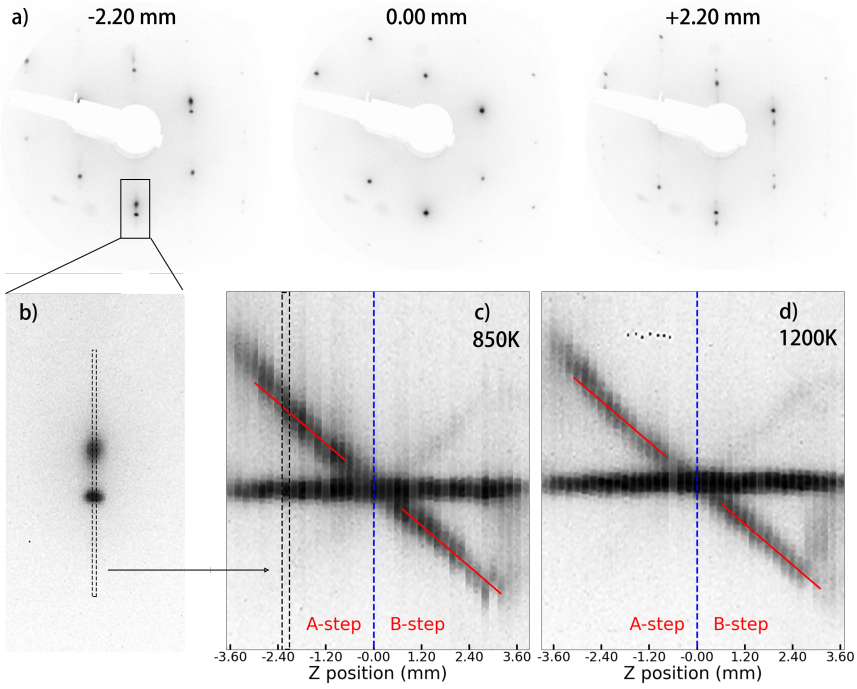

Figure 5.6: Figure a) shows the photographic images of LEED patterns taken at z=-2.2 mm, z=0 mm and z=+2.2 mm after the crystal is annealed at 850 K. Figure b) shows the expansion of the solid rectangle in figure a). The dash rectangle shows the slice we used to cut the center of $(0, -1)$ LEED split-spot (4×200 pixels). Figure c) and d) show a connected series of such slices at different z positions after the crystal is annealed at 850 K and 1200 K, respectively. The red lines are the theoretically predicted values of spot-splitting for different stepped surfaces[110].

0.2 mm step to obtain these images. Figure 5.6c visualizes the spot splitting versus z positions after annealing at 850 K. The spot splitting increases (roughly) linearly from the center to both A-type and B-type step sides. At the edge of the A-type step side, spot splitting diverges from the linear behavior observed closer to the apex. Spot-splitting increases there. The red lines drawn in the image represent the calculated spot-splitting for monoatomically stepped Pt(111) surfaces[110]. Our experimental data agree over a large extent very well with the calculated values, with only a minor deviation occurring beyond -2.5 mm, i.e. near the edge of the crystal. Figure 5.6d shows the same spot-splitting versus z position after annealing to 1200 K as well as the theoretical values. At first glance, differences between figures 5.6c and 5.6d seem small and spot-splitting after 1200 K again agrees well

with the theoretically predicted values for mono-atomic steps. However, differences appear when studying the images in more detail. For example, while in figures 5.6c and 5.6d, the horizontal branch created by connecting the slices of images shows a nearly fixed width (i.e. spot diameter) and intensity (i.e. shade of grey), the branches at $-45°$ (i.e. rotated clockwise) created by the second LEED spot is less intense for T_{anneal} = 1200 K, particularly at some z positions.

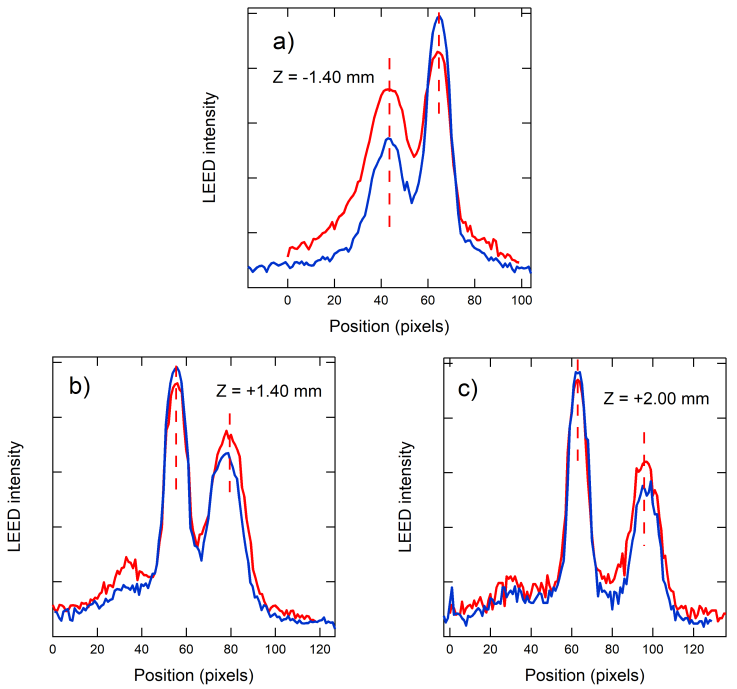

Figure 5.7: LEED intensity profiles of the split $(0, -1)$ spot at different z positions of the crystal. The red and blue curves indicate the two different annealing temperatures, i.e. 850 K and 1200 K, respectively. The red dashed lines indicate the peaks' positions of the red curves as comparison for the blue curves.

On the A-type step side, figure 5.5b shows a strongly reduced HD productivity at z=-1.32 mm for T_{anneal} = 1200 K (blue data). This position corresponds to the unreconstructed (655) or Pt[11(111)×(100)] surface. The HD productivity drops nearly to the level of the crystal's apex. Figure 5.7a shows the intensity of the (0 -1) split spots from the LEED patterns at z=-1.40 mm for annealing at both annealing temperatures (red for 850 K, blue for 1200 K). The peaks' positions are identical for both treatments, but the intensity ratio of the peaks has

clearly changed. The higher annealing temperature (blue line) yields a reduced intensity for the left peak (upper spots in figures 5.6c and 5.6d) and an increased intensity for the right peak (lower spot in figure 5.6d).

On the B-type step side, the HD productivity seems increased slightly by annealing at 1200 K instead of 850 K for $z = +1.36$ mm. This position corresponds to the (11 11 9) or [10(111)×(110)] surface. It is followed by reduced reactivity at $z = +1.91$ mm, i.e. nominally the (443) or [7(111)×(110)] surface. Figure 5.7b and c show the LEED intensity profiles for the (0 -1) spots at $z = +1.40$ mm and $z = +2.00$ mm, respectively. Here, the left peak corresponds to the spot causing the horizontal branch in figure 5.6c and 5.6d. For both z positions, the LEED intensity profiles do not differ much. Upon detailed inspection, in figure 5.7b, the peak on the right side shifts a little to the left after annealing to 1200 K (blue line) compared to the T_{anneal} =850 K case (red). For figure 5.7c, the opposite occurs.

5.4 Discussion

When annealed at 850 K, both HD formation in figure 5.5b and LEED spot splitting in figure 5.6c suggest a linear relation between step density and distance from the crystal's apex. This occurs at both sides of the apex. The experimentally determined LEED spot splitting is quantitatively in agreement with calculated values for monoatomic steps. Spot splitting is also mostly identical on both sides of the apex. The only clear difference between the A and B-type step sides of the crystal is a third diffraction spot weakly visible on the B-type step side. It causes the faint +45° branch in figure 5.6c and is also observed in the intensity plot in figures 5.7b and 5.7c as a small third diffraction feature equidistant to the center peak. Such triplets in LEED patterns may occur when the inherent LEED intensity variation from constructive interference caused by the terraces captures three 'rods' of interference caused by the step array[12]. It is surely not caused by step doubling or faceting as that would lead to a triplet with the third spot appearing in between the original two spots as, e.g., observed for restructuring of Pt(997) [106].

HD formation after T_{anneal} = 850 K is nearly identical on both sides of the crystal's apex. Figure 5.5b shows through a slightly steeper

slope on the B-type step side that HD formation increases more rapidly with step density than for A-type steps. This result may be expected as B-type steps also show higher initial dissociation probabilities than A-type steps in the incident energy regime where dissociation is dominated by steps [101]. Hence, the linear HD formation with position and the non-zero reactivity at the apex in figure 5.5b indicate that HD is being produced by (111) terraces with additional aid of steps, whose density increases linearly with the distance to the apex. The aid of the steps in increasing HD formation may be expected to lie predominantly in the dissociation of H_2 and D_2, and not so much in increasing desorption rates.

We noted that the absolute H-D exchange probabilities for H_2 and D_2 from figure 5.5c were not identical. A comparison of the absolute H-D exchange probabilities reported on the y axes in the upper and lower panels shows that the fraction of H_2 to return as HD is higher than for D_2 molecules. The ratio is approximately 1.5. We consider the reaction kinetics to trace its origin. First, we define the rates of elementary steps. The dissociation rates, R, for H_2 and D_2 are defined by their incident fluxes, Φ_{H_2} and Φ_{D_2}, and dissociation probabilities, S_{H_2} and S_{D_2}.

$$R_{diss,H_2} = \Phi_{H_2} \cdot S_{H_2} \tag{5.5}$$

$$R_{diss,D_2} = \Phi_{D_2} \cdot S_{D_2} \tag{5.6}$$

The part of the impinging flux scattering without dissociating is given by the remainders, $\Phi_{H_2} \cdot (1\text{-}S_{H_2})$ and $\Phi_{D_2} \cdot (1\text{-}S_{D_2})$. Also, we may safely assume steady state conditions. It is most prominently observed in figure 5.2 in the flat HD intensity profile when the beam impinges onto the crystal. In a steady state, the surface coverage of H_{ads} and D_{ads} (Θ_H and Θ_D) do not change as a function of time. This requires that rates of change due to dissociation equal rates of change due to desorption for Θ_H and Θ_D independently. Desorption occurs in part as the original species, i.e. H_2 and D_2, and in part as HD. Therefore,

$$2 \cdot \Phi_{H_2} \cdot S_{H_2} = 2 \cdot k_d \cdot \Theta_H^2 + k_d \cdot \Theta_H \cdot \Theta_D \tag{5.7}$$

and

$$2 \cdot \Phi_{D_2} \cdot S_{D_2} = 2 \cdot k_d \cdot \Theta_D^2 + k_d \cdot \Theta_H \cdot \Theta_D \tag{5.8}$$

where k_d is the isotopologue-independent rate constant for desorption. Figure 5.8 illustrates this graphically, with colored areas indicating directly scatter flux (blue) and flux that dissociated but returned as the original isotope (red). The sum of these components do not result in a drop of the partial pressure while the beam impinges onto the sample. Their relative contributions cannot be distinguished. As our definitions of the H-D exchange probabilities for H_2 and D_2 (EPH_2 and EPD_2) are given by

$$EPH_2 = \frac{k_d \cdot \Theta_H \cdot \Theta_D}{2 \cdot \Phi_{H_2}} \tag{5.9}$$

and

$$EPD_2 = \frac{k_d \cdot \Theta_H \cdot \Theta_D}{2 \cdot \Phi_{D_2}}, \tag{5.10}$$

the observation that $EPH_2 > EPD_2$ by a factor of ∼1.5 requires that $\Phi_{D_2} \approx 1.5 \times \Phi_{H_2}$. This compares well with the ratio of flow rates used to create the three-component supersonic molecular beam (4 ml/min D_2, 2.9 ml/min H_2, and 1 ml/min Ar). Mass focusing in the molecular beam or differences in the calibration of the flow controllers may cause the remainder of the difference. Noteworthy, its higher incident kinetic energy lowers the dissociation probability in this regime for D_2 [26, 28–31].

When annealed at 1200 K, reactivity toward HD formation in figure 5.5 changes on both sides of the crystal. For the A-type step side, it is reduced over the entire range and only recovers when our molecular beam overlaps with the edge of the crystal. It actually becomes slightly more reactivity there, presumably because the higher annealing temperature allows cleans the sample holder better. The general reduction on this side of the crystal's apex is largest at Pt(655) or Pt[11(111)×(100)]. On the B-type step side, reduction in HD productivity is much more localized and centered at Pt(443) or Pt[7(111)×(110)]. From the linear relation between reactivity and step density observed for $T_{anneal} = 850$ K, results for 1200 K suggest dramatic surface structure changes that lower step densities on both A and B-type step sides.

The vicinal surface structure is determined by the balance between the step creation energy, the step-step repulsion energy, and the terrace energy [111]. A structure may become unstable if a physical variable (e.g. temperature) or chemical change (e.g. an im-

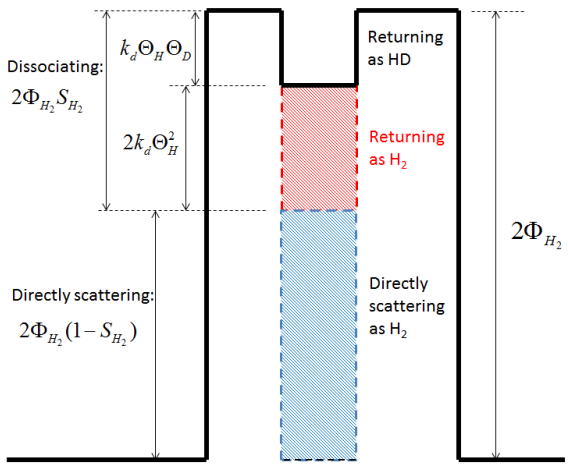

Figure 5.8: Graphical illustration of the relation between the measured partial pressures as the QMS intensity and the fluxes of H atoms impinging onto the sample and returning to the gas phase assuming instantaneous steady state conditions when opening and closing beam flags. While illustrated for H2, the identical picture holds for D_2 varying only by a different QMS sensitivity factor.

purity) causes changes to these energies. Several platinum surfaces are known to reconstruct. For example, step-doubling, which causes terraces to become twice as wide, has been reported by Somorjai and coworkers in a LEED study of Pt(997) being annealed in an O_2 atmosphere[112]. Comsa et al. also observed partial faceting and step-doubling of Pt(997) by high temperature annealing in oxygen using He atom diffraction and LEED[106, 107]. Hahn et al. also studied this system using He atom diffraction and scanning tunneling micrscopy (STM)[108]. First, they annealed the crystal in an oxygen atmosphere (1×10^{-7} mbar) at 700 K for several minutes and observed a partial step-doubling. Step-doubling was argued to be caused by modification of the step energy. On the clean surface, a double-height step costs more energy to create than two single monoatomic steps. If the interaction between the steps with attached O_{ads} lowers the energy cost for generation of double steps, step-doubling may appear. Second, they annealed the crystal at different temperature and observed thermal faceting on Pt(997). They demonstrated that thermal faceting is related to temperature-induced stress relief of the (111) terraces via reconstruction. Faceting is reversible. Annealing at 900 K for several minutes restored the nominal surface.

At any position along the curved surface, there will be a terrace

width distribution, similar or identical to those found on flat vicinal surfaces. The average terrace width is represented in LEED patterns by the spot-splitting to row-spacing ratio. With a curved Pt(111) single crystal very similar to ours, Walter et al. recently investigated the relation between the local surface structure and terrace width distribution using, a.o. scanning tunning microscopy (STM) and LEED[104]. They found linear relations over two regimes. For narrower terraces, step-step repulsion dominates and keeps distributions rather narrow. The ratio of the standard deviation, σ, to the average terrace width, $\overline{d}$, was found to be ~ 0.2. For wider terraces, entropy causes additional broadening of the distribution. It only sets in for (111) terraces of n $\sim$ 18 atom rows.

Our results in figure 5.5b, suggest that Pt(443) is more unstable at higher annealing temperatures than Pt(997). HD productivity reaches a local minimum at (443), whereas at (997) it is not much different from the data obtain for $T_{anneal} = 850$ K. We attribute it to a maximum in local restructuring, that reduces step density, hence the aiding effect of steps in dissociating impinging H_2 and D_2. If facets replace monoatomic steps, they are most likely of the $(11\overline{1})$ type, not of (110). Impinging reactants hit this facet at an angle of $\sim$70° from its surface normal. Luntz et al.[22] and we (see Chapter 3) showed that direct dissociative adsorption is hardly expected for this incident angle onto Pt(111) at the incident energies used here. Compared to the linear increase with step density for the 850 K case at Pt(443), the step-induced enhanced HD productivity (hence, the difference with the reactivity at the apex) drops by $\sim$ 33%. This requires that two-thirds of the monoatomic steps doubled, approximately one-half of the monoatomic steps tripled or a smaller fraction yielded larger facets. Interestingly, our LEED images taken nearest the (443) position in figure 5.6 and the intensity plots of the split spots in 5.7c show little difference. We believe this observation supports that only a small fraction of the surface has drastically changed, hence supporting the idea that larger $(11\overline{1})$ facets are formed rather than step doubling or tripling.

The absence of a significant change in HD reactivity resulting from the higher annealing temperature at the (997) location and the lack of significant differences in LEED patterns (figure 5.6 and 5.7) is also of interest. It shows that restructuring is very delicately dependent on terrace width. Whereas faceting appeared in studies of the nominal Pt(997) surface with its average 8-atom wide terraces[106–108], the

lack of an HD productivity drop argues against a significant loss of step density by faceting. From our experiments, it is clearly the 7-atom wide terrace that is the (most) unstable one in this vicinity. We believe that the previous ideas regarding restructuring of Pt(997) is actually a consequence of the 7-atom wide terraces occurring within the natural terrace width distribution present at the nominal flat Pt(997) surfaces studies by others. Walter et al. showed that the terrace width distribution increases linearly in this regime as a consequence of elastic interactions between steps[104]. For a terrace width of $n = 8$, a significant fraction of the distribution of terraces actually has slightly narrower terraces, e.g. $n = 7$. It seems likely that the observations of faceting on Pt(997) did not result from an instability of the 8-atom wide terraces, but from 7-atom wide terraces present on their samples. In this regard, it is of interest to reconsider whether a surface described by high Miller indices is actually well-represented using the Somorjai notation. The Miller index is derived from the macroscopic vector of the surface without specifying the local structure. It therefor does not imply a unique terrace width. The Somorjai notation describes the surface in terms of microfacets of a unique terrace width. At finite temperatures, the third law of thermodynamics requires entropy to deviate from unity. For a pure single crystal multiple microstates occur, which leads to the occurrence of a distribution of terrace widths.

On the A-type step side, changes in HD production after the higher temperature anneal cycle are much more drastic than on the B-type step side. At the (655) surface, reactivity is nearly identical to the (111) apex. Hence, step density must have been reduced so drastically that the additional reactivity provided by the few remaining steps only offsets the loss of active surface area from formation of (100) facets. The LEED diffraction patterns also show a clear loss in intensity near this position on the crystal in figure 5.7. Although spot-splitting does not change, hence the average step density not being altered, large amounts of faceting here results in a change in the intensity ratio of the split spots. We believe this is caused by narrowing of the sinusoidal intensity variation from (111) facets facing the LEED optics, while spot-splitting is not affected as the macroscopic angle does not change [12]. Hence, while the less intense spot suffers from narrowing of the (111) sinusoidal intensity variation, the more intense spot benefits. The lack of other spots appearing in LEED patters, suggests that there is no ordering to the (100) facets. The observation that the HD reactivity

is affected over a much broader ranges on the A-type step side of the apex than on the other side, suggests that (100) facet formation occurs much more readily than $(11\bar{1})$ facet formation. The step-step repulsion energy could be larger for A-type steps than for B-type steps, but the similarity of the step width distributions in the study by Walter et al. does not support this [104]. Stronger step-step interactions should cause a narrowing of the ratio of σ to $\bar{d}$. As the free energy of the 100 terraces is higher than that of 111 terraces, the different behaviors must be due to a step creation energy. Apparently, it is higher for the Pt A-type step than for the B-type step. Comsa et al. came to the same conclusion in an STM study of the shape of hexagonal pits in Pt(111) planes[113].

We come the conclusion that our chemical H-D exchange probe of surface structure competes very well with the physical probe of electron diffraction in studying reconstruction of stepped surfaces. Our MCP-LEED yields images from which we extract spot-splitting, agreeing very well with theoretical calculations of the ideal stepped surfaces. The vertical spot splitting indicates that steps lie horizontally on the surface. From qualitative interpretation of intensity plots we gather some information on potential surface structure changes, that are, however, much more easily observed in the H-D exchange when monitoring HD as a product. The same key points are present in the loss of H_2 and D_2, as represented by the H-D exchange probability, but signal-to-noise levels are much worse. The size of our molecular beam is also smaller than the electron beam from the LEED optics, leading to higher spatial resolution. In the absence of STM capability, the combination of LEED and the H-D molecular beam exchange probe allow us to study conditions leading to surface restructing and confirm which conditions lead to a linear relation between step density and distance to the apex for this Pt curved crystal.

On a final note, we return to the combined STM-photoemission study by Walter et al.[104]. They use repeated sputtering and annealing cycles to clean their surface, very similar to our methods. They anneal their crystal at 1073 K, whereas the Pt(997) surface is known to develop faceting at 980 K[106–108]. Our measurements confirm faceting in this regime using a higher annealing temperature, and suggest that it is probably Pt[7(111)×(110)] that restructures much more so than Pt[8(111)×(110)]. The absence of any comments on restructuring in this regime in Walter's paper is disturbing, especially since

they do comment on lack of evidence for macroscopic alterations in the curvature of the crystal.

5.5 Summary

At low incident kinetic energy, HD formation from a mixed H_2-D_2 molecular beam on a curved Pt surface is related to Pt step density. Using the appropriate cleaning procedure with a final anneal step of 850 K, a smooth step density gradient is represented by a linear increase in HD formation with distance from the crystal's (111) apex. A LEED study confirms the orientation of steps relative to the curvature of the crystal and suggests the same smooth variation in average terrace width. When annealed at 1200 K, HD formation is clearly reduced over the entire on A-type step side, most predominantly near (655), most likely resulting from (100) facet formation. On the B-step side, faceting occurs very locally at (443). LEED studies fail to show this ostentatiously. We only find indirect evidence of restructuring in intensity variations of split spots. Our H-D exchange probe is therefore much more sensitive to local restructuring than LEED. Noteworthy, the spatial resolution allows us to pinpoint positions where a delicate balance between step-step repulsion, surface and step energies, leads to restructuring more facile than experiments using flat single crystals studied using STM. It even allows us to correct the previously assumed restructuring of Pt[8(111)×(110)] from He atom diffraction, LEED and STM measurements on Pt(997) indicating that it is actually Pt[7(111) × (110)] that causes faceting. For reason of the (hkl) Miller indication for a real vicinal surface at finite temperature inherently requiring a distribution of stepped (or kinked) surfaces, rewriting it in the Somorjai notation, for example as [n(111) × (110)], is formally incorrect. A distribution cannot solely be described by its average.

Chapter 6

The two faces of step defects in O_2 reaction on Pt

6.1 Introduction

Molecular oxygen's dissociation on the surface of platinum - a metal typically used as catalyst in proton exchange membrane (PEM) fuel cells [3] and to treat automotive exhaust gases [2]- is known to be complex [114, 115]. Besides a physisorbed state, in which the molecule shows rotational and vibrational characteristics very similar to gas phase O_2 [116–119], there are at least two molecular chemisorbed states. A superoxo species, O_2^-, and a peroxo species, O_2^{2-}, have been identified on the large atomically flat planes of a Pt(111) single crystal [119–122]. These molecular states are precursors to dissociation, which leaves two adsorbed oxygen atoms, O_{ads}, on the surface. The dynamics of adsorption show parallel characteristics of direct and precursor-mediated processes, although the latter contributes only significantly at low surface temperatures [123, 124]. Dissociation does not happen directly upon impact, but proceeds via molecular chemisorbed states [125, 126].

Although easiest to model from a theoretical perspective, Pt(111) is not very representative of the surface structure dominating nanometer-sized Pt catalyst particles. Experimental molecular dynamics studies on various nanostructured Pt surfaces [109, 127, 128] show that step edges induce a dominance of the indirect dissociation mechanism - one presumably proceeding via the physisorbed molecular state [123]. Scanning Tunneling Microscopy (STM) and Temperuture Programmed

Desorption (TPD) studies confirm that monoatomic steps are more reactive in dissociating O_2 than (111) terraces [129, 130]. Theoretical studies discriminate between various molecularly chemisorbed states, both at steps and terraces [129, 131, 132], but calculations of sticking supporting dynamical multiple processes have so far only considered Pt(111) [133, 134]. A tight-binding molecular dynamics approach also challenged the interpretation of indirect adsorption via a physisorbed state [133].

Recently, two new experimental techniques have been developed that allow detailed testing of surface structure and stereodynamical dependencies in O_2 sticking to surfaces. In combination with supersonic molecular beam techniques, curved single crystal surfaces, were recently shown to resolve outstanding issues regarding the dynamics of Pt catalyzed H_2 dissociation [101]. In combination with a high pressure reactor, step-induced induction of CO oxidation on Pd was revealed [135]. The essential ingredient is the controlled continuous variation of step densities over two orders of magnitude on the surface of a single crystal. The top section of figure 6.2 schematically illustrates such a curved single crystal.

The second new technique is state-selection of O_2 using a magnetic hexapole with subsequent steering of the molecule's rotational axis prior to its impact onto the surface [136, 137]. For Pt(111), this technique provided direct evidence that activated adsorption into the chemisorbed superoxo and peroxo states is sensitive to the orientation of O_2's internuclear axis upon impact [138]. Molecules oriented parallel to the (111) plane more easily find their way into molecular chemisorbed states than those oriented perpendicular to that plane. This phenomenon was also shown to control CO oxidation kinetics [139].

Here, we report on the first experimental study of dynamical dependences combining the above-mentioned new techniques. First, we studied the structure and energy-dependencies for O_2 sticking using a curved Pt single crystal in Leiden, the Netherlands. Subsequently, we studied the orientational dependence for O_2 sticking onto three flat single crystals representing the outer edges and center of the curved crystal in Tsukuba, Japan.

6.2 Experimental methods

For measurements performed in Leiden, the Netherlands, we used the same supersonic molecular beam apparatus as described in our previous study of O_2 sticking and dissociation on Pt(553) [109]. Supersonic expansion of O_2 in various seed gases allows us to vary the incident energy, which we determine by standard time-of-flight (TOF) techniques. Sticking is measured using the King and Wells approach. To attain high local resolution, the molecular beam is skimmed to a rectangular shape with a surface area of 0.12 x 6.0 mm^2 at the curved crystal's position. The curved crystal is cleaned by sputtering at 0.5 keV with $\sim 2.0\ \mu A$ Ar^+ current ($p_{Ar} = 6.0 \times 10^{-6}$ mbar) for 5 minutes at surface temperature, T_s, of 900 K. This is followed by oxidation at the same surface temperature (3 minutes, $p_{O_2} = 3.5 \times 10^{-8}$ mbar) and annealing at 1200 K for 3 minutes. This cleaning procedure is repeated 3-5 times before the last cleaning cycle. For the last cycle, we only sputter and anneal at 850 K. We use LEED and Auger Electron Spetroscopy (AES) (OCI BDL800IR-MCP) to verify surface order and cleanliness across the curved surface.

Two 10 mm diameter flat single crystals exposing either the (533) or (553) surface were used to determine the absolute sticking probabilities for comparison to data obtained with the curved Pt single crystal. These crystals were cleaned by sputtering at 0.5 keV with $\sim 2.0\ \mu A$ Ar^+ current ($p_{Ar} = 6.0 \times 10^{-6}$ mbar) for 5 minutes at surface temperature, T_s, of 900 K. This is followed by oxidation at the same surface temperature (3 minutes, $p_{O_2} = 3.5 \times 10^{-8}$ mbar) and annealing at 1200 K for 3 minutes. This cleaning procedure is repeated 3-5 times before the KW measurement. For flat crystals, we use small hole with diameter of 1.6 mm as the final aperture. The molecular beam is shaped into a cycle with diameter of 3.2 mm at the crystal position.

Stereodynamically sensitive experiments performed in Tsukuba, Japan, were also performed using an apparatus described before [136, 137]. Briefly, supersonically expanded mixtures of O_2 in He pass through a magnetic hexapole containing a variable number of hexapole elements. The number of elements is chosen to optimize the cleanliness of the (2,2) state resolution for each kinetic energy. Three sets of Helmholtz coils are placed on the outside of the UHV chamber that houses the Pt(553), Pt(533) or Pt(111) crystals upon which the state-selected O_2 molecules impinge. Currents through the Helmholtz coils

are alternated every 2 seconds to switch between two impact geometries for O_2 while sticking is measured using the King and Wells technique. Every experiment using two impact geometries is performed at least twice also using the reversed order in alternating between impact geometries. Initial sticking probabilities are obtained by exptrapolating the best fit of a double exponential functional form to data over a nearly 60 s time frame to t = 0. We use two filters to separately fit results for the two impact geometries. This extrapolation removes various convolutions at the start of the experiment. Reported sticking probabilities are averaged for experiments with the original and reversed orders.

A typical KW experiment where the orientation of the incident rotating molecule is switched between helicoptering (H) and cartwheeling along the z axis (C_z) at an incident kinetic energy of 0.33 eV along the [111] normal of Pt(553) is shown in figure 6.1. The main panel shows as a blue line the time-dependent sticking probability during the entire experiment. The solid black and red lines are two fits to the data using a double exponential form. These fits are applied only for selected times that either H or C_z molecules impinge. The filters also cut out the rise times in the signal after switching. The inset in figure 6.1 shows the filters at the top of the graph for the first 20 s of the experiment for H (black) and C_z (red) in a high/low fashion. When the filter is high, data are used for the fit. When it is low, data are not used for the fit. The fits are shown in the inset as dashed black and red traces.

The two initial sticking probablities following from each experiment for a combination of H, C_z, and C_y, or from R and L, are calculated from the fit parameters using t = 0. We also repeat each experiment with reversal of the switching order of the two chosen orientations. Reported values for ratios in the manuscript are calculated from the averages of both orders, e.g. H vs C_z and C_z vs H.

6.3 Results

At the top of Figure 6.2, we present an illutration of our curved Pt single crystal. It curves 31° along $[11\overline{2}]$ with the apex centered at the (111) plane. The macroscopic curvature is a consequence of a smooth variation in density of monoatomic steps of the A and B-types (insets)

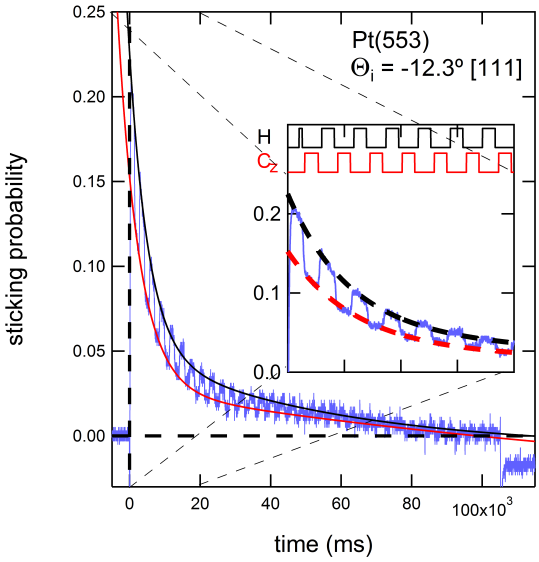

Figure 6.1: An example of a KW measurement for a state-selected (2,2) beam impinging onto Pt(553) at E_{kin} = 0.33 eV and an incident angle of -12.3 ° relative to the surface normal, i.e. along [111]. The Helmholtz coils are set to switch the incident molecules from helicoptering (H) to cartwheeling along the z axis (C_z). The blue line in the main panel shows the KW trace, whereas the black and red solid lines are fits to the data using double exponential functional forms and filters. The inset shows a detail of the KW trace and fits (dashed black and red) for the first 20 s of the experiment. In the upper part of the inset the filters (solid black and red) used to fit the data are shown as high/low for the filter being active/inactive for the indicated rotational orientation of the molecule.

[104, 140]. These A and B-type steps expose, respectively, the shortest possible (100) and (110) facets. We probe the O_2's initial sticking probability, S_0, locally across surface structures from approximately the 6-atom wide (111) planes separated by A-type steps via very large (111) planes at the apex to 6-atom wide (111) planes separated by B-type steps. The width of our molecular beam at the crystal position is 0.12 mm, hence approximately equal to the size of the symbols used to indicate data (open symbols). At the surface temperature of the crystal, T_s, equaling 150 K, the physisorbed state of O_2 is unstable. At the (111) terraces and both steps, O_2 molecules stick molecularly in a chemisorbed state, and/or dissociate. If they (in)directly scatter into the gas phase, it occurs on a time scale much faster than our measurement. The exact final state - dissociated or molecularly chemisorbed - is inconsequential to our findings.

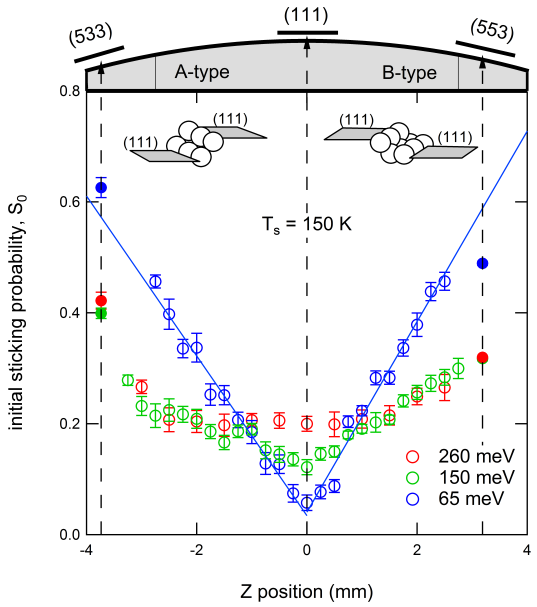

Figure 6.2: Initial sticking probability of O_2 as a function of incident position on a curved Pt single crystal for 65, 150 and 260 meV incident energy at T_s=150 K. Open symbols represent data gathered using the curved single crystal that is schematically represented at the upper side of the graph. Solid symbols were gathered using flat single crystals with (533) and (553) surface structures. Error bars reflect the standard deviation calclulated from multiple measurements. Insets show the local step structure for the A and B type steps.

At the lowest incident energy, E_{kin} = 65 meV, indicated by blue open circles, sticking is linearly dependent on the position over the entire crystal. As the Z position scales linearly with step density, reactivity is a linear sum of independent reactivities at steps and terraces [28, 30]. The solid blue lines represent the best fit to the data at the lowest incident energy. We used only data collected on either the A or B side of the crystal for these fits. Both fits indicate a residual reactivity of 0.04 at the ideal (111) plane. For reference, solid symbols indicate data collected under identical conditions using flat single crystals with (533) and (553) surface structures. These surface structures have 4-atom wide (111) terraces separated by the (100) and (110) facets. Their comparable locations on the curved crystal surface are indicated by vertical dashed lines with arrow heads. Tapering of the polished surface in this regime prohibits accurate measurements using our curved crystal. While for B-types steps, extrapolation of the data

collected on the curved crystal slightly overestimates the reactivity determined for the (553) surface, reactivity is accurately reproduced for the A type step for (533). The steepness of the slopes and their nearly identical absolute values on both sides indicate that the dynamic process resulting in sticking is dominated by steps and insensitive to the local arrangement of Pt atoms forming the step.

At higher incident energies, indicated by the green and red open and solid circles, the reactivity at the (111) apex increases from 0.04 at 65 meV to 0.2 for E_{kin} = 260 meV. The additional contribution of steps diminishes. Reactivity on both sides of the crystal, as well as on the flat (533) and (553) surfaces drops quite dramatically. This energy dependence agrees with previous studies for the (111)[123, 124], (533) [128] and (553)[109] surfaces. Whereas at an incident energy of 150 meV (green), both sides of the crystal still reflect an approximate linear dependence over a reasonably large step density range, at 260 meV the dependence clearly looses it linear character. Beyond 2 mm from the apex, additional kinetic energy has no effect on reactivity, as also found previously for flat single crystals. Particularly A-type steps show non-linear dependence of reactivity on step density in the regime of 4 to 6 atom wide terraces. For wide (111) terraces at the highest incident energy, i.e. near the apex, both step types do not increase reactivity. Clearly, dynamical processes leading to sticking at higher incident energies are not dominated by steps alone.

Figure 6.3 shows the results of experiments testing the dependence of S_0 on the alignment of the O_2 molecule upon impact over a wide range of kinetic energies. A magnetic hexapole selects molecules from a supersonic expansion in the (J,M) = (2,2) state. This state is well described as the $^3\Sigma$ electronic ground with the angular momentum vector of body rotation being aligned parallel to the quantization axis[137]. Coupling of the magnetic moment of this quantum state to an externally applied magnetic field allows us to steer the rotational axis of the molecule prior to impact. In panel a) of figure 6.3, we reproduce with blue diamonds our results published recently for Pt(111)[138]. It plots the ratio of the initial sticking probabilities of molecules impinging onto the surface with a helicoptering motion, $S_0(H)$, and a carthweeling motion, $S_0(C)$, relative to the plane of the Pt surface. As there is no difference for carwheeling motion with respect to the two independent vectors defining the surface plane, we show $S_0(H)/S_0(C)$ without specifying the direction of J with respect to the surface for

cartwheeling molecules. The data clearly show the preference in sticking for helicoptering molecules. This is most explicitly observed at the lowest impact energies, i.e. when the molecule has barely enough kinetic energy to overcome the energetic barrier to chemisorption into a molecular states. This result reflects that chemisorbed states have their O_2 internuclear axis aligned parallel to the surface.

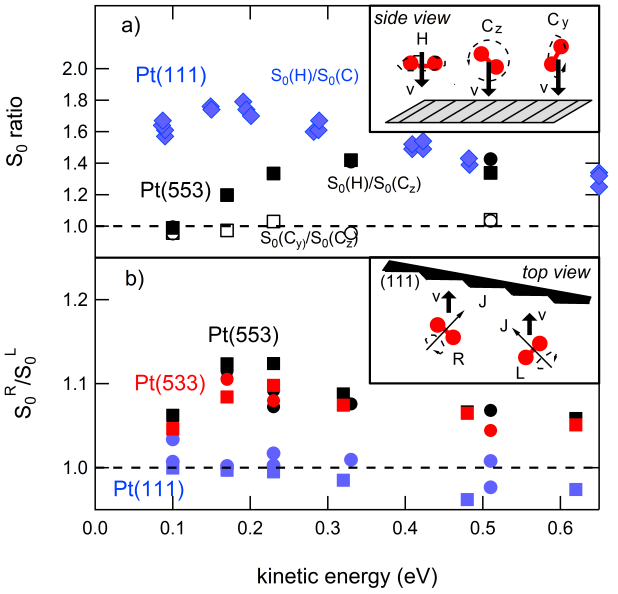

Figure 6.3: In panel a), the sticking probability ratio for helicoptering (H) and cartwheeling (C) O_2 molecules on Pt(111) is shown (blue diamonds) as a function of incident energy. Also shown are the same ratio's for H and C_z (black solid) and C_y and C_z (black open) for Pt(553). Circles indicate impingement along [553], squares along [111]. The inset depicts the various rotational motions relative to the (stepped) surface. Panel b) shows the ratio S_0^R/S_0^L for Pt(111) (blue symbols), Pt(553) (black symbols) and Pt(533) (red symbols) as a function of kinetic energy. The inset depicts the variation in impact geometry for R and L orientations relative to the stepped surfaces. The surface temperature for all data shown in this figure lies in the range of 300 to 400 K.

The black symbols in panel a) of figure 6.3 represent new data, i.e. initial sticking probability ratios for O_2 on Pt(553). Here, we separately show $S_0(H)/S_0(C_z)$ (solid) and $S_0(C_y)/S_0(C_z)$ (open). Circles and squares, which often overlap, differentiate between the experiment being performed with impact along the macroscopic surface normal and impacting along the normal of (111) terraces. The angular difference of $\sim 12°$ has no effect on the results. We separately show the

ratio for C_y and C_z because cartwheeling rotational motion may be sensitive to the alignment of the O_2 axis with respect to the direction of the monoatomic steps on the surface. Data suggest it is rather insensitive to this variation. On the contrary, the ratio of sticking for helicoptering and cartwheeling molecules for Pt(553) clearly deviates from unity. The effects depends on incident energy. While at the lowest kinetic energy the ratio $S_0(H)/S_0(C_z)$ is close to unity, it increases with incident energy to a value of ~ 1.4. This contrasts with the results for Pt(111), where at low energy a strong alignment effect was observed. The B-type steps remove the preference for sticking with a molecular axis parallel to the surface entirely at low incident energy. Notably, at higher incident energy, the sticking probability ratio $S_0(H)/S_0(C_z)$ for the (553) and (111) surfaces merge to the same value.

In panel b) of figure 6.3, we show the results of a different type of experiment. Instead of switching between H and C, we arranged the magnetic field such that molecules flip their rotational axis from +45° (R) to -45° (L) with respect to the velocity vector, v. We ensure that molecules impinge normal to the (111) terraces of three flat single crystals, i.e. Pt(111) (blue), Pt(553) (black) and Pt(533) (red). For the Pt(111) crystal, switching between these R and L states has no effect. These two states are geometrically equivalent on a flat (111) surface. For each energy, we checked that the ratio S_0^R/S_0^L was indeed (nearly) unity for the Pt(111) surface. For the stepped surfaces, this is clearly not the case. Molecules with the J vector oriented as in R, rotate such that the internuclear axis is always roughly parallel to the step facet. To the facet, the molecule looks like it is helicoptering. Rotation as in L combines molecular impact with the internuclear axis being both parallel and orthogonal to the step facet, strongly resembling a cartwheeling motion. Results for A and B type steps, as represented by the Pt(533) and Pt(553) surfaces, indicate that both step types clearly favor molecules impacting with their internuclear axis parallel to the step's (100) or (110) facet. As this experiment is very sensitive to local magnetic fields and details of data analysis, figure 6.3b shows two sets of data by squares and circles gathered independently by two of the authors.

6.4 Discussion

The combined low incident energy results from figure 6.2 and figure 6.3a definitively confirm the hypothesized influence of steps on sticking and dissociation of O_2 at low incident energy. Based on a comparison of the energy-dependence for various stepped Pt surfaces, Jacobse et al. proposed that the dominating contribution to reactivity results from an indirect mechanism that mostly depends on step density[109]. Step type was found not to be of importance to the kinetic energy dependence in the low energy regime. Results of sticking on Pt(533), Pt(553) and Pt(111)(2x1) were nearly identical. The linear dependence of reactivity on step density in figure 6.2 confirms that reactivity is dominated by a dynamical mechanism dependent on steps. The slopes being nearly identical also indicates that this mechanism is indifferent to step type. At the same time, the data in figure 6.3a indicate an independence on the orientation of the internuclear axis at this energy as both sticking probability ratios for molecules with different alignement are all approximately unity. Such indifference is characteristic for a dynamical mechanism that proceeds via a physisorbed state[141]. Such states are only weakly bound. As the potential energy surface for such a state has no strong angular corrugation (they resemble the gas-phase species), scattering into the state is not expected to depend critically on the orientation of the internuclear axis during the collision. The strong dependence on alignment for Pt(111) observed at the lowest energy is a consequence of sticking being predominantly direct into a chemisorbed state. These molecular chemisorbed states are aligned on the surface. Adsorption is favored when the O_2 molecular axis is parallel to the surface during collision. Hence, the lost of the alignment dependence for stepped surfaces in the low energy regime indicates that indirect scattering into a physisorbed state causes the high reactivity as compared to the Pt(111) surface.

With increasing kinetic energy, the results presented in figures 6.3a and 6.3b may seem at odds. While the former suggests that (111) and stepped surfaces have an alignment dependence of equal magnitude at the highest incident energy, favoring H over C with a sticking probability ratio of 1.4, the latter indicate that stepped surfaces show a dependence on alignment whereas (111) does not. However, results in figure 6.3a do not discriminate between alignment effects resulting from impinging onto steps and terraces. At higher incident energies,

the dominance of the dynamical mechanism relying on scattering into a physisorbed state has disappeared. Results in figure 6.2 clearly shows this through the loss of reactivity dependence on step density. Hence, at higher incident energy, direct adsorption into molecular chemisorbed states dominates. This occurs both at steps and terraces. In figure 6.3a, the contributions to direct chemisorption at steps and terraces are mixed. Figure 6.3b, however, shows that the step facets have a unique stereodynamical preference for direct molecular chemisorption as the experimental design removes the contribution of the (111) terraces.

The absolute value of S_0^R / S_0^L seems small in comparison to S_0(H) / S_0(C). It ranges between 1.05 and 1.13, whereas the latter reaches 1.8 for Pt(111). However, this comparison is not fair. The ratio S_0^R / S_0^L results from a minority of O_2 molecules impacting directly onto step sites. Most molecules impact onto the 4-atom wide (111) terraces of the stepped surfaces. The facet may be estimated to contribute at most on the order of one third to the surface area of the unit cell for (533) and (553) [28, 29]. Second, for a quantitative comparison, probability distribution functions for impact with the internuclear axis parallel or perpendicular to any facet need to be taken into account. For the comparison of H and C on (111), the difference in these distributions is largest as H lies truly parallel to the (111) plane. In the R versus L experiment, the facets do not probe the difference as cleanly as their angle from (111) is not 45°. These two considerations suggest that the preference for helicoptering over cartwheeling motion to stick to the step's facet is probably similar to that observed for H and C on Pt(111).

6.5 Concluding remarks

The results of our study show that the influence of steps to alignment dependences in sticking op O_2 are two-faced. Through strongly enhancing the scattering probabilities into a physisorbed state, alignment sensitivity to adsorption and dissociation is entirely lost on highly corrugated surfaces. However, with increasing impact energy, direct adsorption into chemisorbed states becomes increasingly dominant. Similar to (111) terraces, step facets show a preference for molecules being aligned parallel to their surface. Cartwheeling motion relative to the

step direction reduces sticking. The effect shows a clear energy dependence between 0.1 and 0.3 eV, suggesting that adsorption into a chemisorbed state at the step is still (weakly) activated.

Chapter 7

Summary and outlook

7.1 Summary

Heterogeneous catalysis has been applied throughout human history even when people had no knowledge about the processes involved. To investigate the mechanisms of chemical reactions, simple "model systems" are generally used. Chemical reactions in model systems occur with the same elementary steps as catalytic processes under realistic conditions. Although such systems have been studied extensively, many details are not yet clear. In this thesis we focus on simple systems, such as hydrogen dissociation on Pt and Cu surfaces and oxygen dissociation on Pt surfaces.

Hydrogen dissociation on Pt surfaces is a model system for weak (non) activated diatomic molecule dissociation. It has been studied extensively using both experiments and theoretical calculations. The potential energy surface (PES) shows both energetic and geometric corrugation. Using an adjustable Specific Reaction Parameter (SRP) approach to DFT, calibrated by Ghassemi et al. on data of D_2 dissociation on Pt(111) by Luntz et al., good agreement between theory and experiment[22, 39] has been obtained. Their results predict a weak difference in sticking probabilities for two different azimuthal angles at high polar angle incident and high kinetic energies. In chapter 3 we studied hydrogen dissociation on Pt(111) surface. Our data agree well with the earlier experimental work. The reaction only depends weakly on the azimuthal orientation of the incidence plane, which is consistent with the SRP-DFT calculations.

Hydrogen dissociation on Cu surfaces is a model system for strongly

activated dissociative adsorption of diatomic molecules on a metal surface. It is also important as the first step of hydrogenation of CO_2 to methanol over a $Cu/ZnO/Al_2O_3$ catalyst. Understanding of elementary reaction steps may help development of new catalysts. To mimic the edges on real catalyst particles, macroscopic flat surfaces with atomic steps are introduced. The lower coordination of step atoms usually lowers dissociation barriers by increasing the binding energy. In chapter 4 we studied hydrogen adsorption and desorption on the Cu(111) and Cu(211) surfaces. The latter contains A-type steps and the (111) terraces. Here, we find that the Cu(111) surface is more reactive than the Cu(211) surface. A-type steps cause a - to our understanding unique - upward shift in the distribution of activation barriers to adsorption and a downward shift in barriers to desorption. Furthermore, the barrier distributions, which are weakly dependent on hydrogen pre-coverage and saturation coverages, are shown to depend on incident energy. Lateral interactions between adsorbed hydrogen atoms must be weak, especially in the lower coverage regime.

In chapters 5 and 6 we moved onto a curved Pt(111) single crystal. The apex of this crystal is Pt(111). The crystal contains monoatomic A-type steps on one side and B-type steps on the other. The step density increases linearly with the distance from the apex. This crystal can mimic a series of stepped surfaces with A or B steps. To some degree, this overcomes the materials gap between a single crystal surface and real catalysts.

In chapter 5 we studied HD formation on the curved Pt(111) single crystal surface. At low incident energy, HD formation on Pt surfaces is known to be depended on the step density. Using a proper cleaning procedure and a final annealing at 850 K, we observed a linear increase of HD formation with distance from the apex. This indicates the step density increases linearly with distance from the apex. A LEED study confirms this linear increase through the spot splitting observed in LEED patterns. When the crystal is cleaned using the same procedure but followed by a final annealing at 1200 K, HD formation is reduced on both sides. For A-type steps, HD formation is reduced over the entire range, especially near (655). For B-type steps, HD formation is reudced locally at (443). The reduction indicates the presence of faceting, but LEED fails to show this ostentatiously. HD formation as a chemical probe is more sensitive than LEED. More details about the reconstruction need to be studied by STM. Our data also show

that faceting occurs at (443), not at (997). The Pt(997) surface was previously shown to reconstruct and studied by He atom diffraction, LEED and STM.

The dissociation of oxygen on Pt is more complex than that of hydrogen. The process involves at least four states: a molecular physisorbed state, at least two molecular chemisorbed states and an atomic oxygen chemisorbed state. Previous studies have shown that step edges induce a dominance of the indirect dissociation mechanism - presumably proceeding via the physisorbed molecular state, and more reactive in dissociating O_2 than (111) terraces. In chapter 6 we studied O_2 dissociation on Pt surfaces using the same curved Pt(111) single crystal. The sticking probability of O_2 increases linearly with the distance from the apex for both A- and B-type step sides at the lowest incident energy, 65 meV. The steepness of the slopes and the nearly identical absolute values on both sides indicate that the dynamic processes leading to sticking is dominated by steps and insensitive to the step type. At higher incident energies, this dependence clearly starts to loose its linear character. This indicates that the dynamical processes leading to sticking at higher incident energies are not dominated by steps alone. By using a alignment-controlled O_2 beam, sticking of oxygen on flat Pt(111) surfaces preferentially occurs when the internuclear axis is aligned parallel to (111) surface. For the Pt(553) surface, the preference for O_2 sticking with a molecular axis parallel to the surface entirely disappears at low incident energy. At higher incident energy, the sticking probability ratios $S_0(H)/S_0(C_z)$ for the (553) and (111) surfaces converge to the same value. The results of R and L experiments indicate that dissociation on both A- and B-type steps is clearly favored for molecules impacting with their internuclear axis parallel to the step's (100) or (110) facets.

7.2 Outlook

Besides our studies presented above, there are two ways to improve our current understanding of the relationship between surface structure and chemical reactivity. The first improvement is by using STM to probe the local structure with (near) atomic resolution. The second improvement is preparing reactants in the molecular beam in a more controlled fashion, e.g. dividing the reactants into two well-controlled

molecular beams.

7.2.1 STM

As shown in chapter 5, local structures on the curved Pt(111) single crystal surface change with the annealing temperature. By using HD formation as a chemical probe, we clearly observed a reactivity difference with two different annealing temperatures, 850 K and 1200 K. However, this method cannot directly demonstrate the difference of the micro-structure on the surface. LEED is usually a good technique to study the local surface structure. However, in our studies of the curved Pt(111) single crystal, it proved to be less sensitive to local reconstructions than HD formation. The origin of this is that LEED is an averaging technique, which averages the step densities over the probed area. For a flat single crystal, this averaging is not a problem because the probed surface area is uniform. For a curved single crystal with a smooth gradient of step densities, this averaging makes LEED less sensitive to local structure changes. Hence a technique with (near) atomic resolution is needed to probe the local structure.

Scanning tunneling microscopy (STM) is an appropriate technique for this purpose. STM has been used to study the local structures of curved single crystals by other groups[104, 105, 135, 142]. The technique could reveal the local terrace width distribution across the curved crystal and identify the reconstructions. Therefor the chemical reactivity and the local structure can be correlated to one another.

We can also study the types of reconstruction, e.g., step-doubling, faceting and step bunching, on the A- and B-type step sides of the curved Pt(111) single crystal. Furthermore, the dynamics of reconstruction can be studied by varying the annealing temperature, annealing time and cooling rate. This provides a physical aspect of surface reconstruction and can be used to design the geometry of real catalytic nanoparticles.

7.2.2 Double beam

All experiments in this thesis were carried out by using a single supersonic molecular beam (SMB). For experiments with multiple reactants, we usually mixed the reactants into one beam. To prevent reactions from taking place in the nozzle, we avoided heating the nozzle too

much. This limited the energy range we could probe. As an example, we have attempted to increase the kinetic energy of D_2 by seeding D_2 in H_2. When the nozzle was heated to high temperatures, like 800 °C, most of the D_2 was converted to HD. This made the D_2 signal too low to be measured by QMS. We have also tried to measure the hydrogenation of CO_2 by seeding CO_2 in H_2. A large amount of H_2O and CO were generated in the nozzle when heated to high temperature. To overcome this problem, a possible method is pre-adsorbing other reactants through background dosing and providing the main reactants by the SMB. The possible drawback of this method is that the coverage of the background adsorbing reactants may be very small which will probably limit the reaction. The other method is dosing several reactants continuously from the background. In both methods, the main issue is that the reactants supplied from background dosing are barely controlled.

There are two molecular beams connected to our UHV apparatus. One is a supersonic molecular beam and the other is an effusive molecular beam (EMB). In the future we hope to be able to study reactions by using these two beams simultaneously. We can then separate reactants that may react. The ratio of reactants in SMB and EMB can be adapted by changing the flow rates of the flow controllers or by chopping the SMB or EMB. With the usage of these two molecular beams, a series of reactions can be investigated, for example, the HD formation by using H_2 and D_2, CO oxidation by using CO and O_2 and CO_2 reduction by using CO_2 and H_2.

7.2.3 Lock-in amplified detection

In chapter 4 we showed that the small sticking probability can be directly measured by averaging multiple KW measurements. This method improves the signal-to-noise ratio. The KW technique can also be improved by using lock-in amplification. The second flag in our UHV chamber is a wheel with a 50% duty cycle divided over two "open" sections of equal size. It is firmly attached to the axis of a UHV-compatible stepper motor (Arun Microelectronics). Previously we only used it to control impingement of the beam onto the crystal within the UHV chamber in an "on/off" fashion by a single quarter turn of the wheel. However, we can also turn it continuously to chop the beam. In this way, the sticking probability can be detected by

combing with the lock-in amplifier. There is another way to apply lock-in amplifier. The nozzle of the EMB can be moved along the beam axis backward and forward periodically by using a motor. This periodic movement can change the distance between the nozzle and the first skimmer, and thus change the intensity of the EMB periodically. This can also be combined with the lock-in amplifier.

Bibliography

[1] J. J. Berzelius. Considerations respecting a new power which acts in the formation of organic bodies. *Edinburgh New Philosophical Journal*, 21:223–228, 1836.

[2] G. C. Koltsakis and A. M. Stamatelos. Catalytic automotive exhaust aftertreatment. *Progress in Energy and Combustion Science*, 23(1):1–39, 1997.

[3] N. M. Marković, T. J. Schmidt, V. Stamenković, and P. N. Ross. Oxygen reduction reaction on Pt and Pt bimetallic surfaces: a selective review. *Fuel cells*, 1(2):105–116, 2001.

[4] I. Langmuir. The mechanism of the catalytic action of platinum in the reactions $2CO+O_2=2CO_2$ and $2H_2+O_2=2H_2O$. *Transactions of the Faraday Society*, 17:621–654, 1922.

[5] C. N. Hinshelwood. On the theory of unimolecular reactions. *Proc. R. Soc. Lond. A*, 113(763):230–233, 1926.

[6] D. D. Eley and E. K. Rideal. Parahydrogen conversion on tungsten. *Nature*, 146(3699):401, 1940.

[7] D. D. Eley. The interchange of hydrogen in the adsorbed film on tungsten. *Proc. R. Soc. Lond. A*, 178(975):452–464, 1941.

[8] J. Harris and B. Kasemo. On precursor mechanisms for surface reactions. *Surface Science Letters*, 105(2-3):L281–L287, 1981.

[9] P. Mars and D. W. van Krevelen. Oxidations carried out by means of vanadium oxide catalysts. *Chemical Engineering Science*, 3:41–59, 1954.

[10] D. A. King and M. G. Wells. Reaction mechanism in chemisorption kinetics: nitrogen on the {100} plane of tungsten. *Proc. R. Soc. Lond. A*, 339(1617):245–269, 1974.

[11] B. Riedmüller, F. Giskes, D. G. van Loon, P. Lassing, and A. W. Kleyn. A compact molecular beam line. *Measurement Science and Technology*, 13(2):141, 2001.

[12] M. Henzler. LEED-investigation of step arrays on cleaved germanium (111) surfaces. *Surface Science*, 19(1):159–171, 1970.

[13] R. V. Mom, C. Hahn, L. Jacobse, and L. B. F. Juurlink. LEED analysis of a nickel cylindrical single crystal. *Surface Science*, 613:15–20, 2013.

[14] A. den Dunnen, L. Jacobse, S. Wiegman, O. T. Berg, and L. B. F. Juurlink. Coverage-dependent adsorption and desorption of oxygen on Pd(100). *The Journal of chemical physics*, 144(24):244706, 2016.

[15] D. J. Auerbach. Velocity measurements by time-of-flight methods. In G. Scoles, editor, *Atomic and Molecular Beam Methods Vol. 1*, chapter 14, pages 362–379. Oxford University Press, Oxford, 1988.

[16] C. T. Rettner, H. A. Michelsen, and D. J. Auerbach. Quantum-state-specific dynamics of the dissociative adsorption and associative desorption of H_2 at a Cu(111) surface. *The Journal of chemical physics*, 102(11):4625–4641, 1995.

[17] D. A. King. Thermal desorption from metal surfaces: A review. *Surface Science*, 47(1):384–402, 1975.

[18] G. J. Kroes and C. Díaz. Quantum and classical dynamics of reactive scattering of H_2 from metal surfaces. *Chemical Society Reviews*, 45(13):3658–3700, 2016.

[19] A. W. Kleyn. Molecular beams and chemical dynamics at surfaces. *Chemical Society Reviews*, 32(2):87–95, 2003.

[20] B. Poelsema, K. Lenz, and G. Comsa. The dissociative adsorption of hydrogen on defect-'free' Pt(111). *Journal of physics: condensed matter*, 22(30):304006, 2010.

[21] P. Samson, A. Nesbitt, B. E. Koel, and A. Hodgson. Deuterium dissociation on ordered Sn/Pt(111) surface alloys. *The Journal of chemical physics*, 109(8):3255–3264, 1998.

[22] A. C. Luntz, J. K. Brown, and M. D. Williams. Molecular beam studies of H_2 and D_2 dissociative chemisorption on Pt(111). *The Journal of Chemical Physics*, 93(7):5240–5246, 1990.

[23] J. P. Cowin, C. F. Yu, and L. Wharton. HD scattering from Pt(111): Rotationally mediated selective adsorption. *Surface Science*, 161(1):221–233, 1985.

[24] J. P. Cowin, C. F. Yu, S. J. Sibener, and L. Wharton. HD scattering from Pt(111): Rotational excitation probabilities. *The Journal of chemical physics*, 79(7):3537–3549, 1983.

[25] J. P. Cowin, C. F. Yu, S. J. Sibener, and J. E. Hurst. Bound level resonances in rotationally inelastic HD/Pt(111) surface scattering. *The Journal of Chemical Physics*, 75(2):1033–1034, 1981.

[26] A. T. Gee, B. E. Hayden, C. Mormiche, and T. S. Nunney. The role of steps in the dynamics of hydrogen dissociation on Pt(533). *The Journal of Chemical Physics*, 112(17):7660–7668, 2000.

[27] A. T. Gee, B. E. Hayden, C. Mormiche, and T. S. Nunney. The blocking of the step-mediated indirect channel to hydrogen dissociation by oxygen on Pt(533). *Surface science*, 512(3):165–172, 2002.

[28] I. M. N. Groot, A. W. Kleyn, and L. B. F. Juurlink. The energy dependence of the ratio of step and terrace reactivity for H_2 dissociation on stepped platinum. *Angewandte Chemie International Edition*, 50(22):5174–5177, 2011.

[29] I. M. N. Groot, A. W. Kleyn, and L. B. F. Juurlink. Separating catalytic activity at edges and terraces on platinum: Hydrogen dissociation. *The Journal of Physical Chemistry C*, 117(18):9266–9274, 2013.

[30] I. M. N. Groot, K. J. P. Schouten, A. W. Kleyn, and L. B. F. Juurlink. Dynamics of hydrogen dissociation on stepped platinum. *The Journal of chemical physics*, 129(22):224707, 2008.

[31] D. A. McCormack, R. A. Olsen, and E. J. Baerends. Mechanisms of H_2 dissociative adsorption on the Pt(211) stepped surface. *The Journal of chemical physics*, 122(19):194708, 2005.

[32] R. A. Olsen, D. A. McCormack, M. Luppi, and E. J. Baerends. Six-dimensional quantum dynamics of H_2 dissociative adsorption on the Pt(211) stepped surface. *The Journal of chemical physics*, 128(19):194715, 2008.

[33] G. J. Kroes, C. Díaz, E. Pijper, R. A. Olsen, and D. J. Auerbach. Apparent failure of the born–oppenheimer static surface model for vibrational excitation of molecular hydrogen on copper. *Proceedings of the National Academy of Sciences*, 107(49):20881–20886, 2010.

[34] C. Díaz, E. Pijper, R. A. Olsen, H. F. Busnengo, D. J. Auerbach, and G. J. Kroes. Chemically accurate simulation of a prototypical surface reaction: H_2 dissociation on Cu(111). *Science*, 326(5954):832–834, 2009.

[35] P. Nieto, E. Pijper, D. Barredo, G. Laurent, R. A. Olsen, E. J. Baerends, G. J. Kroes, and D. Farías. Reactive and nonreactive scattering of H_2 from a metal surface is electronically adiabatic. *Science*, 312(5770):86–89, 2006.

[36] E. Pijper, G. J. Kroes, R. A. Olsen, and E. J. Baerends. Reactive and diffractive scattering of H_2 from Pt(111) studied using a six-dimensional wave packet method. *The Journal of chemical physics*, 117(12):5885–5898, 2002.

[37] E. Pijper, G. J. Kroes, R. A. Olsen, and E. J. Baerends. Dissociative and diffractive scattering of H_2 from Pt(111): A four-dimensional quantum dynamics study. *The Journal of chemical physics*, 116(21):9435–9448, 2002.

[38] E. Pijper, M. F. Somers, G. J. Kroes, R. A. Olsen, E. J. Baerends, H. F. Busnengo, A. Salin, and D. Lemoine. Six-dimensional quantum dynamics of scattering of $(v = 0, j = 0)$ H_2 from Pt(1 1 1): comparison to experiment and to classical dynamics results. *Chemical physics letters*, 347(4-6):277–284, 2001.

[39] E. N. Ghassemi, M. Wijzenbroek, M. F. Somers, and G. J. Kroes. Chemically accurate simulation of dissociative chemisorption of D_2 on Pt(111). *Chemical Physics Letters*, 683:329–335, 2017.

[40] G. R. Darling and S. Holloway. Surface temperature effects in the dissociative adsorption of D_2/Cu(111) revisited. *Surface science*, 321(3):L189–L194, 1994.

[41] G. R. Darling and S. Holloway. The dissociation of diatomic molecules at surfaces. *Reports on Progress in Physics*, 58(12):1595, 1995.

[42] G. J. Kroes. Towards chemically accurate simulation of molecule–surface reactions. *Physical Chemistry Chemical Physics*, 14(43):14966–14981, 2012.

[43] B. Riedmüller, F. Giskes, D. G. van Loon, P. Lassing, and A. W. Kleyn. A compact molecular beam line. *Measurement Science and Technology*, 13(2):141, 2001.

[44] H. G. Jenniskens, A. Bot, P. W. F. Dorlandt, W. van Essenberg, E. de Haas, and A. W. Kleyn. An ultrahigh vacuum (UHV) apparatus to study the interaction between adsorbates and photons. *Measurement Science and Technology*, 8(11):1313, 1997.

[45] I. M. N. Groot, H. Ueta, M. J. T. C. van der Niet, A. W. Kleyn, and L. B. F. Juurlink. Supersonic molecular beam studies of dissociative adsorption of H_2 on Ru(0001). *The Journal of chemical physics*, 127(24):244701, 2007.

[46] K. C. Waugh. Methanol synthesis. *Catalysis Today*, 15(1):51–75, 1992.

[47] L. C. Grabow and M. Mavrikakis. Mechanism of methanol synthesis on Cu through CO_2 and CO hydrogenation. *ACS Catalysis*, 1(4):365–384, 2011.

[48] M. Behrens, F. Studt, I. Kasatkin, S. Kühl, M. Hävecker, F. Abild-Pedersen, S. Zander, F. Girgsdies, P. Kurr, B. L. Kniep, et al. The active site of methanol synthesis over $Cu/ZnO/Al_2O_3$ industrial catalysts. *Science*, page 1219831, 2012.

[49] G. Anger, A. Winkler, and K. D. Rendulic. Adsorption and desorption kinetics in the systems H_2/Cu(111), H_2/Cu(110) and H_2/Cu(100). *Surface Science*, 220(1):1–17, 1989.

[50] S. Sakong and A. Groß. Dissociative adsorption of hydrogen on strained Cu surfaces. *Surface science*, 525(1-3):107–118, 2003.

[51] H. F. Berger, M. Leisch, A. Winkler, and K. D. Rendulic. A search for vibrational contributions to the activated adsorption of H_2 on copper. *Chemical physics letters*, 175(5):425–428, 1990.

[52] D. J. Auerbach, C. T. Rettner, and H. A. Michelsen. Interaction dynamics of hydrogen at a Cu(111) surface. *Surface science*, 283(1-3):1–8, 1993.

[53] C. T. Rettner, D. J. Auerbach, and H. A. Michelsen. Role of vibrational and translational energy in the activated dissociative adsorption of D_2 on Cu(111). *Physical review letters*, 68(8):1164, 1992.

[54] C. T. Rettner, H. A. Michelsen, and D. J. Auerbach. From quantum-state-specific dynamics to reaction rates: the dominant role of translational energy in promoting the dissociation of D_2 on Cu(111) under equilibrium conditions. *Faraday Discussions*, 96:17–31, 1993.

[55] C. T. Rettner, H. A. Michelsen, and D. J. Auerbach. Quantum-state-specific dynamics of the dissociative adsorption and associative desorption of H_2 at a Cu(111) surface. *The Journal of chemical physics*, 102(11):4625–4641, 1995.

[56] C. T. Rettner and D. J. Auerbach. Dynamics of the formation of HD from D (H) atoms colliding with H (D) Cu(111): a model study of an eley-rideal reaction. *Surface science*, 357:602–608, 1996.

[57] C. T. Rettner and D. J. Auerbach. Quantum-state distributions for the hd product of the direct reaction of H (D)/Cu (111) with D (H) incident from the gas phase. *The Journal of chemical physics*, 104(7):2732–2739, 1996.

[58] H. A. Michelsen, C. T. Rettner, and D. J. Auerbach. State-specific dynamics of D_2 desorption from Cu(111): the role of molecular rotational motion in activated adsorption-desorption dynamics. *Physical review letters*, 69(18):2678, 1992.

[59] H. A. Michelsen, C. T. Rettner, D. J. Auerbach, and R. N. Zare. Effect of rotation on the translational and vibrational energy dependence of the dissociative adsorption of D_2 on Cu(111). *The Journal of chemical physics*, 98(10):8294–8307, 1993.

[60] G. R. Darling and S. Holloway. Vibrational effects in the associative desorption of H_2. *Surface science*, 268(1-3):L305–L310, 1992.

[61] G. R. Darling and S. Holloway. Enhanced diffraction of vibrationally excited molecules from surfaces. *Chemical physics letters*, 191(5):396–400, 1992.

[62] G. R. Darling and S. Holloway. Rotational effects in the dissociative adsorption of H_2 on Cu(111). *Faraday Discussions*, 96:43–54, 1993.

[63] G. R. Darling and S. Holloway. Dissociation thresholds and the vibrational excitation process in the scattering of H_2. *Surface science*, 307:153–158, 1994.

[64] C. Díaz, R. A. Olsen, D. J. Auerbach, and G. J. Kroes. Six-dimensional dynamics study of reactive and non reactive scattering of H_2 from Cu(111) using a chemically accurate potential energy surface. *Physical Chemistry Chemical Physics*, 12(24):6499–6519, 2010.

[65] M. Balooch, M. J. Cardillo, D. R. Miller, and R. E. Stickney. Molecular beam study of the apparent activation barrier associated with adsorption and desorption of hydrogen on copper. *Surface Science*, 46(2):358–392, 1974.

[66] T. H. Liao and Q. Sun. Chemisorption of hydrogen on stepped surfaces of Ni and Cu. *physica status solidi (b)*, 200(2):491–498, 1997.

[67] Ž. Šljivančanin and B. Hammer. H_2 dissociation at defected Cu: Preference for reaction at vacancy and kink sites. *Physical Review B*, 65(8):085414, 2002.

[68] B. Hammer and J. K. Nørskov. Why gold is the noblest of all the metals. *Nature*, 376(6537):238, 1995.

[69] B. Hammer and J. K. Nørskov. Electronic factors determining the reactivity of metal surfaces. *Surface Science*, 343(3):211–220, 1995.

[70] G. Füchsel, K. Cao, S. Er, E. W. F. Smeets, A. W. Kleyn, L. B. F. Juurlink, and G. J. Kroes. Anomalous dependence of the reactivity on the presence of steps: Dissociation of D_2 on Cu(211). *The journal of physical chemistry letters*, 2017.

[71] F. Nattino, C. Díaz, B. Jackson, and G. J. Kroes. Effect of surface motion on the rotational quadrupole alignment parameter of D_2 reacting on Cu(111). *Physical review letters*, 108(23):236104, 2012.

[72] M. A. van Hove and G. A. Somorjai. A new microfacet notation for high-miller-index surfaces of cubic materials with terrace, step and kink structures. *Surface Science*, 92(2-3):489–518, 1980.

[73] G. Kresse and J. Hafner. Ab initio molecular dynamics for liquid metals. *Physical Review B*, 47(1):558, 1993.

[74] G. Kresse and J. Hafner. Ab initio molecular-dynamics simulation of the liquid-metal–amorphous-semiconductor transition in germanium. *Physical Review B*, 49(20):14251, 1994.

[75] G. Kresse and J. Furthmüller. Efficiency of ab-initio total energy calculations for metals and semiconductors using a plane-wave basis set. *Computational materials science*, 6(1):15–50, 1996.

[76] G. Kresse and J. Furthmüller. Efficient iterative schemes for ab initio total-energy calculations using a plane-wave basis set. *Physical review B*, 54(16):11169, 1996.

[77] M. Wijzenbroek, D. M. Klein, B. Smits, M. F. Somers, and G. J. Kroes. Performance of a non-local Van der Waals density functional on the dissociation of H_2 on metal surfaces. *The Journal of Physical Chemistry A*, 119(50):12146–12158, 2015.

[78] C. T. Rettner and D. J. Auerbach. Dynamics of the eley-rideal reaction of D atoms with H atoms adsorbed on Cu(111): Vibrational and rotational state distributions of the HD product. *Physical review letters*, 74(22):4551, 1995.

[79] C. T. Rettner, H. A. Michelsen, and D. J. Auerbach. Determination of quantum-state-specific gas—surface energy transfer and adsorption probabilities as a function of kinetic energy. *Chemical physics*, 175(1):157–169, 1993.

[80] H. Ueta, L. Chen, R. D. Beck, I. Colón-Dìaz, and B. Jackson. Quantum state-resolved CH_4 dissociation on Pt(111):

coverage dependent barrier heights from experiment and density functional theory. *Physical Chemistry Chemical Physics*, 15(47):20526–20535, 2013.

[81] K. H. Rieder and W. Stocker. Hydrogen-induced subsurface reconstruction of Cu(110). *Physical review letters*, 57(20):2548, 1986.

[82] U. Bischler, P. Sandl, E. Bertel, T. Brunner, and W. Brenig. Sticking, adsorption, and absorption of atomic H on Cu(110). *Physical review letters*, 70(23):3603, 1993.

[83] K. Doblhoff-Dier, J. Meyer, P. .E Hoggan, and G. J. Kroes. Quantum monte carlo calculations on a benchmark molecule-metal surface reaction: H_2+ Cu(111). *Journal of chemical theory and computation*, 13(7):3208–3219, 2017.

[84] Y. M. Sun, W. Dong, and X. H. Yan. Coverage effect on reactivity can be more complicated than what you believe: H2 dissociation on h-precovered pd (111). *The Journal of chemical physics*, 140(24):244703, 2014.

[85] D. A. Butler, B. E. Hayden, and J. D. Jones. Precursor dynamics in dissociative hydrogen adsorption on w (100). *Chemical physics letters*, 217(4):423–429, 1994.

[86] E. Habenschaden and J. Küppers. Evaluation of flash desorption spectra. *Surface science letters*, 138(1):L147–L150, 1984.

[87] J. K. Nørskov, T. Bligaard, A. Logadottir, S. Bahn, L. B. Hansen, M. Bollinger, H. Bengaard, B. Hammer, Z. Sljivancanin, M. Mavrikakis, et al. Universality in heterogeneous catalysis. *Journal of Catalysis*, 209(2):275–278, 2002.

[88] C. Hahn, J. Shan, Y. Liu, O. Berg, A. W. Kleijn, and L. B. F. Juurlink. Employing a cylindrical single crystal in gas-surface dynamics. *The Journal of chemical physics*, 136(11):114201, 2012.

[89] S. Gudmundsdóttir, E. Skúlason, K. J. Weststrate, L. Juurlink, and H. Jónsson. Hydrogen adsorption and desorption at the Pt(110)-(1× 2) surface: experimental and theoretical study. *Physical Chemistry Chemical Physics*, 15(17):6323–6332, 2013.

[90] S. Kaufmann, Q. Shuai, D. J. Auerbach, D. Schwarzer, and A. M. Wodtke. Associative desorption of hydrogen isotopologues from copper surfaces: Characterization of two reaction mechanisms. *The Journal of Chemical Physics*, 148(19):194703, 2018.

[91] G. A. Somorjai and Y. Li. *Introduction to surface chemistry and catalysis*. John Wiley & Sons, 2010.

[92] K. E. Lu and R. R. Rye. Flash desorption and equilibration of H_2 and D_2 on single crystal surfaces of platinum. *Surface Science*, 45(2):677–695, 1974.

[93] S. L. Bernasek, W. J. Siekhaus, and G. A. Somorjai. Molecular-beam study of hydrogen-deuterium exchange on low-and high-miller-index platinum single-crystal surfaces. *Physical Review Letters*, 30(24):1202, 1973.

[94] S. L. Bernasek and G. A. Somorjai. Molecular beam study of the mechanism of catalyzed hydrogen–deuterium exchange on platinum single crystal surfaces. *The Journal of Chemical Physics*, 62(8):3149–3161, 1975.

[95] S. L. Bernasek and G. A. Somorjai. Small molecule reactions on stepped single crystal platinum surfaces. *Surface Science*, 48(1):204–213, 1975.

[96] R. J. Gale, M. Salmeron, and G. A. Somorjai. Variation of surface reaction probability with reactant angle of incidence: A molecular beam study of the asymmetry of stepped platinum crystal surfaces for hh bond breaking. *Physical Review Letters*, 38(18):1027, 1977.

[97] M. Salmeron, R. J. Gale, and G. A. Somorjai. Molecular beam study of the H_2-D_2 exchange reaction on stepped platinum crystal surfaces: Dependence on reactant angle of incidence. *The Journal of Chemical Physics*, 67(11):5324–5334, 1977.

[98] M. Salmerón, R. J. Gale, and G. A. Somorjai. A modulated molecular beam study of the mechanism of the $H_2 - D_2$ exchange reaction on Pt(111) and Pt(332) crystal surfaces. *The Journal of Chemical Physics*, 70(6):2807–2818, 1979.

[99] K. Christmann and G. Ertl. Interaction of hydrogen with Pt(111): the role of atomic steps. *Surface Science*, 60(2):365–384, 1976.

[100] B. Poelsema, K. Lenz, and G. Comsa. The dissociative adsorption of hydrogen on Pt(111): Actuation and acceleration by atomic defects. *The Journal of chemical physics*, 134(7):074703, 2011.

[101] R. van Lent, S. V. Auras, K. Cao, A. J. Walsh, M. A. Gleeson, and L. B. F. Juurlink. Resolving an old problem: how does H_2 dissociate on pt? *submitted*.

[102] C. M. Greenlief, S. Akhter, and J. M. White. Temperature-programmed desorption study of hydrogen-deuterium exchange on platinum (111) and the role of subsurface sites. *The Journal of Physical Chemistry*, 90(17):4080–4083, 1986.

[103] L. K. Verheij, M. B. Hugenschmidt, A. B. Anton, B. Poelsema, and G. Comsa. A molecular beam study of the interaction between hydrogen and the Pt(111) surface. *Surface Science*, 210(1-2):1–26, 1989.

[104] A. L. Walter, F. Schiller, M. Corso, L. R. Merte, F. Bertram, J. Lobo-Checa, M. Shipilin, J. Gustafson, E. Lundgren, A. X. Bríon-Ríos, et al. X-ray photoemission analysis of clean and carbon monoxide-chemisorbed platinum (111) stepped surfaces using a curved crystal. *Nature communications*, 6:8903, 2015.

[105] M. Ilyn, A. Magaña, A. L. Walter, J. Lobo-Checa, D. G. de Oteyza, F. Schiller, and J. E. Ortega. Step-doubling at vicinal Ni(111) surfaces investigated with a curved crystal. *The Journal of Physical Chemistry C*, 121(7):3880–3886, 2017.

[106] G. Comsa, G. Mechtersheimer, and B. Poelsema. He beam scattering and LEED evidence for partial facetting of a Pt(997) surface. *Surface Science*, 97(1):L297–L303, 1980.

[107] G. Comsa, G. Mechtersheimer, and B. Poelsema. He-beam scattering study of the dynamics of oxygen induced reconstruction of the Pt(997) surface: I. dynamics of double step formation and destruction. *Surface Science*, 119(2-3):159–171, 1982.

[108] E. Hahn, H. Schief, V. Marsico, A. Fricke, and K. Kern. Orientational instability of vicinal Pt surfaces close to (111). *Physical review letters*, 72(21):3378, 1994.

[109] L. Jacobse, A. den Dunnen, and L. B. F. Juurlink. The molecular dynamics of adsorption and dissociation of O_2 on Pt(553). *The Journal of chemical physics*, 143(1):014703, 2015.

[110] M. A. van Hove and G. A. Somorjai. A new microfacet notation for high-miller-index surfaces of cubic materials with terrace, step and kink structures. *Surface Science*, 92(2-3):489–518, 1980.

[111] E. D. Williams, R. J. Phaneuf, J. Wei, N. C. Bartelt, and T. L. Einstein. Thermodynamics and statistical mechanics of the faceting of stepped Si(111). *Surface science*, 294(3):219–242, 1993.

[112] B. Lang, R. W. Joyner, and G. A. Somorjai. Low energy electron diffraction studies of chemisorbed gases on stepped surfaces of platinum. *Surface science*, 30(2):454–474, 1972.

[113] H. A. Michelsen and D. J. Auerbach. A critical examination of data on the dissociative adsorption and associative desorption of hydrogen at copper surfaces. *The Journal of chemical physics*, 94(11):7502–7520, 1991.

[114] T. Zambelli, J. V. Barth, J. Wintterlin, and G. Ertl. Complex pathways in dissociative adsorption of oxygen on platinum. *Nature*, 390(6659):495, 1997.

[115] M. M. Montemore, M. A. van Spronsen, Robert J. Madix, and C. M. Friend. O_2 activation by metal surfaces: Implications for bonding and reactivity on heterogeneous catalysts. *Chemical reviews*, 2017.

[116] A. C. Luntz, J. Grimblot, and D. E. Fowler. Sequential precursors in dissociative chemisorption: O_2 on Pt(111). *Physical Review B*, 39(17):12903, 1989.

[117] J. Grimblot, A. C. Luntz, and D. E. Fowler. Low temperature adsorption of O_2 on Pt(111). *Journal of electron spectroscopy and related phenomena*, 52:161–174, 1990.

[118] W. Wurth, J. Stöhr, P. Feulner, X. Pan, K. R. Bauchspiess, Y. Baba, E. Hudel, G. Rocker, and D. Menzel. Bonding, structure, and magnetism of physisorbed and chemisorbed O_2 on Pt(111). *Physical review letters*, 65(19):2426, 1990.

[119] K. Gustafsson and S. Andersson. Infrared spectroscopy of physisorbed and chemisorbed O_2 on Pt(111). *The Journal of chemical physics*, 120(16):7750–7754, 2004.

[120] J. L. Gland, B. A. Sexton, and G. B. Fisher. Oxygen interactions with the Pt(111) surface. *Surface Science*, 95(2-3):587–602, 1980.

[121] H. Steininger, S. Lehwald, and H. Ibach. Adsorption of oxygen on Pt(111). *Surface Science*, 123(1):1–17, 1982.

[122] N. R. Avery. An EELS and TDS study of molecular oxygen desorption and decomposition on Pt(111). *Chemical Physics Letters*, 96(3):371–373, 1983.

[123] M. D. Williams, D. S. Bethune, and A. C. Luntz. Coexistence of precursor and direct dynamics: The sticking of O_2 on a Pt(111) surface. *The Journal of Chemical Physics*, 88(4):2843–2845, 1988.

[124] A. C. Luntz, M. D. Williams, and D. S. Bethune. The sticking of O_2 on a Pt(111) surface. *The Journal of chemical physics*, 89(7):4381–4395, 1988.

[125] C. T. Rettner, H. A. Michelsen, D. J. Auerbach, and C. B. Mullins. Dynamics of recombinative desorption: Angular distributions of H_2, HD, and D_2 desorbing from Cu(111). *The Journal of chemical physics*, 94(11):7499–7501, 1991.

[126] P. D. Nolan, B. R. Lutz, P. L. Tanaka, J. E. Davis, and C. B. Mullins. Molecularly chemisorbed intermediates to oxygen adsorption on Pt(111): A molecular beam and electron energy-loss spectroscopy study. *The Journal of chemical physics*, 111(8):3696–3704, 1999.

[127] A. V. Walker, B. Klötzer, and D. A. King. Dynamics and kinetics of oxygen dissociative adsorption on Pt {110}(1× 2). *The Journal of chemical physics*, 109(16):6879–6888, 1998.

[128] A. T. Gee and B. E. Hayden. The dynamics of O_2 adsorption on Pt(533): step mediated molecular chemisorption and dissociation. *The Journal of Chemical Physics*, 113(22):10333–10343, 2000.

[129] P. Gambardella, Ž. Šljivančanin, B. Hammer, M. Blanc, K. Kuhnke, and K. Kern. Oxygen dissociation at Pt steps. *Physical Review Letters*, 87(5):056103, 2001.

[130] C. Badan, R. G. Farber, Y. Heyrich, M. T. M. Koper, D. R. Killelea, and L. B. F. Juurlink. Step-type selective oxidation of platinum surfaces. *The Journal of Physical Chemistry C*, 120(40):22927–22935, 2016.

[131] A. Eichler and J. Hafner. Molecular precursors in the dissociative adsorption of O_2 on Pt(111). *Physical review letters*, 79(22):4481, 1997.

[132] J. S. McEwen, J. M. Bray, C. Wu, and W. F. Schneider. How low can you go? minimum energy pathways for O_2 dissociation on Pt(111). *Physical Chemistry Chemical Physics*, 14(48):16677–16685, 2012.

[133] A. Groß, A. Eichler, J. Hafner, M. J. Mehl, and D. A. Papaconstantopoulos. Unified picture of the molecular adsorption process: O_2/Pt(111). *Surface science*, 539(1-3):L542–L548, 2003.

[134] P. Valentini, T. E. Schwartzentruber, and I. Cozmuta. Molecular dynamics simulation of O_2 sticking on Pt(111) using the ab initio based reaxff reactive force field. *The Journal of chemical physics*, 133(8):084703, 2010.

[135] S. Blomberg, J. Zetterberg, J. Zhou, L. R. Merte, J. Gustafson, M. Shipilin, A. Trinchero, L. A. Miccio, A. Magaña, M. Ilyn, et al. Strain dependent light-off temperature in catalysis revealed by planar laser-induced fluorescence. *ACS Catalysis*, 7(1):110–114, 2016.

[136] M. Kurahashi and Y. Yamauchi. Production of a single spin-rotational state $[(J, M) = (2, 2)]$ selected molecular oxygen $(^3\Sigma_g^-)$ beam by a hexapole magnet. *Review of Scientific Instruments*, 80(8):083103, 2009.

[137] M. Kurahashi. Oxygen adsorption on surfaces studied by a spin- and alignment-controlled O_2 beam. *Progress in Surface Science*, 91(1):29–55, 2016.

[138] H. Ueta and M. Kurahashi. Dynamics of O_2 chemisorption on a flat platinum surface probed by an alignment-controlled O_2 beam. *Angewandte Chemie International Edition*, 56(15):4174–4177, 2017.

[139] H. Ueta and M. Kurahashi. Steric effect in CO oxidation on Pt(111). *The Journal of Chemical Physics*, 147(19):194705, 2017.

[140] A. J. Walsh, R. van Lent, S. V Auras, M. A. Gleeson, O. T. Berg, and L. B. F. Juurlink. Step-type and step-density influences on CO adsorption probed by reflection absorption infrared spectroscopy using a curved Pt(111) surface. *Journal of Vacuum Science & Technology A: Vacuum, Surfaces, and Films*, 35(3):03E102, 2017.

[141] M. Kurahashi and Y. Yamauchi. Huge steric effects in surface oxidation of Si(100). *Physical Review B*, 85(16):161302, 2012.

[142] L. A. Miccio, M. Setvin, M. Müller, M. Abadía, I. Piquero, J. Lobo-Checa, F. Schiller, C. Rogero, M. Schmid, D. Sánchez-Portal, et al. Interplay between steps and oxygen vacancies on curved TiO_2(110). *Nano letters*, 16(3):2017–2022, 2016.

B

Samenvatting

Heterogene katalyse wordt al sinds mensenheugenis toegepast zonder dat men besef had van de onderliggende processen. Om de onderliggende mechanismen van deze chemische reacties te ontrafelen worden over het algemeen eenvoudige 'model systemen' gebruikt. Chemische reacties in deze model systemen verlopen met dezelfde elementaire reactie stappen als onder realistische condities. Ondanks dat deze systemen extensief zijn bestudeerd, is veel vooralsnog onduidelijk. In dit proefschrift concentreren we op simpele systemen, zoals waterstof en zuurstof dissociatie aan platina, en waterstof dissociatie aan koper oppervlakken.

Waterstof dissociatie aan Pt oppervlakken is een model systeem voor zwak (niet) geactiveerde moleculaire dissociatie. Dit systeem is uitvoerig bestudeerd met behulp van experimentele technieken en theoretische berekeningen. De potentieel energie oppervlakken voor dit systeem vertoont zowel energetische als geometrische corrugatie. Met behulp van een verstelbare Specifieke Reactie Parameter (SRP), gekalibreerd door Ghassemi et al. met experimentele data voor D_2 dissociatie aan Pt(111) van Luntz et al., wordt goede overeenkomst tussen theorie en experiment verkregen [22, 39]. De resultaten voorspellen een klein verschil in plak kans voor twee verschillende azimuthale hoeken. In hoofdstuk 3 hebben we waterstof dissociatie aan Pt(111) bestudeerd. Onze resultaten komen overeen met eerder experimenteel werk. De plak kans is zwak afhankelijk van de azimuthale oriëntatie van de invalshoek, in overeenstemming met de SRP-DFT berekeningen.

Waterstof dissociatie aan Cu oppervlakken is een model systeem voor sterk geactiveerde dissociatie aan metaal oppervlakken. Daarnaast is dit systeem ook belangrijk als de eerste stap in de hydrogenering van CO_2 naar methanol aan een $Cu/ZnO/Al_2O_3$ katalysator. Begrip van de elementaire reactie stappen kan de ontwikkeling van nieuwe katalysatoren sturen. Om randen aan katalysatoren na te boot-

sen, worden vaak macroscopisch vlakke oppervlakken gebruikt waarbij systematisch atomaire stappen worden geïntroduceerd. De lagere coördinatie van atomen aan de staprand resulteert meestal in een lagere dissociatie barrière ten gevolge van een hogere bindingsenergie. In hoofdstuk 4 bestudeerden we waterstof adsorptie en desorptie aan de Cu(111) en Cu(211) oppervlakken. Hier vinden wij dat het Cu(111) oppervlak reactiever is dan het Cu(211) oppervlak. A-type stapranden veroorzaken een, voor zover wij weten, unieke verhoging en verlaging van de activatie en desorptie barrière distributies. Daarnaast hebben wij aangetoond dat de barrière distributies, welke zwak afhankelijk zijn van de waterstof bedekkingsgraden voor adsorptie en bij verzadiging, óók afhankelijk zijn van de invalsenergie. Laterale interacties tussen geadsorbeerde waterstof atomen moeten daarom zwak zijn, vooral bij een lage bedekkingsgraad.

In hoofdstukken 5 en 6 gebruikten we een gekromd Pt(111) éénkristal. De top van dit kristal is Pt(111). Het kristal bevat A-type stapranden aan de ene en B-type stapranden aan de andere zijde, welke beide één atoom hoog zijn. De stapdichtheid varieert lineair met de afstand tot de top van het kristal. Hiermee kan een serie aan gestapte oppervlakken met A-type en B-type stapranden worden nagebootst. Hiermee kan de materiaal kloof tussen éénkristallijne oppervlakken en echte katalysatoren in zekere mate worden overbrugd.

In hoofdstuk 5 bestuurden we de vorming van HD aan een gekromd Pt(111) oppervlak. Bij lage invalsenergie is de vorming van HD afhankelijk van de stapdichtheid. Met de juiste schoonmaak procedure en uitgloeien bij 850 K is de HD vorming lineair met de afstand tot de top van het kristal. Dit toont aan dat de stapdichtheid lineair verloopt met de verplaatsing. Dit wordt bevestigd met LEED waar de karakteristieke gespleten pieken worden waargenomen in het diffractie patroon. De vorming van HD verlaagt aan beide zijden van het éénkristal wanneer dezelfde schoonmaak procedure wordt gebruikt, maar opgevolgd wordt door uitgloeien bij 1200 K. HD vorming bij A-type stapranden is lager over het gehele bereik en in het bijzonder rondom Pt(655). Bij B-type stapranden is de verlaging van de HD vorming gelokaliseerd rondom Pt(443). Deze verlagingen geven aan dat facetten vormen, ondanks dat dit niet zichtbaar is in LEED. HD vorming als chemische methode is in dit geval gevoeliger dan LEED. De reconstructie vereist meer onderzoek met behulp van de raster tunnel microscoop (STM). Onze data toont daarnaast aan dat facetten vormen bij Pt(443), en niet

bij Pt(997). In het verleden is aangetoond dat het Pt(997) oppervlak reconstrueert met behulp van He diffractie, LEED, en STM.

Zuurstof dissociatie aan Pt is ingewikkelder dan waterstof dissociatie. Het proces omvat een moleculaire physisorptie toestand, twee moleculaire chemisorptie toestanden, en een atomaire chemisorptie toestand. Eerder onderzoek toonde aan dat zuurstof dissociatie gedomineerd wordt door stap randen middels een indirect dissociatie mechanisme. Dit mechanisme verloopt vermoedelijk via een moleculaire physisorptie toestand en leidt tot hogere reactiviteit dan de (111) terrassen. In hoofdstuk 6 bestudeerden we O_2 dissociatie aan Pt oppervlakken met hetzelfde gekromde Pt(111) éénkristal. De plak kans van O_2 gaat lineair omhoog met de afstand tot de top van het kristal voor zowel A-type als B-type stapranden bij lage kinetische energie, 65 meV. We zien een sterke hellingshoek en nagenoeg identieke absolute waarden aan beide zijden. Dit toont aan dat de dynamische processen die ten grondslag liggen voor het plakken van O_2, gedomineerd wordt door stapranden maar ongevoelig is voor de lokale structuur van de staprand. Bij hogere invalsenergieën verdwijnt het lineaire karakter van deze afhankelijkheid. Dit toont aan dat de dynamische processen niet alleen door stapranden worden bepaald. Door middel van een oriëntatie gecontroleerde O_2 bundel blijkt dat zuurstof bij voorkeur plakt aan Pt(111) wanneer de moleculaire-as van het molecuul parallel is aan het oppervlak. Bij het Pt(553) oppervlak zien we geen voorkeur voor een bepaalde oriëntatie van de moleculaire-as. Bij hogere kinetische energie convergeert de verhouding $S_0(H)/S_0(C_z)$ voor Pt(111) en Pt(553) naar dezelfde waarde. De resultaten voor R en L experimenten tonen aan dat dissociatie aan A-type en B-type stapranden duidelijk voorkeur hebben voor moleculen met de moleculaire-as parallel aan de (100) en (110) stapranden.

List of publications

This thesis is based on the following publications

Chapter 3

A molecular beam study of D_2 dissociation on Pt(111): testing SRP-DFT calculations
Chemical Physics Letters, 2018, 706, pp 680-683
Kun Cao, Richard van Lent, Aart W. Kleyn, and Ludo B. F. Juurlink

Chapter 4

Anomalous dependence of the reactivity on the presence of steps: dissociation of D_2 on Cu(211)
The Journal of Physical Chemistry Letters, 2018, 9(1), pp 170–175
Gernot Füchsel, Kun Cao, Süleyman Er, Egidius W. F. Smeets, Aart W. Kleyn, Ludo B. F. Juurlink, and Geert-Jan Kroes
The first two authors contributed equally to this paper

Hydrogen adsorption and desorption from Cu(111) and Cu(211)
Physical Chemistry Chemical Physics, 2018, Accepted Manuscript
Kun Cao, Gernot Füchsel, Aart W. Kleyn, and Ludo B.F. Juurlink
This article is part of the themed collection: "2018 PCCP HOT Articles"

Chapter 5

Structure dependence of HD formation on curved Pt(111) surface
In preparation
Kun Cao, Aart W. Kleyn, and Ludo B. F. Juurlink

Chapter 6

The two faces of step defects in O_2 reaction on Pt
Nature Chemistry, in preparation
Kun Cao, Mitsunori Kurahashi and Ludo B. F. Juurlink

Other publications

Resolving an old problem: how does H_2 dissociate on Pt?
Science, submitted
Richard van Lent, Sabine V. Auras, Kun Cao, Anton J. Walsh, Michael A. Gleeson and Ludo B. F. Juurlink

Curriculum Vitae

Kun Cao was born in Zhumadian, a city in Henan province in China in 1986. He obtained his bachelor degree in Tsinghua University in 2008. He obtained his master degree in China Academy of Engineering Physics in 2011. From 2011 to 2014, he worked at China Academy of Engineering Physics as an assistant research fellow. In September 2014, Kun started his PhD research at Leiden University (the Netherlands) in the group "Catalysis and Surface Chemistry" (CASC). The research was carried out under the supervision of Prof. Dr. Marc T. M. Koper, Prof. Dr. Aart W. Kleyn and Dr. Ludo B. F. Juurlink and sponsored by the China Scholorship Council (CSC). The topic of his work was structure dependence of molecular reactions on surfaces. The results are presented in this thesis. Parts of the results have been presented at the following conferences:

- Chemistry As Innovating Science (CHAINS) in Veldhoven, the Netherlands in 2014 (poster)
- International Conference on Molecular Energy Transfer in Complex Systems (ICOMET) in Chengdu, China in 2015 (poster)
- International Conference on Scattering of Atoms and Molecules from Surfaces (SAMS) in Bergen, Norway in 2016 (poster)